Advanced diffusion-weighted MRI for cancer microstructure assessment in body imaging, and its relationship with histology

Ella Fokkinga, MSc[1,2], Juan A. Hernandez-Tamames, PhD[3,4], Andrada Ianus, PhD[5], Markus Nilsson, PhD[6], Chantal M. W. Tax, PhD[7,8], Raquel Perez-Lopez, MD, PhD[2*†], Francesco Grussu, PhD[2*†]

* Joint corresponding author † Joint last (senior) author

[1]Biomedical Engineering, track Medical Physics, Delft University of Technology, Delft, The Netherlands [2]Radiomics Group, Vall d'Hebron Institute of Oncology, Vall d'Hebron Barcelona Hospital Campus, Barcelona, Spain [3]Department of Radiology and Nuclear Medicine, Erasmus MC, Rotterdam, The Netherlands [4]Department of Imaging Physics, Delft University of Technology, Delft, The Netherlands [5]Champalimaud Research, Champalimaud Foundation, Lisbon, Portugal [6]Dept. Diagnostic Radiology, Clinical Sciences Lund, Lund, Sweden [7]Cardiff University Brain Research Imaging Center (CUBRIC), School of Physics and Astronomy, Cardiff University, Cardiff, United Kingdom [8]University Medical Center Utrecht, Utrecht, The Netherlands

This is the accepted version of the following article: "*Advanced diffusion-weighted MRI for cancer microstructure assessment in body imaging, and its relationship with histology*", Fokkinga E et al, Journal of Magnetic Resonance Imaging 2023, DOI: 10.1002/jmri.29144, which has been published in final form at https://doi.org/ 10.1002/jmri.29144.

Corresponding author information:

Raquel Perez-Lopez: Radiomics Group, Vall d'Hebron Institute of Oncology (VHIO), Cellex Center, Carrer de Natzaret 115-117, 08035 Barcelona, Spain. Telephone: +34 932543450 ext. 8682. Email: rperez@vhio.net

Francesco Grussu: Radiomics Group, VHIO, Cellex Center, Carrer de Natzaret 115-117, 08035 Barcelona, Spain. Telephone: +34 932543450 ext. 8682. Email: fgrussu@vhio.net

Grant Support:

FG receives the support of a fellowship from "la Caixa" Foundation (ID 100010434). The fellowship code is LCF/BQ/PR22/11920010. RPL is supported by "la Caixa" Foundation, a CRIS Foundation Talent Award (TALENT19-05), the FERO Foundation, the Instituto de Salud Carlos III-Investigacion en Salud (PI18/01395 and PI21/01019), the Prostate Cancer Foundation (18YOUN19) and the Asociación Española Contra el Cancer (AECC) (PRYCO211023SERR). AI is supported by "la Caixa" Foundation (ID 100010434) and European Union's Horizon 2020 Research and Innovation Program (Marie Skłodowska-Curie grant No. 847648), fellowship code LCF/BQ/PI20/11760029. CMWT was supported by a Veni grant (17331) from the Dutch Research Council (NWO) and a Sir Henry Wellcome Fellowship (215944/Z/19/Z). MN is supported by the Swedish Research Council (2020-04549), the Cancer Foundation (2022/2414), and ALF. This research was funded in whole, or in part, by the Wellcome Trust [Grant number 215944/Z/19/Z]. For the purpose of open access, the author has applied a CC BY public copyright licence to any Author Accepted Manuscript version arising from this submission.

Conflict of interest: MN holds stocks in Random Walk Imaging AB, which has financial interests connected to advanced diffusion encoding protocols.

Running Title: Diffusion MRI and histology in cancer

Abstract

Diffusion-Weighted Magnetic Resonance Imaging (DW-MRI) aims to disentangle multiple biological signal sources in each imaging voxel, enabling the computation of innovative maps of tissue microstructure. DW-MRI model development has been dominated by brain applications. More recently, advanced methods with high fidelity to histology are gaining momentum in other contexts, e.g., in oncological applications of body imaging, where new biomarkers are urgently needed. The objective of this article is to review the state-of-the-art of DW-MRI in body imaging (i.e., not including the nervous system) in oncology, and to analyse its value as compared to reference co-localised histology measurements, given that demonstrating the histological validity of any new DW-MRI method is essential. In this article, we review the current landscape of DW-MRI techniques that extend standard Apparent Diffusion Coefficient (ADC), describing their acquisition protocols, signal models, fitting settings, microstructural parameters, and relationship with histology. Pre-clinical, clinical and *in/ex vivo* studies were included. The most used techniques were Intravoxel Incoherent Motion (IVIM, 36.3% of used techniques), Diffusion Kurtosis Imaging (DKI, 16.7%), Vascular, Extracellular, and Restricted Diffusion for Cytometry in Tumors (VERDICT, 13.3%), and Imaging Microstructural Parameters Using Limited Spectrally-Edited Diffusion (IMPULSED, 11.7%). Another notable category of techniques relates to innovative b-tensor diffusion encoding or joint diffusion-relaxometry. The reviewed approaches provide histologically-meaningful indices of cancer microstructure (e.g., vascularisation/cellularity) which, while not necessarily accurate numerically, may still provide useful sensitivity to microscopic pathological processes. Future work of the community should focus on improving the inter-/intra-scanner robustness, and on assessing histological validity in broader contexts.

Keywords

- Diffusion-Weighted Magnetic Resonance Imaging (DW-MRI)
- Body
- Histology
- Microstructure
- Cancer

List of abbreviations

- ADC: Apparent Diffusion Coefficient
- AI: Artificial Intelligence
- AIC: Akaike Information Criterion
- AMICO: Accelerated Microstructure Imaging via Convex Optimization

- BP: Bayesian-Probability
- CV: Coefficient of Variation
- DCE: Dynamic Contrast Enhanced
- DDE: Double Diffusion Encoding
- DKI: Diffusion Kurtosis Imaging
- DNN: Deep Neural Network
- DR-CSI: Diffusion-Relaxation Correlation Spectrum Imaging
- DSI: Diffusion Spectrum Imaging
- DTD: Diffusion Tensor Distribution
- DW: Diffusion-weighted
- FEXI: Filter-Exchange Imaging
- FWHM: Full-width-at-half-maximum
- GAM: Generalised Additive Model
- GAN: General Adversarial Network
- HM-MRI: Hybrid Multidimensional Magnetic Resonance Imaging
- IMPULSED: Imaging Microstructural Parameters Using Limited Spectrally-Edited Diffusion
- IVIM: Intravoxel Incoherent Motion
- LM: Levenberg-Marquardt
- LTE: Linear Tensor Encoding
- MAP-MRI: Mean Apparent Propagator Magnetic Resonance Imaging
- MC: Monte Carlo
- MDD-MRI: Multi-Dimension Diffusion Magnetic Resonance Imaging
- mpMRI: Multi-parametric Magnetic Resonance Imaging
- MRI: Magnetic Resonance Imaging
- MD: Mean Displacement
- MSD: Mean Squared Displacement

- MVD: Microvessel Density
- OGSE: Oscillating Gradient Spin Echo
- ONCO-RADS: Oncologically Relevant Findings Reporting and Data System
- PCI: Pericyte Coverage Index
- PIRADS: Prostate Imaging Reporting and Data System
- PGSE: Pulsed Gradient Spin Echo
- POMACE: Pulsed and Oscillating Gradient MRI for Assessment of Cell Size and Extracellular Space
- PRISMA-ScR: Preferred Items for Systematic Reviews and Meta-analyses Extension for Scoping Reviews
- PTE: Planar Tensor Encoding
- PZD: Probability of Zero Displacement
- QSI: Q-Space Imaging
- RSI: Restriction Spectrum Imaging
- RTAP: Return-To-Axis Probability
- RTOP: Return-To-Origin Probability
- RTPP: Return-To-Plane Probability
- SEM: Stretched Exponential Model
- SG: Segmented-Constrained
- SNR: Signal-to-Noise Ratio
- STE: Spherical Tensor Encoding
- SU: Segmented-Unconstrained
- TDD: Time-Dependent Diffusion
- TDS: Temporal Diffusion Spectroscopy
- TR: Trust-Region
- VERDICT: Vascular, Extracellular, and Restricted Diffusion for Cytometry in Tumors
- VM: Vasculogenic Mimicry

1 Introduction

Diffusion-weighted (DW) Magnetic Resonance Imaging (MRI) detects signals that encode water diffusion in the body. Its ultimate goal is the estimation of the tissue *microstructure* that determines diffusion patterns, i.e., statistics of biological properties at the $\sim$ 1-100 μm length scale, from sets of MRI signal measurements [1, 2]. Motion-probing gradients are used to encode salient characteristics of water diffusion in tissues into the MRI signal. The classical DW-MRI experiment is based on the Pulsed Gradient Spin Echo (PGSE) sequence, also known as the Stejskal-Tanner experiment [3], Single Diffusion Encoding, or Linear Tensor Encoding (LTE) [4] with PGSE wave forms. The idealised PGSE experiment is illustrated in Fig. 1, in which motion-probing magnetic field gradients are placed on either side of a spin echo refocussing pulse. Several approaches have been proposed to enable microstructure estimation, and the latest methods entail rich acquisitions coupled with sophisticated signal modelling (Appendix A).

A number of recent articles have reviewed the state-of-the-art of DW-MRI applications [5–8]. However, these tend to focus heavily on brain imaging, especially in neurological or psychiatric disorders, and reviews in contexts of body imaging in oncology are limited [9–11], despite the rapidly growing amount of research in this field. Moreover, while DW-MRI is intimately related to histology, recent reviews do not typically assess the techniques taking into account their actual histological validity and histopathological specificity. Histological validation is a key step in the development of any new DW-MRI technique, as it is essential to assess the implication of the modelling assumptions, and to confirm that the method is actually sensitive and specific to the histopathological characterisitcs that it intends to measure [2].

Given the importance of linking DW-MRI measures with the underlying tissue histology, the objective of this paper is to review the state-of-the-art of DW-MRI in the context of oncological body imaging (beyond the central nervous system, i.e., mainly abdominal and pelvic imaging), with an emphasis on their value in the assessment of microstructure as compared to reference histopathology. We specifically aimed to provide an overview of the landscape of advanced DW-MRI methods that extend Apparent Diffusion Coefficient (ADC), focussing on techniques whose indices have been compared to histology in oncological body imaging. In doing so, we took a mainly narrative approach, while also presenting some quantitative information from the articles. This was related to the application area (anatomical, cancer type), scanning settings, and level of correlation histology.

2 Methods

2.1 DW-MRI technique selection

Given the high number of DW-MRI methods used to assess microstructure and the variety of approaches followed to relate DW-MRI and histology, we carried out a literature search in PubMed to guide the selection of the techniques in this review. The search aimed to identify techniques that are relevant to body imaging, and that offer sensitivity to the

underlying tissue histology (search query: Appendix B). The search adhered to the Preferred Items for Systematic Reviews and Meta-analyses Extension for Scoping Reviews (PRISMA-ScR) guidelines [12] and was performed on September the 8th 2023.

Inclusion criteria were: (i) primary study, (ii) English language, (iii) report an application of DW-MRI, (iv) the DW-MRI technique provides a direct estimate of a microstructural property, or offers some markers that extend routine Apparent Diffusion Coefficient (ADC) (so that they rely on a signal model with more tissue parameters than simple ADC), (iv) focussed on pre-clinical, clinical, *in/ex vivo* oncology studies (studies that compared DW-MRI metrics from animal or human cancer cells or tissue, scanned either *in vivo* or *ex vivo*, and then compared to metrics derived from microscopy performed on the same specimens after MRI), (v) focussed on body imaging (that is, on applications that do not include imaging of the nervous system).

2.2 Technique application and MRI-histology correlation assessments

We screened all included articles and recorded the MRI scanner used, the tissue condition during MR imaging, the area of application, as well as correlation coefficients between any DW-MRI and histological metric, whenever reported.

2.3 Narrative description of the selected techniques

For each identified technique, we described i) signal model, ii) required diffusion encoding protocol, iii) fitting methods, iv) main histological correlates, and finally iv) discussed its strengths and weaknesses. Note that with both signal "model" and "representation" we mean a functional form capable of predicting the diffusion MRI signal for a variety of possible diffusion protocols given a set of tissue parameters, which can be estimated through fitting from sets of DW-MRI measurements. In the case of models, these parameters typically refer to histological characteristics, such as cell size or cell density. Tissue parameters in signal representations instead are apparent phenomenological properties that are sensitive to different histological characteristics at once, and typically change when the diffusion encoding gradient timings vary (e.g., apparent diffusion coefficient or kurtosis).

3 Results

3.1 DW-MRI technique selection

354 articles were identified. 87 articles were excluded based on title and abstract. Of the remaining 267 articles, 238/267 focused on the use of techniques that compute indirect measures of microstructure; 29/267 focused on techniques that provide direct estimates of histological properties. Of the former, 213/238 were excluded as they either did not report any comparison to histology, or, if they did, only for ADC. 54/267 articles were finally included in this review. Fig. 2 summaries graphically the article screening process.

The following techniques were identified: Diffusion Kurtosis Imaging (DKI), Intravoxel-incoherent motion (IVIM) imaging, Vascular, Extracellular, and Restricted Diffusion for Cytometry in Tumors (VERDICT), Imaging Microstructural Parameters Using Limited Spectrally-Edited Diffusion (IMPULSED), Stretched Exponential Model (SEM), q-space imaging (QSI), MRI-cytometry, Restriction Spectrum Imaging (RSI), Monte Carlo (MC) simulations for microstructural mapping from clinical DW-MRI, Multidimensional Diffusion MRI (MDD-MRI), Hybrid Multidimensional MRI (HM-MRI), Diffusion-Relaxation Correlation Spectrum Imaging (DR-CSI), mpMRI-based Artificial Intelligence (AI). Some articles focussed on more than one technique.

A summary of the included techniques is given in Table 1 and Fig. 3. Techniques are grouped as phenomenological, when they parametrise the signal to surrogate parameters that do have a direct microstructural counterpart (e.g., diffusion kurtosis), or biophysical models, if they estimate specific histology features (e.g., cell size).

3.2 Technique application and MRI-histology correlation assessments

Supporting Information Tables 1-7 report in detail information on the MRI scanner and DW protocol, tissue condition during MR imaging, area of application, and information on the correlation of MRI metrics to histology for all 54 articles. This information is also included as a structured CSV data set in Supporting Information Data 1.

Fig. 4 visualises graphically information on the MRI-histology applications extracted from the selected articles. The figure shows that in most studies (about 60%), 3T MRI scanners were used (Fig. 4.A). Human tissue was used in 60% of cases, followed by mouse tissue in almost 30% of the experiments (Fig. 4.B). In the vast majority of the experiments (roughly 80%), tissues were imaged *in vivo*, while *ex vivo* imaging (of either fresh or fixed tissue) was performed in 13% of the experiments (Fig. 4.C). Finally, the analysis of the included articles reveals that the cancer application that were investigated varied considerably (Fig. 4.D). The three most commons areas of interest were, in decreasing order, cancers of the prostate (23% of the experiments), breast (16.4% of the experiments) and liver (14.8% of the experiments).

Tables 2 and 3 report correlation coefficients between DW-MRI metrics and histology (Table 2: DKI and IVIM metrics; Table 3: all other techniques). Correlations vary from weak (e.g., $r = 0.22$ for SEM parameter α with nuclear-to-cytoplasm ratio) to strong (e.g., $r = 0.92$ for IMPULSED cell diameter d with histology-derived cell size). Moreover, for some metrics correlations are not always consistent across studies (e.g., $r = 0.78$ and $r = -0.41$ for IVIM D^* and microvessel density), while for others they are (e.g., DKI ADC_K or SEM D_t are consistently negatively correlated with metrics of cellularity or cell count). Promisingly high correlations are, for example, those observed in prostate cancer for diffusion-relaxation methods (r of 0.67 and 0.90 between MRI and histological prostate lumen fraction).

3.3 Narrative description of the selected techniques

This section describes the advanced DW-MRI techniques that were used in the 54 articles included in this review, discussing the key metrics that each technique provides.

3.3.1 Diffusion kurtosis imaging

Ten articles report on Diffusion Kurtosis Imaging (DKI) [13–22] (Supporting Information Table 1 for all but [20–22], which are reported in Supporting Information Table 2 [20, 21] and 5 [22], being these articles focussed on more than one DW-MRI technique). DKI is a technique based on the diffusion signal cumulant expansion [23], and was proposed by Jensen et al. in 2005 to characterise non-Gaussian diffusion arising from presence of multiple water pools with different diffusivities, restriction, water exchange, or combination of those [24].

Signal model The DKI signal representation is

$$S \;=\; S_0 \exp\left(-b\,ADC_k \;+\; \frac{1}{6}\,K\,(b\,ADC_k)^2\right). \tag{1}$$

Above, S is the signal and b is the b-value. Unknown parameters are the non-DW signal level S_0, an ADC metric ADC_k, the excess kurtosis K ($K = 0$ for Gaussian diffusion) and the non-DW-signal S_0. ADC_k is a corrected estimate of ADC as compared to a first-order description $S \;=\; S_0\, exp\,(-b\,ADC)$ (for sufficiently low b-values, $ADC_k \approx ADC$, $K \approx 0$). K is unitless; the larger $|K|$, the stronger the departure from Gaussian diffusion (i.e., from mono-exponential signal decay). Negative K is possible, but rarely measured. In some articles, a full tensor fit is performed, and Eq. 1 is generalised to account for anisotropy in apparent diffusivity and apparent kurtosis across 3D spatial directions [18, 19]. In those cases, the authors typically focussed their analyses on mean diffusivity and mean kurtosis, which here were then taken as proxys for ADC_k and K in Table 2.

Required diffusion encoding protocol Clinical DKI is based on PGSE (i.e., LTE), with 3 mutually-orthogonal gradient directions at b-values up to approximately 1000-2000 s/mm^2. The measurement regime where estimating K becomes relevant depends on the microstructure. Typically, K cannot be neglected when the estimated ADC starts to become dependent on the maximum b-value. Signals from the 3 directions are averaged (either geometrically or arithmetically) and scalar kurtosis evaluated, rather than full tensors (required in tissues such as muscles and white matter), due to low anisotropy. To estimate S_0, ADC_k and K, sampling at least 3 b-values up to 1000-2000 s/mm^2 is required.

Fitting methods The included articles used voxel-wise, non-linear least-squares fitting, which were implemented in MATLAB [13, 14].

Main histological correlates DKI-parameters are not direct estimates of microstructural properties as cell size/density. Nonetheless, they are sensitive to several different biophysical characteristics, and can serve as indirect markers of microstructure. In four articles, K or full tensorial mean kurtosis were tested for correlation to cellularity [13, 14, 18, 19], with mixed results. In a study on ovarian cancer [13] cellularity correlated with K; in hepatocellular carcinoma (HCC) [14] and in a rabbit VX2 bone tumour model [18], it did not. Since K reflects diffusional

heterogeneity, it is possible that such variable correlations with cellularity reflect, at least in part, intra-voxel heterogeneity in cell-density [25]. Intra-cellular fraction from histology and other tissue component fractions were compared to K in renal cell carcinoma and prostate [16, 17], and results varied (correlation not always seen).

ADC_K or full tensorial mean diffusivity exhibited similar correlations as K with cellularity, but inverse. It was found to have a significant inverse correlation with cellularity [13, 18, 19], and tissue composition fractions [16, 17]. Combining ADC_k and K resulted in an even stronger correlation to cytoplasm, cellular, and stromal fraction [17].

Rosenkrantz et al. [14] found weak correlations among ADC, ADC_k and K, implying that K may offer complementary information, even if fully biologically-specific. This is supported by the fact that non-Gaussian diffusion was seen in all HCC cases ($K > 0.5$). K exhibited a higher Coefficient-of-Variation (CV) than ADC, reflecting higher sensitivity to diffusion heterogeneity, but also potentially higher sensitivity to noise.

Grussu et al. [15] mapped ADC_k and K to intra-cellular diffusivity and volume-weighted cell size at fixed diffusion time in fixed mouse livers. Cell size estimates were not accurate, but captured between-sample contrasts seen on histology.

Discussion The main advance of DKI is that it extends routine ADC mapping to account for non-Gaussian diffusion, which is quantified by the kurtosis excess K. DKI enables the description of a wider b-value range compared to ADC measurement, as it enables accounting for departures from mono-exponential signal decay. Nonetheless, DKI also has several limitations, and its practical implementation can be challenging. In order to accurately estimate the kurtosis, higher b-values than those typically acquired in the clinic are required, resulting in longer echo times and overall worse signal-to-noise ratio (SNR), as well as longer diffusion protocols, which may increase the sensitivity to motion. The higher requirements compared to ADC mapping are a limitation of virtually all advanced techniques described here, and will be given as understood when introducing the next techniques. Moreover, the estimation of the kurtosis can be ill-defined as ADC_k goes towards zero. Finally, changes in the kurtosis excess K can be due to several, different independent changes in tissue microstructure, which may be difficult to tell apart, e.g., changes in cell size, cell density, voxel heterogeneity, or water exchange.

3.4 IVIM

Intravoxel-incoherent motion (IVIM) imaging was the focus of 20 articles [20, 21, 26–43] (Supporting Information Table 2). IVIM was originally proposed in 1986 by Le Bihan et al. [44].

Signal model IVIM models two water pools (bi-exponential signal model). One describes signal from perfusion within randomly-oriented fluid-filled conduits (e.g., capillaries, blood vessels, tubules), while the other true diffusion in non-vascular tissue [44].

The overall magnitude signal attenuation in IVIM is written as

$$S \;=\; S_0 \Big((1-f)\, e^{-bD_t} \;+\; f\, e^{-bD^*} \Big). \tag{2}$$

Above, S and S_0 are the same as in Eq. 21, f is the pseudo-diffusion (vascular) signal fraction (intrinsically relaxation-weighted), D_t is the tissue ADC, and D^* is the pseudo-diffusion ADC ($D^* \gg D_t$, ranging in 10-100 μm^2/ms), and can be notated as D or D_p, for "pure". Recently, Eq. (2) has been extended to incorporate T2-effects [45] or to capture non-Gaussian diffusion [21, 46] (joint IVIM-DKI).

Required diffusion encoding protocol Body IVIM protocols typically require LTE with 3 mutually-orthogonal gradient directions at various b-values. Low b-values (up to approximately 100 s/mm^2) are densely sampled, and additional b-values are acquired up to approximately 1000 s/mm^2. Signal from the 3 directions are averaged. The number of b-values used in the included articles ranged from 5 to 11.

Fitting methods The choice of the fitting algorithm can significantly influence the quality of IVIM maps. Barbieri et al. [47] compared six algorithms for IVIM fitting in abdominal imaging (Appendix C, Table 3). Bayesian-Probability (BP)-based fitting provides the highest precision and accuracy, and minimises inter-reader/-subject variability. "Two-step fitting" is used in [20, 21, 37, 40], but without further specifications. Two articles use Levenberg-Marquardt (LM) fitting [30, 35]. Hecht et al. [30] described the fitting procedure in detail.

Main histological correlates The IVIM-parameters of the non-vascular diffusion component are often employed as markers for cellularity, while pseudo-diffusion indices are used as markers of microvessel characteristics. In five articles [20, 27, 31, 32, 40], a correlation between D_t and cellularity or related measures was found. However, in three articles [21, 29, 30], no significant correlation was found. In one study both D_t and ADC were computed; the correlation with cellularity was stronger for D_t [27]. These findings were however not supported by four other studies [21, 26, 29, 31].

Conversely, f and D^* rarely correlated with cellularity, although some weak correlation with the level of necrosis was seen in [42]. In [43], a negative correlation between both f and D^* with liver cell size following hepatectomy was reported. Correlation with measures of vessel density was tested in thirteen articles. In ten articles, a significant correlation was reported [29, 33–37, 39–42], while in three no correlation was found [21, 30, 31]. For example, f and D^* correlated positively with Microvessel Density (MVD) [41, 42]. D^* also correlated positively with the Pericyte Coverage Index (PCI), while D_t correlated negatively with the Vasculogenic Mimicry (VM) [41].

Discussion IVIM enables the joint estimation of tissue diffusion properties as well as characteristics of the local microvasculature, which may be useful in a variety of oncological applications, being abnormal vasculature a key characteristics of cancer. However, the practical implementation of IVIM in real-world clinical contexts faces a number of hurdles.

Firstly, a large number of b-value measurements are required. If one wants to accurately characterise both true-diffusion/pseudo-diffusion components, very long acquisitions may be required.

IVIM oversimplifies the true microstructure, as it models only two compartments, pooling all non-vascular contributions into a surrogate tissue component. Also, it does not account for inter-compartment exchange [48], compartment-wise relaxation [45] and diffusion time dependence [1]. Because of this, IVIM parameters may be considered semi-quantitative.

Moreover, the included articles demonstrate clearly that there is currently a lack of standardisation of both fitting procedure and acquisition protocol, which may be one of the leading factors behind the relatively poor reproducibility of IVIM metrics.

Finally, several studies [30–34] report that IVIM-parameters do not perform well in terms of repeatability (especially f, D^*). Flow-compensated acquisitions improve IVIM robustness [49, 50], but may not be available in all scanners. Efforts are also ongoing to optimise the clinical protocol and facilitate standardisation [51].

3.5 VERDICT

Eight articles reported on VERDICT [52–59] (Supporting Information Table S3). This model was originally proposed by Panagiotaki et al. (2014) [55].

Signal model VERDICT is a biophysical, multi-compartment model fitted on DW-MRI measurements acquired at varying b-values, diffusion times and gradient directions with standard linear tensor encoding (PGSE). The model, developed on colorectal cancer xenograft mice [55], has shown utility *in vivo* in prostate imaging [60] and in other contexts (e.g., rhabdomyosarcoma).

VERDICT models three non-exchanging water pools:

- water in the intra-cellular space (restricted diffusion within spherical cells);
- water in the extra-cellular extra-vascular space (EES) (hindered diffusion in stroma and lumen, outside cells/vessels);
- water in the vascular compartment (pseudo-diffusion within blood vessels/tubules).

The total signal is written as

$$S \;=\; S_0 \left(f_{ic}\, S_{ic}(d_{ic}, R) \;+\; f_{EES}\, S_{EES}(d_{ec}) \;+\; f_{vasc}\, S_{vasc}(d_{vasc}) \right). \tag{3}$$

Above, b is the b-value; $d_{ic,ec,vasc}$ are the intrinsic diffusivity of the intra-cellular space (d_{ic}) and the EES/vascular ADCs (d_{ec}/d_{vasc}). R is cell radius, while the $f_{ic,EES,vasc}$ are relaxation-weighted signal fraction ($f_{ic} + f_{EES} + f_{vasc} = 1$). A recent article by [59] extended the VERDICT model (relaxation-VERDICT) to account for compartment-wise relaxation properties.

Required diffusion encoding protocol VERDICT requires a rich PGSE protocol with several b-values and diffusion times (i.e., varying Δ/δ). The different diffusion times may be sampled at the expense of varying the TE, a fact that has been exploited in recent relaxation-VERDICT [59]. Sampling different diffusion times at different diffusion-weighting strengths provides sensitivity to cell size and cellularity due to restriction (intra-cellular space) or tortuosity (extra-cellular space), a phenomenon known as time-dependent diffusion (TDD) [1].

Recently, Double Diffusion Encoding (DDE) VERDICT (made of two consecutive PGSE blocks; Appendix A) improved f_{ic} and R estimation [54].

Fitting methods VERDICT is generally fitted with f_{EES}, f_{ic}, R as free parameters ($f_{vasc} = 1 - f_{ic} - f_{EES}$) and $d_{ic,ec,vasc}$ fixed (and $d_{ic} = d_{ec}$), using an iterative optimisation procedure [52, 55, 57]. The optimisation is non-linear, via LM algorithm (see Table 4, Appendix C). VERDICT can also adopt different compartment-wise anisotropy, depending on the cancer type [55, 57, 61]: optimal compartment shape has been investigated with the Akaike Information Criterion (AIC) [53]. Accelerated Microstructure Imaging via Convex Optimization (AMICO) fitting was used to speed up signal processing, without jeopardising fitting accuracy [52]. An article [62] reported a method based on General Adversarial Networks (GANs) to synthesise VERDICT parameters from routinely acquired DW-MRI, suitable for ADC mapping. Methods of this type may be useful in clinical settings, but should be interpreted with care: microstructural information that is not encoded in the signal cannot be retrieved. The recent relaxation-VERDICT implementation was instead fitted using DNNs [59], resulting in lower metric variability, higher scan-rescan repeatability and higher accuracy in parameter estimation.

Main histological correlates All included articles were on prostate cancer, except for one on rhabdomyosarcoma [54] and one on colorectal cancer [55]. In the included articles, low/high f_{ic} was found to mirror areas of low/high cellularity [53], a promising finding for potential applications in clinical trials. R was shown to be highly variable in areas of high lumen density. The quantitative comparison between VERDICT parameters and histology showed that VERDICT parameters are correlated with their histological counterparts [55], and the level of agreement increases when tissue shrinkage due to histology processing is taken into account. Importantly, it can discriminate Gleason grades. The classical VERDICT implementation distinguishes benign prostate lesions from Gleason grade 3+3, and 3+3 from 3+4. In additional, relaxation-VERDICT also distinguishes 3+4 from 4+3 or higher [59].

Discussion In three studies, a comparison was executed between VERDICT, ADC, IVIM, and DKI [55, 57, 60]. The most important benefit of VERDICT over the other techniques is that VERDICT describes specific histological factors, while the others provide surrogate indices of tissue microstructure [60]. Nonetheless, a joint quantitative benchmarking of these techniques against histology was executed in only one study, and further validation of VERDICT is required.

In VERDICT, a tailored acquisition is required to sample high b-values (up to ≈ 3000 s/mm^2) and various Δ, δ, and potentially TE in recent VERDICT extensions [59]. This results in demanding acquisitions, as for DKI

[55, 62].

Concluding, VERDICT is a promising technique providing sensitive markers of specific histological properties, and variations in the acquisition/analysis (AMICO, DDE, GANs, DNN-fitting, joint diffusion-relaxation modelling), may strengthen its clinical feasibility. Its main advantage is that it attempts to disentangle independent factors that can contribute to the diffusion contrast, striving to provide quantitative estimates of relevant biophysical properties such as cell size or density. Its main disadvantage is that it relies on a biophysical model that makes strong assumptions on the underlying characteristics of the diffusion process (e.g., it neglects water exchange; it assumes a fixed diffusivity in the intra-cellular compartment), which has not been fully validated yet. Moreover, it relies on a long acquisition protocol, which may be impractical in certain clinical contexts where scan time is limited.

3.6 IMPULSED

Seven articles report on IMPULSED [63–69] (Supporting Information Table S4), which is based on Temporal Diffusion Spectroscopy (TDS), a framework that exploits TDD to resolve restriction lengths combining PGSE and oscillating gradient spin echo (OGSE). This method was proposed by Jiang et al. (2017) [66].

Signal model IMPULSED models two non-exchanging compartments, describing intra-/extra-cellular water, i.e.,

$$S \;=\; f_{ic}\, S_{ic} \;+\; (1 - f_{ic})\, S_{ec}, \tag{4}$$

where f_{ic} (also known as v_{in}) is the relaxation-weighted intra-cellular signal fraction, S_{ic}/S_{ec} intra-/extra-cellular signals. S_{ic} is modelled by diffusion within spheres of diameter d, with intrinsic cytosol diffusivity d_{ic}. S_{ec} is modelled as

$$S_{ec}(b) \;=\; exp(\, -b\, d_{ec}\,). \tag{5}$$

d_{ec} is approximately linear as a function of the OGSE frequency f [63–66] ($d_{ec} = d_{ec,0} + \beta f$), while it does not depend on δ/Δ in PGSE. A cellularity index can be obtained by combining d and f_{ic} [66], similarly to [60].

In the original IMPULSED, signal contributions from perfusion are ignored and intra-/extra-cellular exchange assumed to be negligible. In a study of Jiang et al. [63], a third compartment is added to describe the effect of vasculature. Li et al. [67] investigate the influence of water exchange, suggesting that it can be ignored if the diffusion time is at least one order of magnitude smaller than the intra-cellular water lifetime τ_{in} ($\geq$ 30 ms). Recently, water exchange was incorporated by Jiang et al. [69] in IMPULSED. This improved fitting accuracy and provided additional τ_{in} and cell membrane permeability P_m estimates.

Required diffusion encoding protocol IMPULSED utilises LTE with both OGSE, probing ultra-short diffusion times maximising sensitivity to cell size [66, 68]), and routine PGSE wave forms. To obtain microstructural in-

formation for common cell types, diffusion times in the range of approximately 1-70 ms are required [63]. Also, b-values up to approximately 1000 s/mm^2 are used.

Fitting methods Fitting is performed via constrained non-linear least square optimisation. d_{ic} (intrinsic intracellular cytosol diffusivity) is fixed in most studies (e.g., 3 μm^2/ms [63]) to increase precision [63, 64, 68].

Main histological correlates Comparisons to histological references were found for f_{ic} and d. f_{ic} is underestimated with respect to histology [63, 64, 66, 67, 69], potentially due to unaccounted water exchange [66, 69]. The cell size estimate d is less influenced by exchange and is moderately or strongly correlated with histology [63–67, 69].

Discussion Similarly to VERDICT, IMPULSED relies on a multi-compartment model to disentangle key properties of intra-/extra-cellular diffusion, providing metrics of cytometry designed to be highly specific to histology. Practically, IMPULSED combines OGSE and PGSE to probe a wide range of diffusion times t_{diff} (approximately 1.7-52 ms) as this improves microstructural inference of cell size. However, such a requirement can hinder the practical implementation of the technique. The t_{diff} range that can be probed depends on the maximum available gradient strength [65], and by the fact that OGSE may not be readily available in commercial scanners [68].

In conclusion, IMPULSED is potentially clinically-feasible, as long as the required gradient magnitudes are achievable and OGSE sequences are available. It provides histologically-meaningful cell size indices (d), while accurate f_{ic} estimates are more difficult to obtain, especially if water exchange is not accounted for.

3.7 Stretched Exponential Model

In three papers, SEM, a technique developed by Bennett et al. in 2003 [70], was mentioned [17, 33, 71], despite not being the primary focus of the study (see Supporting Information Table S1 and S5).

Signal model SEM, a special case of Fractional Order Diffusion, attempts to quantify diffusion heterogeneity by introducing a heterogeneity index α, such that

$$S \;=\; S_0 \; exp(\,-(b\,D_{SEM})^{\alpha}\,). \tag{6}$$

S, S_0, b have the same meaning as described earlier, while α ranges from 0 to 1. α close to 1 implies low diffusion heterogeneity (i.e., diffusion approximately Gaussian; mono-exponential decay). Conversely, the closer α to 0, the more heterogeneous the diffusion process. D_{SEM} is the mean intra-voxel diffusion coefficient.

Required diffusion encoding protocol The protocol requirements are similar to those of DKI, namely, standard LTE with at least two non-zero b-values plus one or more non-DW images. In body imaging, 3 directions per b-value are typically acquired and averaged, and the diffusion time and TE are generally fixed for all b-values. The maximum b-value used in SEM is around 2000 s/mm^2.

Fitting methods SEM parameter maps are typically obtained via non-linear least squares fitting.

Main histological correlates Two papers compared SEM to histological indices [17, 71]. D_{SEM} shows similar negative histological correlation with cellularity. Correlation figures for α are weaker. Nonetheless, linear regressions that include both D_{SEM} and α predict histological cellularity better than D_{SEM} alone [17], implying that α may carry sensitivity to microstructure.

Discussion SEM provides a framework that enables the characterisation of departures from Gaussian diffusion and mono-exponential decay through diffusion heterogeneity. SEM provides useful information on microstructure that generalises routine ADC. However, it suffers from similar issues as the techniques described above. Firstly, its metrics are only semi-quantitative, as they may vary with varying diffusion protocols (e.g., due to changes in the diffusion times). Morevoer, SEM has an unphysical nature, as the exponent parameter α does not have any biophysical meaning [72]. Finally, it requires longer acquisition protocols and higher b-values than routine ADC mapping, due to its higher number of parameters. This comes at the price of reductions in SNR, as well as potentially higher susceptibility to motion.

3.7.1 q-space imaging

q-space imaging (QSI) was the focus of two articles [71, 73]. QSI is a phenomenological technique that recovers the spin displacement distribution due to diffusion, developed by the seminal work of Callaghan [74].

Signal model QSI enables the estimation of the probability density of diffusion displacement $\mathbf{r}$ due to diffusion over a time t ($p(\mathbf{r}, t)$), known as *diffusion propagator*. The estimation of the propagator is made possible by the fact that the DW-signal measured as a function of the q-value $\mathbf{q} = \gamma\,\delta\,G\hat{\mathbf{g}}$ (with G, δ and $\hat{\mathbf{g}}$ being the gradient strength, duration and direction) at a fixed gradient separation Δ in the short gradient pulse limit ($\delta \ll \frac{L^2}{D_0} \ll \Delta$ [75], where L is the compartment size and D_0 the intrinsic diffusivity), is the Fourier transform of $p(\mathbf{r}, t = \Delta)$, which can can be estimated by inverse Fourier-transforming DW measurement sets $S(\boldsymbol{q}, \Delta)$ [3, 76], i.e.,

$$p(\mathbf{r}, \Delta) \;=\; F^{-1}\left\{S(\mathbf{q}, \Delta)\right\}. \tag{7}$$

Required diffusion encoding protocol For QSI, rich protocols based on LTE PGSE are typically required. A high number of measurements is required to sample the q-space and enable accurate inverse Fourier transformation. For example, in [71, 73], 32 b-values up to 7163 s/mm^2 were used.

Fitting methods The propagator in Eq. 7 is estimated via practical numerical implementations of inverse Fourier transformation, such as the Fast Inverse Fourier Transform [71]. Ad-hoc methods have also been proposed in the literature for the estimation of the propagator and of its salient properties, such as diffusion spectrum imaging (DSI, 2005) [77], or Mean Apparent Propagator MRI (MAP-MRI, 2013) [76]. Multiple metrics can be used to characterise

$p(\mathbf{r}, \Delta)$, e.g., mean displacement (MD) or mean squared displacement (MSD) [73], measurement of displacement probability (such as the probability of zero displacement (PZD [73]), or the return-to-origin/axis/plane probabilities (RTOP, RTAP, RTPP) from MAP-MRI [76]), or the kurtosis [73] of the full-width-at-half-maximum (FWHM) of the propagator itself [71].

Main histological correlates In [73], MD correlated negatively with nuclear cytoplasmatic ratio and tumor cellularity, while PZD and Kurtosis correlated positively with both features. In [71], the FWHM and its skewness correlated negatively with cellularity and skewness of cellularity respectively.

Discussion QSI offers the advantage of reconstructing in full the diffusion propagator, enabling the characterisation of several different features of non-Gaussian diffusion. The included articles demonstrate that QSI is sensitive to changes in microstructure [71, 73]. Specifically, measures of water displacements derived from the propagator correlate with cellularity/cell density. Potential drawbacks of QSI are that its metrics are surrogate markers with limited biological specificity, since several different, independent factors can cause alterations of the propagator. Moreover, the propagator is intrinsically diffusion-time dependent, implying that QSI metrics are semi-quantitative, being protocol dependent. Finally, QSI acquisitions are more demanding than those required for ADC measurement.

3.7.2 MRI-cytometry

MRI-cytometry is a two-pool intra-/extra-cellular biophysical framework for mapping cell size distributions, proposed by Xu et al. [78], which is one of the articles selected in this review (see also Supporting Information Table S5).

Signal model The MRI-cytometry model is a two-compartment model that describes the signal as arising from the sum of intra-cellular and extra-cellular, extra-vascular components, without inter-compartment exchange, i.e.,

$$S \;=\; S_{ic} + S_{ec}. \tag{8}$$

Both intra-/extra-cellular signals are described as the sum of a continuous distribution of spin packets with fixed properties. For a b-value b and a diffusion time τ, the these are written as

$$S_{ic} \;=\; \int_{d_{ic}} \int_{R} \rho_{ic}\, \frac{8\pi}{3} (R)^3\, a_{ic}(d_{ic}, R)\, P(d_{ic}, R)\, d\, d_{ic}\, dR \tag{9}$$

for the intra-cellular signal and

$$S_{ec} \;=\; \int_{d_{ec,0}} \int_{\beta} \rho_{ec}\, e^{-b(d_{ec,0} + \frac{\beta}{\tau})}\, P(d_{ec,0}, \beta)\, d\, d_{ec,0}\, d\beta \tag{10}$$

for the extra-cellular signal. Above, d_{ic} is the intrinsic intra-cellular diffusivity, $d_{ec,0}$ is the asymptotic extra-cellular ADC, R is the cell radius, β is the extra-cellular TDD factor, ρ_{ic} and ρ_{ec} are the unit signal per unit volume coming from the intra-cellular and extra-cellular compartment respectively, and $a_{ic}(d_{ic}, R)$ is the characteristic signal of a cell with radius R and cytosol diffusivity d_{ic}.

Required diffusion encoding protocol As IMPULSED, MRI-Cytometry utilises LTE with both OGSE and PGSE wave forms. The technique has been demonstrated *in vivo* on a clinical system using diffusion times τ of 70, 10, and 5 ms, with the highest b being of 1800 s/mm^2, 1000 s/mm^2, and 300 s/mm^2 for each τ.

Fitting methods The MRI-cytometry model is fitted after constructing a discrete dictionary of candidate intra-/extra-cellular signals, following a two-step regularised non-linear least square procedure [78]. This provides estimates of the joint probability density functions $P(d_{ic}, R)$ and $P(d_{ec,0}, \beta)$ in each voxel. Integrating $P(d_{ic}, R)$ over d_{ic} enables mapping the cumulative cell size distribution, whose peaks can be used to identify different cell populations with remarkably different average cell sizes.

Main histological correlates The authors report a good match between cell size estimates and references from cell cultures *in vitro*. However, correlation coefficients were not calculated, owing to the small sample size.

Discussion MRI-Cytometry is essentially a more complex implementation of IMPULSED. The technique can potentially provide more in-depth information on the different cell types present in a voxel (e.g., small lymphocytes vs larger cancer cells), as it enables recovering a full cell size distribution, rather than a single cell size index per voxel, as IMPULSED. However, the more complex model comes at the expenses of more complex parameter estimation, which is even more prone to instabilities, and requires regularisation. Finally, similarly to IMPULSE, the technique requires combining LTE with OGSE and PGSE wave forms. The former are typically not available in vendor-provided diffusion sequences, and may therefore be an hurdle for its practical clinical implementation.

3.7.3 Restriction Spectrum Imaging

Restriction Spectrum Imaging (RSI) was the focus of two articles included in this review [22, 79] (Supporting Information Table S5). RSI was proposed in brain imaging by White et al.[80].

Signal model The method models the DW-signal as arising from a distribution of diffusion tensor components. The components with the slowest diffusion are used as proxies for water restricted within cells. Different RSI implementations vary depending on the number/characteristics of the components. One of the RSI articles included in this review used three-component for discriminating rectal cancer grades [22], i.e.,

$$S \;=\; S_0 \left(C_1\, e^{-bD_1} \;+\; C_2\, e^{-bD_2} \;+\; C_3\, e^{-bD_3} \right) \;\; s.t.\; D_1 < D_2 < D_3, \tag{11}$$

where $C_{1,2,3}$ are relaxation-weighted signal fractions for restricted, hindered, and free water, while $D_{1,2,3}$ ($D_i < D_{i+1}$) their ADCs.

Required diffusion encoding protocol RSI can be performed at fixed diffusion time and it has been implemented with protocols as short as 5 minutes. The method has been demonstrated using LTE PGSE with maximum b-values as low as 1000 s/mm^2 in [79] and 2000 s/mm^2 in [22], i.e., using the same protocols that one could employ for DKI.

Fitting methods Eq. 11 is typically fitted using non-linear least square approaches. During fitting, the ADCs of the different diffusion components are not estimated, but rather fixed to characteristics values. For example, in [22] the following values were used: $D_1 = 0.5$ μm^2/ms (restricted diffusion), $D_2 = 1.3$ μm^2/ms (hindered diffusion), $D_3 = 3.0$ μm^2/ms (free water diffusion). After fitting, signal fraction maps can be standardised in the form of z-scores using reference values from healthy tissue, e.g., from the healthy prostate, as in [79].

Main histological correlates Yami et al. [79] used RSI to estimate cellularity in prostate cancer, detecting variations of Gleason Grade within a single tumour. Similarly, in [22], the restricted signal fraction C_1 correlated with rectal cancer grade.

Discussion RSI is a promising techniques that attempts to disentangle different sub-voxel signal sources, providing signal fraction maps designed to be specific to characteristics cellular components. The technique is based on a multi-component representation that can fitted more easily than multi-compartment models such as IMPULSED, being the properties of such components fixed (i.e., pre-specified D_i values). However, this comes at the price of potential biases in the signal fraction maps, since the characteristics ADCs of the different sub-voxel components are likely to vary on a voxel-by-voxel basis. Moreover, RSI modelling does not take into account explicitly the diffusion time, implying that its metrics are likely to be protocol dependent. Regarding the acquisition, RSI requires more complex protocols than routine ADC measurement. Nonetheless, it has been demonstrated with compact scan times under 10 minutes, which offer promise for clinical translation.

3.7.4 MC simulations for microstructural mapping from clinical DW-MRI

One article [81] (see also Supporting Information Table S5) investigated microstructural parameter estimation from clinical DW-MRI informed by MC simulations in skull-base chordoma cases treated with radiotherapy.

Signal model The technique essentially aims to map several ADC values obtained from different sub-protocols of multi b-value clinical DW-MRI, to microstructural parameters that are more specific to the underlying tissue histology: cellular radius R, cell volume fraction f_{ic}, cell diffusivity d_{ic} and apparent cellularity ρ_{app}.

Fitting methods The mapping $(ADC_1, ..., ADC_N) \rightarrow (f_{ic}, R, d_{ic}, \rho_{app})$ is achieved by comparing voxel-wise ADC maps to sets of synthetic, candidate ADCs values generated via Monte Carlo simulations. The comparison involves multiple steps, and accounts explicitly the uncertainty of the estimation of each microstructural parameter due to noise. Monte Carlo simulations were performed within synthetic cancer micro-environments in the form of 3D meshes.

Required diffusion encoding protocol The approach has been demonstrated with routine PGSE LTE, which included 3 b-values (50, 400, 1000 s/mm^2).

Main histological correlates Microstructural maps were related to the cancer aggressiveness as measured by Ki-67 immunohistochemistry. All estimated tissue parameters differed between more vs less proliferative tumours (i.e., high Ki-67 vs low Ki-67 immunostain) [81]. Moreover, statistical survival models that combined all microstructural parameters could predict the risk of progression following radiotherapy with high accuracy.

Discussion The approach presented by Morelli et al. [81] is promising in that it enables clinically feasible estimation of microstructure metrics without any further assumptions than those that go into the simulations [82]. The framework relies on simulations of diffusion that can be performed on synthetic cancer micro-environments, and that can therefore incorporate unprecedented levels of microstructural details. On the one hand, this removes the need for developing analytical expressions of the signal based on over-simplified geometric models of the tissue (e.g., modelling cells as spheres, as in VERDICT or IMPULSED). On the other hand, the approach can potentially enable the mapping of indices of cell heterogeneity, e.g., measures of dispersion in cell size or morphology. Despite its potential, the method remains complex to be deployed in practice, since most centres may not have the capabilities to run Monte Carlo simulations of the very specific DW-MRI sequences being used at the centre. The approach has shown potential clinical utility, but the microstructural parameters have still to be validated by comparisons to their direct counterparts from histology.

3.7.5 Multidimensional Diffusion MRI

Multidimensional Diffusion (MDD) MRI, also known as b-tensor encoding or q-space trajectory imaging, makes use of generalised diffusion gradient wave forms [4]. The approach, pioneered *in vivo* by Westin and Nilsson [4] after pre-clinical development by Topgaard, Eriksson and Lasic [83, 84], was investigated by Naranjo et al. [85], an article included in this review (Supporting Information Table S5).

Signal model In MDD, diffusion-weighting is described in terms of a b-tensor $\mathbf{B}$, rather than by scalar b-values. $\mathbf{B}$ is defined as

$$\mathbf{B} = \int_0^{TE} \mathbf{q}(t)\ \mathbf{q}(t)^{\mathrm{T}}\, dt, \tag{12}$$

where $\mathbf{q}(t) = \gamma \int_0^t \mathbf{g}(\xi)\, d\xi$, with the diffusion gradient $\mathbf{g}(t)$ free to change its direction during encoding. This sensitises measurements to different diffusion directions at once, probing a new contrast that is not accessible to PGSE [86–88], and disentangling heterogeneity in isotropic diffusivity from diffusion heterogeneity caused by anisotropy. Different methods have been proposed to analyse data acquired with b-tensor encodings beyond standard LTE PGSE or OGSE. These typically express the DW signal in terms of a continuous distribution of microscopic domains, each characterised by a specific diffusion tensor [89], i.e.,

$$S(\mathbf{B}) = S_0 \int P(\mathbf{B})\, e^{-\mathbf{B}:\mathbf{D}} d\mathbf{D}. \tag{13}$$

Above, $\mathbf{B}$ is the acquisition b-tensor, $\mathbf{D}$ is the diffusion tensor of the generic diffusion component, $P(\mathbf{D})$ is the diffusion tensor distribution (DTD), and : denotes the double inner product between the diffusion-/b-tensors.

Required diffusion encoding protocol MDD-MRI protocols typically entail a variety of b-values sampled with different b-tensor encoding shapes, e.g. combinations of LTE, spherical tensor encoding (STE) and planar tensor encodings (PTE). While STE and PTE may not be available off-the-shelf in vendor-provided DW-MRI sequences, several works have now developed robust implementations across multiple system platforms and manufactures, which have shown excellent stability and reproducibility [90].

Fitting methods B-tensor encoding parametric maps are typically recovered by parametrising the signal as a function of different features of the DTD, depending on the tissue of interest. For example, the signal can be parametrised as function of the overall mean diffusivity ($\bar{D}$) and the anisotropic and isotropic diffusional variance (V_A and V_I) [90], or via cumulant expansions of the DTD [4]. Fitting is then performed via non-linear least square optimisation, and once the DTD parameters have been recovered, other microstructural parameters of interest can be derived analytically, e.g., microscopic fractional anisotropy.

Main histological correlates The authors in [85] used LTE and spherical-tensor encoding to obtain metrics as D_{iso} (isotropic diffusivity) or D_{Δ^2} (shape parameter of diffusion anisotropy, similar to V_A) of the various tensors making up the DTD. Cancer and healthy tissue differed according to nearly all DTD metrics. However, histological data were only assessed mainly qualitatively, as also done, for example, in the prostate [86].

Discussion MDD MRI has expanded the capabilities on in vivo DW-MRI, giving access to new diffusion contrasts that cannot be probed with conventional diffusion imaging. These may enable disentangling subtle microstructural differences that would be indistinguishable in conventional PGSE, ultimately providing useful biomarkers in several types of body cancer. Despite its potential, at present the practical clinical use of MDD is challenged by the limited availability of b-tensor encoding as an off-the-shelf product sequence. Moreover, b-tensor DTD metrics, while surely promising, are phenomenological indices that are sensitive to different features of the underlying microstructure. Histological validation is ongoing in a variety of clinical contexts [25] to confirm their specificity, and

to rule out confounding factors that have not been account for yet. Finally, it should be noted that MDD also comes with some challenges. For example, it has proven difficult define exactly the sequence effective diffusion time in presence of irregular, oscillatory gradient wave forms, as those required for the efficient implementation of STE and/or PTE. This implies that strong differences in diffusion time across different b-tensor implementations, if not accounted for, may confound the values of DTD metrics across scanners, and could therefore hinder the deployment of these metrics as quantitative markers in clinical settings.

3.7.6 Hybrid Multidimensional MRI

Two papers used HM-MRI [91, 92], proposed by Chatterjee et al. in 2018 [93] (see Supporting Information Table S6).

Signal model HM-MRI models the signal as the sum of lumen, stroma and epithelium components:

$$S \;=\; S_0 \left(\sum_{n=1}^{n=3} V_n \; e^{-b\, ADC_n \, - \frac{TE}{T_{2n}}} \right). \tag{14}$$

Above, V_n, T_{2n}, and ADC_n are signal fractions, T2, and ADC of lumen, stroma, and epithelium water ($n = 1, 2, 3$), which are fitted by imposing upper/lower bounds [93].

Required diffusion encoding protocol HM-MRI requires standard LTE PGSE acquisitions. Images at multiple b-values and multiple echo times TE are used, with three or more directions per unique (b,TE) value, which are averaged. The maximum b-value required for HM-MRI is around 1500 s/mm^2. Regarding TE, values as high as 200 ms or more are needed to appreciate the T2-decay of lumen water, known to feature a much longer T2 than the stromal or epithelial components. HM-MRI has been demonstrated using at least 9 unique (b,TE) acquisitions [93].

Fitting methods Eq. 14 is fitted via non-linear least square optimisation, imposing upper/lower bounds on compartment-wise ADC and T2 values [93]. For example, the lumen signal component is assigned the highest ADC and longest T2, while the epithelial signal component the lowest ADC.

Main histological correlates Tissue composition changes were observed in presence of prostate cancer and reflected different histological grades. For instance, an increased epithelium and reduced lumen fractions were found in tumours [91]. HM-MRI fractions of lumen, epithelial, and stromal signal agree excellently with counterparts derived from histology [91], and matched well with expert interpretation [92].

Discussion HM-MRI is a diffusion-relaxometry method, which aims to resolve diffusion and relaxation properties jointly in each voxel through multi-contrast readouts [94, 95]. Joint diffusion-relaxometry imaging may be beneficial when TR or TE are changed as part of the diffusion encoding protocol (e.g., due to restrictions imposed by MRI

manufactures [60]), or to account for the TE-dependence of multi-compartment signal fractions [45]. Results from the papers included in this review suggest that HM-MRI offers promise from clinical translation, given its excellent agreement with histology and its easy-to-implement protocol, requiring approximately 10 minutes. However, HM-MRI suffers from similar issues as methods such as DKI or RSI: its metrics may be protocol-dependent, since they i) do not take into account sequence parameters such as the diffusion time (which may vary across b-values due to changes in TE), and ii) rely on assumption on the characteristics ADC and T2 of the different prostate components, which are unlikely to hold across all prostate voxels. Finally, the long TE required by HM-MRI jeopardises the overall SNR, and acquisition protocols are more demanding than those required for ADC measurement.

3.7.7 Diffusion-Relaxation Correlation Spectrum Imaging

Diffusion-relaxation Correlation Spectrum Imaging (DR-CSI) was proposed by Kim et al. in 2017 [96] and de Almeida Martins and Topgaard in 2018 [97], after pioneering DR-CS work in spectroscopy in the early 2000s [98]. Two papers included in this review focussed on DR-CSI [99, 100] (Supporting Information Table S6).

Signal model In DR-CSI, no predefined number of compartments has to be defined [99], being the signal dependent on a continuous ADC-T2 distribution $p(ADC, T_2)$, i.e.,

$$S(b, TE) \;=\; S_0 \int_0^\infty \int_0^\infty p(ADC, T_2)\; e^{-b\,ADC\,-\,\frac{TE}{T_2}}\; dADC\; dT_2. \tag{15}$$

Required diffusion encoding protocol DR-CSI is similar to HM-MRI, in that it requires multiple LTE with PGSE wave forms, acquired at varying b-values and TE. In body imaging the technique has been demonstrated on *ex vivo* prostate scanned on a clinical system with 16 unique (b,TE) encodings [99], for a maximum b of 1500 s/mm^2 and maximum TE of 120ms.

Fitting methods $p(ADC, T_2)$ (the ADC-T2 spectrum) can be recovered via inverse-Laplace transformation or related numerical approaches [94]. In [99], $p(ADC, T_2)$ non-negative non-linear least square regression with total variation spatial regularisation was used. Peaks in $p(ADC, T_2)$ provide component fraction maps and characteristic ADC/T2 [94, 99]. Other fitting approaches are based on defining a pre-specified number of normative spectral component, for example drawing regions-of-interest in tumours and/or normal tissue. The fraction of each component is then mapped voxel-wise using regularised spectral analysis with cross-subject spectral standardisation [100].

Main histological correlates In [99], which focussed on prostate imaging, three signal components were detected, and found to correspond to histological epithelium, stroma and lumen, with promising significant positive correlations. The study only focussed on *ex vivo* data, and *in vivo* confirmation is required. Conversely, [100] tested whether DR-CSI enables the non-invasive grading of clear cell renal cell carcinoma. The authors identified 5 different ADC-T2 spectra in the kidney, and mapped the signal fraction of these spectra voxel-by-voxel. Two of

these signal fraction maps correlated with cancer grade from histopathological assessment of HE-stained sections obtained from nephrectomy.

Discussion Considerations for DR-CSI are essentially equivalent to those discussed above for HM-MRI. The method is promising as it enables disentangling different water pools within a voxel. As compared to HM-MRI, DR-CSI does not make any assumption on the number and characteristics of ADC-T2 component, and can therefore provide higher specificity to biology: peaks in the ADC-T2 spectrum can be assigned to specific components (e.g., to stroma, rather than epithelium) by means of pilot MRI-histology correlation analyses. However, resolving a full ADC-T2 spectrum is inherently more challenging, so this could come at the expenses of higher metric variability and/or blurring of information due to the strong regularisation required for stable fitting. Finally, as for HM-MRI, DR-CSI requires very long TE, which reduce SNR, and does not take into account changes in diffusion time during the acquisition (likely to happen in clinical systems owing to changes in TE). Ultimately this may confound at least in part the recovered ADC-T2 spectra, and lead to sub-optimal protocol-dependent metrics. However, this is merely a practical limitation owing to current practices in sequence design, which could be easily mitigated by scanner software upgrades.

3.8 mpMRI-based AI

Finally, one paper reported on methods predicting histology indices from multi-parametric MRI (mp-MRI) [101] with AI (Supporting Information Table 7).

Signal model This approach is general and flexible, in that it relies on training AI systems that predict histological properties directly from mpMRI images and, potentially, easy-to-get parametric maps, as for example routine ADC as provided by the MRI scanner as part of any clinical mpMRI implementation.

Required diffusion encoding protocol The approach has been demonstrated on prostate mpMRI, which includes high resolution anatomical T2-weighted images, DW-MRI with at least one non-zero b-value for ADC calculation, plus, potentially, other contrasts, such as T1-weighted anatomical imaging and/or dynamic contrast-enhanced (DCE) MRI.

Fitting methods Histological images were co-registered to MRI and AI algorithms such as Deep Neural Networks (DNNs) were trained to map MRI directly to histology. The user potentially does not require to perform any DW-MRI signal model fitting, since simple parametric maps such as ADC provided by the scanner in clinical mpMRI can be stacked as inputs of the DNNs.

Main histological correlates Sun et al. [101] estimated prostate cell density from mp-MRI with a generalised additive model (GAM).

Discussion The study shows promising MRI-histology correlations, with minimal requirements in terms of the diffusion protocol. Nevertheless, the approach is challenged by several issues that are typically encountered in AI-based methods. First of all, large, high-quality data sets of co-localised mpMRI and histology data - *per se* very difficult to obtain - are needed to robustly train the AI systems. These should include mpMRI protocols acquired with a variety of approaches, field strengths, resolutions, contrasts, etc, and in a variety of clinical contexts, to ensure generalisability of the results. Secondly, extensive validation is needed to ensure that the trained AI system do not provide histology predictions with hallucinated features.

4 Discussion

4.1 Summary

We reviewed systematically the state-of-the-art of advanced DW-MRI in body imaging in cancer (beyond the central nervous system, i.e., mainly abdominal/pelvic imaging; and beyond routine ADC), analysing its value in tissue microstructure assessment. Many different techniques were found, with the most common being IVIM, DKI, VERDICT and IMPULSED, and other gaining momentum, e.g., MDD or diffusion-relaxation MRI. All these methods add additional degrees of freedom to routine diffusion protocols, increasing the measurement space so that more microstructural information can be encoded in the signal, as illustrated in Figure 5. This is done by acquiring extra b-values (e.g., IVIM, DKI, RSI), by varying diffusion times (e.g., VERDICT, IMPULSED) or TE (e.g., HM-MRI), or by using new gradient wave forms (e.g., MDD). These approaches have their own strengths and limitations, and their clinical feasibility depends on requirements for non-standard sequences, maximum b, or scan time. A practical example of a rich acquisition in this high-dimensional measurement space is provided in Figure 6. The figure shows a breast cancer liver metastasis imaged at 3T with a diffusion-relxation protocol, where four different b-values are acquired with LTE at 3 different echo times TE. The images reveal faster signal decay with increasing b-value within the tumour core, likely indicative of necrotic areas, which are surrounded by active tumour.

4.2 Routine DW-MRI: ADC mapping

ADC mapping was not included in this review, as it is extensively covered elsewhere. Our article focusses explicitly on methods that go beyond routine ADC measurement, and for which histological validation has been carried out. This explains the number of articles included in the review, i.e., 54.

ADC is, by construction, a surrogate, semi-quantitative metric that pools into one number several microstructural sources of diffusion contrast. Moreover, its actual numerical value depends strongly on the interaction between the DW-MRI acquisition protocol and the underlying microstructure, making it a semi-quantitative, protocol-dependent index. Despite these well-known limitations, ADC has also shown some potential clinical utility in several oncological applications, some of which are briefly discussed below for the benefit of the readership. For example, DW sequences are now routinely included in genitourinary system imaging, with applications in the female

pelvis, imaging of uterus and ovary, as well as prostate, bladder, penis, testis and kidney [102]. DW acquisitions routinely come with scanner-computed ADC maps; these aid the visual interpretation of the expert radiologist beyond anatomical sequences, and are used, in some cases, to calculate cut-off values that can aid the differentiation of different types of cancers (e.g., leiomyomas from uterine sarcomas [102]). Useful ADC cut-offs have also been proposed to distinguish metastatic vs non-metastatic lymph nodes in breast cancer with high reliability [103], while the detection of early ADC increases following chemo-/radio-therapy in oesophageal cancer were predictive of response [104]. In prostate imaging, DW imaging and ADC maps are now routinely included as part of the Prostate Imaging Reporting and Data System (PI-RADS) [105], a structured mpMRI report used in the treatment-naive prostate to study potentially malignant lesions. ADC has been found to be moderately correlated with cancer grade as assessed by the Gleason score [106], although at present there are still no, widely-accepted ADC cut-offs that can be used to classify prostate lesions as malignant [107]. Such associations with Gleason score are in line with related findings on cancer cellularity: ADC has been widely reported to correlate with tumour cellularity [108]. However, while characteristics beyond cell density should be taken into account when interpreting ADC changes [109], since ADC has been reported to correlate to a variety of histological properties, such as tumour-stroma ration, cell count, proliferation indices from Ki-67 immunostains, or number of tumor-infiltrating lymphocytes in several types of cancer of the liver [110]. From the more practical point of view of the MRI acquisition, efforts are also ongoing in terms of standardisation of protocols for ADC calculation: guidelines in term of b-value choice, for example, are provided as part of structured reports such as PI-RADS [105] for the prostate or Oncologically Relevant Findings Reporting and Data System (ONCO-RADS) for whole-body imaging [111]. Consensus guidelines have also been published, as for renal and breast DW-MRI [112, 113].

4.3 Advanced DW-MRI

Given the limitations of standard ADC mapping discussed above, current efforts of the DW-MRI community focus on developing novel techniques capable of providing metrics that are not only sensitive, but also highly specific to tissue features relevant in cancer. For this purpose, different biophysical signal models and/or phenomenological signal representations have been developed in a variety of body imaging contexts (see Fig. 4 as well as Appendix A for some basics principles of DW-MRI physics and signal modelling). These are typically based on analytical expressions that parametrise the signal as a function of the diffusion-encoding gradient timing and amplitude, as well as of tissue parameters of interest. DW-MRI then attempts to solve an inverse problem, i.e., to infer the unknown tissue parameters in each voxel from sets of signals measured at varying diffusion encodings. To solve this task, several different estimation techniques are used, such as non-linear least squares fitting. However, the solution of this inverse problem is generally ill-posed: different combinations of tissue parameters can explain the DW measurements equally well. This issue is exacerbated by scarce acquisition protocols, which lead to degeneracy (measurement sets effectively lack specificity towards all microstructure parameters [114, 115]). To cope with this problem, the go-to solution has been to fix some tissue parameters to pre-determined values. While this

may increase estimation robustness, it also leads to biases when the microstructure does not conform to modelling assumptions. The bias is unlikely to prevent a correlation between model parameters and a wide range of microstructures. However, subtle, pathological changes may produce a response in the constrained parameters that does not reflect the actual microstructural alteration. Ultimately, this can lead to inflated believes in the validity of constrained models. Recently, DNNs are becoming increasingly popular to solve this inverse problem [59, 62, 116]. Nonetheless, even with AI it is not possible to retrieve the microstructural information that is not encoded in the signal [117]. This implies that DW-MRI parametric maps obtained through DNNs should always be interpreted with care: unless specific strategies to map prediction uncertainty are implemented, DNNs always produce confidently an output, which could then exhibit *hallucinated* features in presence of unexpected inputs, as these will be mapped to the closest examples seen during the training stage.

4.4 MRI-histology agreement

Histological validation is imperative to demonstrate the sensitivity and biological specificity of any new DW-MRI metric. To this end, the voxel-by-voxel comparison of spatially-matched MRI and histology is ideal. However, obtaining this type of data *in vivo* is challenging, as it would require access to entire slabs of excised tissue, for example following surgery [118]. Alternatively, tissue can also be imaged *ex vivo*, following excision. Nonetheless, in this case it would lack perfusion, and in both cases, microstructural changes occur as a consequence of fixation. Importantly, DW-MRI maps are typically compared to tiny 2D sections of histological material (MRI slice thickness $\sim$ 0.5-2.5 mm; histology sectioning of $\sim$ 4-20 μm). As a consequence, portions of tissues that contributed to the MRI signal are not included in histological analyses. This may explain, at least in part, why within-sample MRI variations are not always mirrored by histology, despite overall strong MRI-histology between-sample agreement.

Another challenge is the fact that distributions of microstructural domains exist within a voxel. As a consequence, some MRI metrics may depend on the image resolution [119] (the lower the resolution, the more heterogeneous the voxel content). Also, this means that non-trivial histological features can be encoded in the DW signal. For example, DW-MRI cell size estimates are biased towards the largest cells, as these feature stronger time-dependence, contain more water than smaller cells, and since the smallest cells may not even be distinguishable (4-8 μm is the intrinsic cell size resolution limit with clinical systems [120]). For this reason, comparing DW-MRI cell size maps to the arithmetic mean of histology cell sizes l (i.e., $< l >$) may provide lower agreements than comparisons to other statistics emphasising the largest cells, e.g., $\left(\frac{<l^7>}{<l^3>}\right)^{\frac{1}{4}}$ [15].

Nevertheless, all in all the articles in this review suggest that measuring key cancer properties throughout the body in clinical setting may be feasible, i.e., vascularisation through IVIM-like approaches, and cell size/cellularity with VERDICT, IMPULSED, MDD, and more. The analysed methods, while not always accurate, retain sensitivity to key microstructural properties, and may provide non-invasive readouts useful in oncology.

4.5 Challenges

Despite the potential of the reviewed methods, challenges remain.

Firstly, the variety of acquisition protocols encompassed in the review highlights the lack of standardisation of advanced DW-MRI. While a truly quantitative MRI method should provide metrics that are invariant to the acquisition protocol, in practice the number of microstructural parameters that can be estimated depends on the measurements available. As a consequence, harmonisation (either prospective, or retrospective [121]) may be required before the new biomarkers can be considered truly quantitative. In this respect, we point out that certain inter-scanner differences are intimately related to the specifics of the acquisition, and are not only expected, but they actually encode microstructural information. For example, the overall ADC is approximately equal to the average of the ADCs of the different intra-voxel compartments, weighted by a TE-dependent fraction, i.e., $ADC(TE) \approx \sum_i f_i(TE)\ ADC_i$. Therefore, two ADCs obtained at two very different TE may also be very different between each other, due to inherently different T2-weighting. Harmonising these types of differences requires extra care, as it could blur information about disease processes.

Another challenge is related to scan times being longer than what is feasible in hospital settings. DW-MRI is only one of the several contrasts that are probed during an imaging session, where each contrasts typically takes no more than 10 minutes. Future work is required to make the latest DW techniques feasible with ultra-short acquisitions, potentially exploiting AI.

Furthermore, the review has highlighted that DW-MRI suffers from high levels of variability [116], implying that some of the approaches presented in this paper may not work well on a patient-by-patient basis. Methodological development to improve the intrinsic quality of images should therefore go hand-by-hand with signal model development [122], and should focus on: image quality enhancement via AI or machine learning; development of novel signal readouts that increase the robustness to motion; hardware improvements (e.g., stronger field/gradient strengths), to make acquisitions faster and increase SNR.

Finally, we stress that it is not yet known how the minimum, clinically-feasible DW protocol that enables resolving the microstructure exactly looks like. Research is still ongoing to understand which microstructural features can be encoded in the signal. The newest diffusion encodings, coupled with the latest estimation techniques, ever-faster acquisitions and protocol optimisation may soon increase the fidelity of DW MRI with respect to histopathology, and help us find answers to key questions such as: *How can we improve the validity of our DW-MRI models? How can we ensure generalisability across protocols and model types? Are there specific applications where one model is more suitable than another?*, as this could pave the way to personalised medicine in oncology.

4.6 Limitations

We acknowledge two main limitations in the compilation of this review.

The search was restricted using several tailored inclusion criteria. While this ensured a reproducible and complete compilation, it may have caused some articles to be left out of the selection for various reasons. For example,

some methods may have only been tested in the brain (e.g., Pulsed and Oscillating Gradient MRI for Assessment of Cell Size and Extracellular Space (POMACE) [123]); others may have lacked comparisons with histology [124]; and finally, some might have been missed due to variations in nomenclature, e.g., a study by Ianus et al. [125] on mesorectal lymph nodes.

Lastly, we classified techniques as phenomenological or biophysical (see Figure 3) to provide a general overview of the DW-MRI landscape. However, we acknowledge that some techniques may in fact fit both categories, e.g., "*partial volume*" methods such as RSI or HM-MRI, here classified as biophysical.

5 Conclusions

Several DW-MRI techniques, including DKI, IVIM, VERDICT, IMPULSED, MDD, HM-MRI and other have the potential to enable the non-invasive estimation of distinctive microstructural properties of cancer in the body, such as its vascularisation or cellularity. These techniques provide histologically meaningful indices which, while not necessarily accurate, may still equip oncologists with useful non-invasive biomarkers. However, further research is needed before these innovative approaches can fully enter the clinic. Efforts are needed to harmonise acquisition and analysis, to strengthen inter-/intra-scanner robustnesses, and to demonstrate histopathological validity in broader contexts.

Conflict of Interest

MN holds stocks in Random Walk Imaging AB, which has financial interests connected to advanced diffusion encoding protocols.

Acknowledgements

FG receives the support of a fellowship from "la Caixa" Foundation (ID 100010434). The fellowship code is LCF/BQ/PR22/11920010. RPL is supported by "la Caixa" Foundation, a CRIS Foundation Talent Award (TALENT19-05), the FERO Foundation, the Instituto de Salud Carlos III-Investigacion en Salud (PI18/01395 and PI21/01019), the Prostate Cancer Foundation (18YOUN19) and the Asociación Española Contra el Cancer (AECC) (PRYCO211023SERR). AI is supported by "la Caixa" Foundation (ID 100010434) and European Union's Horizon 2020 Research and Innovation Program (Marie Skłodowska-Curie grant No. 847648), fellowship code CF/BQ/PI20/11760029. CMWT was supported by a Veni grant (17331) from the Dutch Research Council (NWO) and a Sir Henry Wellcome Fellowship (215944/Z/19/Z). MN is supported by the Swedish Research Council (2020-04549), the Cancer Foundation (2022/2414), and ALF. This research was funded in whole, or in part, by the Wellcome Trust [Grant number 215944/Z/19/Z]. For the purpose of open access, the author has applied a CC BY public copyright licence to any Author Accepted Manuscript version arising from this submission.

References

[1] Reynaud O. Time-dependent diffusion MRI in cancer: Tissue modeling and applications. Frontiers in Physics. 2017 11;5(NOV):58.

[2] Dyrby TB, Innocenti GM, Bech M, Lundell H. Validation strategies for the interpretation of microstructure imaging using diffusion MRI. NeuroImage. 2018 11;182:62–79.

[3] Stejskal EO, Tanner JE. Spin Diffusion Measurements: Spin Echoes in the Presence of a Time-Dependent Field Gradient. The Journal of Chemical Physics. 1965 7;42(1):288. Available from: https://aip.scitation.org/doi/abs/10.1063/1.1695690.

[4] Westin CF, Knutsson H, Pasternak O, Szczepankiewicz F, Özarslan E, van Westen D, et al. Q-space trajectory imaging for multidimensional diffusion MRI of the human brain. NeuroImage. 2016 7;135:345–362.

[5] Martinez-Heras E, Grussu F, Prados F, Solana E, Llufriu S. Diffusion-Weighted Imaging: Recent Advances and Applications. Seminars in Ultrasound, CT and MRI. 2021 10;42(5):490–506.

[6] Rokem A, Yeatman JD, Pestilli F, Kay KN, Mezer A, Van Der Walt S, et al. Evaluating the Accuracy of Diffusion MRI Models in White Matter. PLOS ONE. 2015 4;10(4):e0123272. Available from: https://journals.plos.org/plosone/article?id=10.1371/journal.pone.0123272.

[7] Minati L, Weglarz WP. Physical foundations, models, and methods of diffusion magnetic resonance imaging of the brain: A review. Concepts in Magnetic Resonance Part A. 2007 9;30A(5):278–307. Available from: https://onlinelibrary.wiley.com/doi/full/10.1002/cmr.a.20094https://onlinelibrary.wiley.com/doi/abs/10.1002/cmr.a.20094https://onlinelibrary.wiley.com/doi/10.1002/cmr.a.20094.

[8] Jelescu IO, Budde MD. Design and validation of diffusion MRI models of white matter. Frontiers in Physics. 2017 11;5(NOV):61.

[9] Tang L, Zhou XJ. Diffusion MRI of cancer: From low to high b-values. John Wiley and Sons Inc.; 2019.

[10] Brancato V, Cavaliere C, Salvatore M, Monti S. Non-Gaussian models of diffusion weighted imaging for detection and characterization of prostate cancer: a systematic review and meta-analysis. Scientific Reports 2019 9:1. 2019 11;9(1):1–15. Available from: https://www.nature.com/articles/s41598-019-53350-8.

[11] Chatterjee A, Harmath C, Oto A. New prostate MRI techniques and sequences. Abdominal Radiology. 2020 12;45(12):4052–4062. Available from: https://link.springer.com/article/10.1007/s00261-020-02504-8.

[12] Tricco AC, Lillie E, Zarin W, O'Brien KK, Colquhoun H, Levac D, et al. PRISMA extension for scoping reviews (PRISMA-ScR): Checklist and explanation. Annals of Internal Medicine. 2018 10;169(7):467–473. Available from: https://www.acpjournals.org/doi/10.7326/M18-0850.

[13] Deen SS, Priest AN, McLean MA, Gill AB, Brodie C, Crawford R, et al. Diffusion kurtosis MRI as a predictive biomarker of response to neoadjuvant chemotherapy in high grade serous ovarian cancer. Scientific reports. 2019 12;9(1). Available from: https://pubmed.ncbi.nlm.nih.gov/31341212/.

[14] Rosenkrantz AB, Sigmund EE, Winnick A, Niver BE, Spieler B, Morgan GR, et al. Assessment of hepatocellular carcinoma using apparent diffusion coefficient and diffusion kurtosis indices: preliminary experience in fresh liver explants. Magnetic resonance imaging. 2012 12;30(10):1534–1540. Available from: https://pubmed.ncbi.nlm.nih.gov/22819175/.

[15] Grussu F, Bernatowicz K, Casanova-Salas I, Castro N, Nuciforo P, Mateo J, et al. Diffusion MRI signal cumulants and hepatocyte microstructure at fixed diffusion time: Insights from simulations, 9.4T imaging, and histology. Magnetic Resonance in Medicine. 2022 7;88(1):365–379. Available from: https://onlinelibrary.wiley.com/doi/full/10.1002/mrm.29174https://onlinelibrary.wiley.com/doi/abs/10.1002/mrm.29174https://onlinelibrary.wiley.com/doi/10.1002/mrm.29174.

[16] Wu G, Zhao Z, Yao Q, Kong W, Xu J, Zhang J, et al. The Study of Clear Cell Renal Cell Carcinoma with MR Diffusion Kurtosis Tensor Imaging and Its Histopathologic Correlation. Academic radiology. 2018 4;25(4):430–438. Available from: https://pubmed.ncbi.nlm.nih.gov/29198944/.

[17] Hectors SJ, Semaan S, Song C, Lewis S, Haines GK, Tewari A, et al. Advanced Diffusion-weighted Imaging Modeling for Prostate Cancer Characterization: Correlation with Quantitative Histopathologic Tumor Tissue Composition-A Hypothesis-generating Study. Radiology. 2018 3;286(3):918–928. Available from: https://pubmed.ncbi.nlm.nih.gov/29117481/.

[18] Guo J, Dong C, Wu Z, Sun W, Li X, Zhou R, et al. Diffusion kurtosis imaging assessment of the response to radiotherapy in a VX2 bone tumor model: an animal study. Acta radiologica (Stockholm, Sweden : 1987). 2022 2;63(2):182–191. Available from: https://pubmed.ncbi.nlm.nih.gov/33535770/.

[19] Tang Wj, Yao W, Jin Z, Kong Qc, Hu Wk, Liang Ys, et al. Evaluation of the Effects of Anti-PD-1 Therapy on Triple-Negative Breast Cancer in Mice by Diffusion Kurtosis Imaging and Dynamic Contrast-Enhanced Imaging. Journal of Magnetic Resonance Imaging. 2022;56(6):1912–1923.

[20] Xiao Z, Tang Z, Zhang J, Yang G, Zeng W, Luo J, et al. Whole-tumor histogram analysis of monoexponential and advanced diffusion-weighted imaging for sinonasal malignant tumors: Correlations with histopathologic features. Journal of Magnetic Resonance Imaging. 2020 1;51(1):273–285.

[21] Mori N, Inoue C, Tamura H, Nagasaka T, Ren H, Sato S, et al. Apparent diffusion coefficient and intravoxel incoherent motion-diffusion kurtosis model parameters in invasive breast cancer: Correlation with the histological parameters of whole-slide imaging. Magnetic resonance imaging. 2022 7;90:53–60. Available from: https://pubmed.ncbi.nlm.nih.gov/35439547/.

[22] Xiong Z, Geng Z, Lian S, Yin S, Xu G, Zhang Y, et al. Discriminating rectal cancer grades using restriction spectrum imaging. Abdominal radiology (New York). 2022 6;47(6):2014–2022. Available from: https://pubmed.ncbi.nlm.nih.gov/35368206/.

[23] Kiselev VG. The Cumulant Expansion: An Overarching Mathematical Framework For Understanding Diffusion NMR. In: Diffusion MRI. Oxford University Press; 2010. p. 152–168.

[24] Jensen JH, Helpern JA, Ramani A, Lu H, Kaczynski K. Diffusional kurtosis imaging: The quantification of non-gaussian water diffusion by means of magnetic resonance imaging. Magnetic Resonance in Medicine. 2005 6;53(6):1432–1440. Available from: https://onlinelibrary.wiley.com/doi/full/10.1002/mrm.20508https://onlinelibrary.wiley.com/doi/abs/10.1002/mrm.20508https://onlinelibrary.wiley.com/doi/10.1002/mrm.20508.

[25] Szczepankiewicz F, van Westen D, Englund E, Westin CF, Ståhlberg F, Lätt J, et al. The link between diffusion MRI and tumor heterogeneity: Mapping cell eccentricity and density by diffusional variance decomposition (DIVIDE). Neuroimage. 2016;142:522–532.

[26] Fang S, Yang Y, Chen B, Yin Z, Liu Y, Tao J, et al. DWI and IVIM Imaging in a Murine Model of Rhabdomyosarcoma: Correlations with Quantitative Histopathologic Features. Journal of Magnetic Resonance Imaging. 2022 1;55(1):225–233. Available from: https://onlinelibrary.wiley.com/doi/full/10.1002/jmri.27828https://onlinelibrary.wiley.com/doi/abs/10.1002/jmri.27828https://onlinelibrary.wiley.com/doi/10.1002/jmri.27828.

[27] Yuan Q, Kapur P, Zhang Y, Xi Y, Carvo I, Signoretti S, et al. Intratumor Heterogeneity of Perfusion and Diffusion in Clear-Cell Renal Cell Carcinoma: Correlation With Tumor Cellularity. Clinical genitourinary cancer. 2016 12;14(6):e585–e594. Available from: https://pubmed.ncbi.nlm.nih.gov/27209349/.

[28] Yin Y, Sedlaczek O, Müller B, Warth A, González-Vallinas M, Lahrmann B, et al. Tumor Cell Load and Heterogeneity Estimation From Diffusion-Weighted MRI Calibrated With Histological Data: an Example From Lung Cancer. IEEE transactions on medical imaging. 2018 1;37(1):35–46. Available from: https://pubmed.ncbi.nlm.nih.gov/28463188/.

[29] Meyer HJ, Höhn AK, Woidacki K, Andric M, Powerski M, Pech M, et al. Associations between IVIM histogram parameters and histopathology in rectal cancer. Magnetic resonance imaging. 2021 4;77:21–27. Available from: https://pubmed.ncbi.nlm.nih.gov/33316358/.

[30] Hecht EM, Liu MZ, Prince MR, Jambawalikar S, Remotti HE, Weisberg SW, et al. Can diffusion-weighted imaging serve as a biomarker of fibrosis in pancreatic adenocarcinoma? Journal of magnetic resonance imaging : JMRI. 2017 8;46(2):393–402. Available from: https://pubmed.ncbi.nlm.nih.gov/28152252/.

[31] Winfield JM, Miah AB, Strauss D, Thway K, Collins DJ, DeSouza NM, et al. Utility of Multi-Parametric Quantitative Magnetic Resonance Imaging for Characterization and Radiotherapy Response Assessment in Soft-Tissue Sarcomas and Correlation With Histopathology. Frontiers in oncology. 2019;9(APR). Available from: https://pubmed.ncbi.nlm.nih.gov/31106141/.

[32] Cai SQ, Li Y, Li YA, Wang L, Zhu J, Zhao SH, et al. Perfusion-based functional magnetic resonance imaging for differentiating serous borderline ovarian tumors from early serous ovarian cancers in a rat model. Acta radiologica (Stockholm, Sweden : 1987). 2021 1;62(1):129–138. Available from: https://pubmed.ncbi.nlm.nih.gov/32276553/.

[33] Wu H, Liu H, Liang C, Zhang S, Liu Z, Liu C, et al. Diffusion-weighted multiparametric MRI for monitoring longitudinal changes of parameters in rabbit VX2 liver tumors. Journal of magnetic resonance imaging : JMRI. 2016 9;44(3):707–714. Available from: https://pubmed.ncbi.nlm.nih.gov/26878263/.

[34] Liu Q, Zhang J, Jiang M, Zhang Y, Chen T, Zhang J, et al. Evaluating the Histopathology of Pancreatic Ductal Adenocarcinoma by Intravoxel Incoherent Motion-Diffusion Weighted Imaging Comparing With Diffusion-Weighted Imaging. Frontiers in oncology. 2021 6;11. Available from: https://pubmed.ncbi.nlm.nih.gov/34249707/.

[35] Song XL, Kang HK, Jeong GW, Ahn KY, Jeong YY, Kang YJ, et al. Intravoxel incoherent motion diffusion-weighted imaging for monitoring chemotherapeutic efficacy in gastric cancer. World Journal of Gastroenterology. 2016 6;22(24):5520. Available from: /pmc/articles/PMC4917612//pmc/articles/PMC4917612/?report=abstracthttps://www.ncbi.nlm.nih.gov/pmc/articles/PMC4917612/.

[36] Lee HJ, Rha SY, Chung YE, Shim HS, Kim YJ, Hur J, et al. Tumor perfusion-related parameter of diffusion-weighted magnetic resonance imaging: correlation with histological microvessel density. Magnetic resonance in medicine. 2014;71(4):1554–1558. Available from: https://pubmed.ncbi.nlm.nih.gov/23798038/.

[37] Mayer P, Fritz F, Koell M, Skornitzke S, Bergmann F, Gaida MM, et al. Assessment of tissue perfusion of pancreatic cancer as potential imaging biomarker by means of Intravoxel incoherent motion MRI and CT perfusion: correlation with histological microvessel density as ground truth. Cancer imaging : the official publication of the International Cancer Imaging Society. 2021 12;21(1). Available from: https://pubmed.ncbi.nlm.nih.gov/33468259/.

[38] Li JL, Ye WT, Liu ZY, Yan LF, Luo W, Cao XM, et al. Comparison of microvascular perfusion evaluation among IVIM-DWI, CT perfusion imaging and histological microvessel density in rabbit liver VX2 tumors.

Magnetic resonance imaging. 2018 2;46:64–69. Available from: https://pubmed.ncbi.nlm.nih.gov/29103979/.

[39] Yang SH, Lin J, Lu F, Han ZH, Fu CX, Lv P, et al. Evaluation of antiangiogenic and antiproliferative effects of sorafenib by sequential histology and intravoxel incoherent motion diffusion-weighted imaging in an orthotopic hepatocellular carcinoma xenograft model. Journal of magnetic resonance imaging : JMRI. 2017 1;45(1):270–280. Available from: https://pubmed.ncbi.nlm.nih.gov/27299302/.

[40] Hompland T, Hole KHk, Ragnum HB, Aarnes EK, Vlatkovic L, Kathrine Lie A, et al. Combined MR Imaging of Oxygen Consumption and Supply Reveals Tumor Hypoxia and Aggressiveness in Prostate Cancer Patients. Cancer research. 2018 8;78(16):4774–4785. Available from: https://pubmed.ncbi.nlm.nih.gov/29945958/.

[41] Tao J, Yin Z, Li X, Zhang Y, Zhang K, Yang Y, et al. Correlation between IVIM parameters and microvessel architecture: direct comparison of MRI images and pathological slices in an orthotopic murine model of rhabdomyosarcoma. European Radiology. 2023;p. 1–9.

[42] Zhang Z, Shen S, Ma J, Qi T, Gao C, Hu X, et al. Sequential multi-parametric MRI in assessment of the histological subtype and features in the malignant pleural mesothelioma xenografts. Heliyon. 2023;9(4).

[43] Xie S, Qiu C, Sun Y, Yu Y, Zhang Q, Bao M, et al. Series of Intravoxel Incoherent Motion and T2* Magnetic Resonance Imaging Mapping in Detection of Liver Perfusion Changes and Regeneration Among Partial Hepatectomy in Sprague-Dawley Rats. Academic Radiology. 2022;29(12):1810–1818.

[44] Le Bihan D, Breton E, Lallemand D, Grenier P, Cabanis E, Laval-Jeantet M. MR imaging of intravoxel incoherent motions: application to diffusion and perfusion in neurologic disorders. Radiology. 1986;161(2):401–407. Available from: https://pubmed.ncbi.nlm.nih.gov/3763909/.

[45] Jerome NP, D'Arcy JA, Feiweier T, Koh DM, Leach MO, Collins DJ, et al. Extended T2-IVIM model for correction of TE dependence of pseudo-diffusion volume fraction in clinical diffusion-weighted magnetic resonance imaging. Physics in medicine and biology. 2016 11;61(24):N667–N680. Available from: https://pubmed.ncbi.nlm.nih.gov/27893459/.

[46] Liu Y, Wang X, Cui Y, Jiang Y, Yu L, Liu M, et al. Comparative Study of Monoexponential, Intravoxel Incoherent Motion, Kurtosis, and IVIM-Kurtosis Models for the Diagnosis and Aggressiveness Assessment of Prostate Cancer. Frontiers in Oncology. 2020 9;10:1763. Available from: /pmc/articles/PMC7518290//pmc/articles/PMC7518290/?report=abstracthttps://www.ncbi.nlm.nih.gov/pmc/articles/PMC7518290/.

[47] Barbieri S, Donati OF, Froehlich JM, Thoeny HC. Impact of the calculation algorithm on biexponential fitting

of diffusion-weighted MRI in upper abdominal organs. Magnetic Resonance in Medicine. 2016;75(5):2175–2184.

[48] Lasič S, Nilsson M, Lätt J, Ståhlberg F, Topgaard D. Apparent exchange rate mapping with diffusion MRI. Magnetic Resonance in Medicine. 2011 8;66(2):356–365.

[49] Wetscherek A, Stieltjes B, Laun FB. Flow-compensated intravoxel incoherent motion diffusion imaging. Magnetic resonance in medicine. 2015 8;74(2):410–419. Available from: https://pubmed.ncbi.nlm.nih.gov/25116325/.

[50] Ahlgren A, Knutsson L, Wirestam R, Nilsson M, Ståhlberg F, Topgaard D, et al. Quantification of microcirculatory parameters by joint analysis of flow-compensated and non-flow-compensated intravoxel incoherent motion (IVIM) data. NMR in Biomedicine. 2016;29(5):640–649.

[51] Sijtsema ND, Petit SF, Poot DH, Verduijn GM, van der Lugt A, Hoogeman MS, et al. An optimal acquisition and post-processing pipeline for hybrid IVIM-DKI in head and neck. Magnetic Resonance in Medicine. 2021;85(2):777–789.

[52] Bonet-Carne E, Johnston E, Daducci A, Jacobs JG, Freeman A, Atkinson D, et al. VERDICT-AMICO: Ultrafast fitting algorithm for non-invasive prostate microstructure characterization. NMR in biomedicine. 2019 1;32(1). Available from: https://pubmed.ncbi.nlm.nih.gov/30378195/.

[53] Bailey C, Bourne RM, Siow B, Johnston EW, Brizmohun Appayya M, Pye H, et al. VERDICT MRI validation in fresh and fixed prostate specimens using patient-specific moulds for histological and MR alignment. NMR in biomedicine. 2019 5;32(5). Available from: https://pubmed.ncbi.nlm.nih.gov/30779863/.

[54] Duchêne G, Abarca-Quinones J, Leclercq I, Duprez T, Peeters F. Insights into tissue microstructure using a double diffusion encoding sequence on a clinical scanner: Validation and application to experimental tumor models. Magnetic resonance in medicine. 2020 4;83(4):1263–1276. Available from: https://pubmed.ncbi.nlm.nih.gov/31593350/.

[55] Panagiotaki E, Walker-Samuel S, Siow B, Johnson SP, Rajkumar V, Pedley RB, et al. Noninvasive quantification of solid tumor microstructure using VERDICT MRI. Cancer Research. 2014;74(7):1902–1912.

[56] Johnston EW, Bonet-Carne E, Ferizi U, Yvernault B, Pye H, Patel D, et al. VERDICT MRI for prostate cancer: Intracellular volume fraction versus apparent diffusion coefficient. Radiology. 2019 5;291(2):391–397. Available from: https://doi.org/10.1148/radiol.2019181749.

[57] Bailey C, Collins DJ, Tunariu N, Orton MR, Morgan VA, Feiweier T, et al. Microstructure Characterization of Bone Metastases from Prostate Cancer with Diffusion MRI: Preliminary Findings. Frontiers in oncology. 2018 2;8(FEB). Available from: https://pubmed.ncbi.nlm.nih.gov/29503808/.

[58] Johnston E, Pye H, Bonet-Carne E, Panagiotaki E, Patel D, Galazi M, et al. INNOVATE: A prospective cohort study combining serum and urinary biomarkers with novel diffusion-weighted magnetic resonance imaging for the prediction and characterization of prostate cancer. BMC Cancer. 2016 10;16(1). Available from: /pmc/articles/PMC5073433//pmc/articles/PMC5073433/?report=abstracthttps://www.ncbi.nlm.nih.gov/pmc/articles/PMC5073433/.

[59] Palombo M, Valindria V, Singh S, Chiou E, Giganti F, Pye H, et al. Joint estimation of relaxation and diffusion tissue parameters for prostate cancer with relaxation-VERDICT MRI. Scientific Reports 2023 13:1. 2023 2;13(1):1–13. Available from: https://www.nature.com/articles/s41598-023-30182-1.

[60] Panagiotaki E, Chan RW, Dikaios N, Ahmed HU, O'Callaghan J, Freeman A, et al. Microstructural characterization of normal and malignant human prostate tissue with vascular, extracellular, and restricted diffusion for cytometry in tumours magnetic resonance imaging. Investigative radiology. 2015 4;50(4):218–227. Available from: https://pubmed.ncbi.nlm.nih.gov/25426656/.

[61] Panagiotaki E, Schneider T, Siow B, Hall MG, Lythgoe MF, Alexander DC. Compartment models of the diffusion MR signal in brain white matter: A taxonomy and comparison. NeuroImage. 2012 2;59(3):2241–2254.

[62] Chiou E, Valindria V, Giganti F, Punwani S, Kokkinos I, Panagiotaki E. Synthesizing VERDICT Maps from Standard DWI Data Using GANs. Lecture Notes in Computer Science (including subseries Lecture Notes in Artificial Intelligence and Lecture Notes in Bioinformatics). 2021;13006 LNCS:58–67. Available from: https://link.springer.com/chapter/10.1007/978-3-030-87615-9_6.

[63] Jiang X, Xu J, Gore JC. Mapping hepatocyte size in vivo using temporal diffusion spectroscopy MRI. Magnetic Resonance in Medicine. 2020 4;84(5):2671–2683. Available from: https://europepmc.org/articles/PMC7402009https://europepmc.org/article/MED/32333469.

[64] Xu J, Jiang X, Li H, Arlinghaus LR, McKinley ET, Devan SP, et al. Magnetic resonance imaging of mean cell size in human breast tumors. Magnetic Resonance in Medicine. 2019;.

[65] Jiang X, Dudzinski S, Beckermann KE, Young K, McKinley E, J McIntyre O, et al. MRI of tumor T cell infiltration in response to checkpoint inhibitor therapy. Journal for immunotherapy of cancer. 2020 6;8(1). Available from: https://pubmed.ncbi.nlm.nih.gov/32581044/.

[66] Jiang X, Li H, Xie J, McKinley ET, Zhao P, Gore JC, et al. In vivo imaging of cancer cell size and cellularity using temporal diffusion spectroscopy. Magnetic resonance in medicine. 2017 7;78(1):156–164. Available from: https://pubmed.ncbi.nlm.nih.gov/27495144/.

[67] Li H, Jiang X, Xie J, Gore JC, Xu J. Impact of transcytolemmal water exchange on estimates of tissue microstructural properties derived from diffusion MRI. Magnetic resonance in medicine. 2017

6;77(6):2239. Available from: /pmc/articles/PMC5183568//pmc/articles/PMC5183568/?report=abstracthttps://www.ncbi.nlm.nih.gov/pmc/articles/PMC5183568/.

[68] Wu D, Jiang K, Li H, Zhang Z, Ba R, Zhang Y, et al. Time-Dependent Diffusion MRI for Quantitative Microstructural Mapping of Prostate Cancer. Radiology. 2022 6;303(3):578–587. Available from: https://pubs.rsna.org/doi/10.1148/radiol.211180.

[69] Jiang X, Devan SP, Xie J, Gore JC, Xu J. Improving MR cell size imaging by inclusion of transcytolemmal water exchange. NMR in biomedicine. 2022;Available from: https://pubmed.ncbi.nlm.nih.gov/35794795/.

[70] Bennett KM, Schmainda KM, Bennett R, Rowe DB, Lu H, Hyde JS. Characterization of continuously distributed cortical water diffusion rates with a stretched-exponential model. Magnetic resonance in medicine. 2003 10;50(4):727–734. Available from: https://pubmed.ncbi.nlm.nih.gov/14523958/.

[71] Senn N, Masannat Y, Husain E, Siow B, Heys SD, He J. q-Space Imaging Yields a Higher Effect Gradient to Assess Cellularity than Conventional Diffusion-weighted Imaging Methods at 3.0 T: A Pilot Study with Freshly Excised Whole-Breast Tumors. Radiology Imaging cancer. 2019 9;1(1). Available from: https://pubmed.ncbi.nlm.nih.gov/33778671/.

[72] Novikov DS, Fieremans E, Jespersen SN, Kiselev VG. Quantifying brain microstructure with diffusion MRI: Theory and parameter estimation. NMR in Biomedicine. 2019 4;32(4):e3998. Available from: https://onlinelibrary.wiley.com/doi/full/10.1002/nbm.3998https://onlinelibrary.wiley.com/doi/abs/10.1002/nbm.3998https://analyticalsciencejournals.onlinelibrary.wiley.com/doi/10.1002/nbm.3998.

[73] Yamada I, Hikishima K, Miyasaka N, Tokairin Y, Ito E, Kawano T, et al. Esophageal carcinoma: Evaluation with q-space diffusion-weighted MR imaging ex vivo. Magnetic resonance in medicine. 2015 6;73(6):2262–2273. Available from: https://pubmed.ncbi.nlm.nih.gov/24947492/.

[74] Callaghan PT, Eccles CD, Xia Y. NMR microscopy of dynamic displacements: k-space and q-space imaging. Journal of Physics E: Scientific Instruments. 1988 8;21(8):820. Available from: https://iopscience.iop.org/article/10.1088/0022-3735/21/8/017https://iopscience.iop.org/article/10.1088/0022-3735/21/8/017/meta.

[75] Lätt J, Nilsson M, Malmborg C, Rosquist H, Wirestam R, Ståhlberg F, et al. Accuracy of q-space related parameters in MRI: simulations and phantom measurements. IEEE transactions on medical imaging. 2007 11;26(11):1437–1447. Available from: https://pubmed.ncbi.nlm.nih.gov/18041259/.

[76] Özarslan E, Koay CG, Shepherd TM, Komlosh ME, Irfanoğlu MO, Pierpaoli C, et al. Mean Apparent Propagator (MAP) MRI: a novel diffusion imaging method for mapping tissue microstructure. NeuroImage.

2013 9;78:16. Available from: /pmc/articles/PMC4059870//pmc/articles/PMC4059870/?report=abstracthttps://www.ncbi.nlm.nih.gov/pmc/articles/PMC4059870/.

[77] Wedeen VJ, Hagmann P, Tseng WYI, Reese TG, Weisskoff RM. Mapping complex tissue architecture with diffusion spectrum magnetic resonance imaging. Magnetic Resonance in Medicine. 2005 12;54(6):1377–1386. Available from: https://onlinelibrary.wiley.com/doi/full/10.1002/mrm.20642https://onlinelibrary.wiley.com/doi/abs/10.1002/mrm.20642https://onlinelibrary.wiley.com/doi/10.1002/mrm.20642.

[78] Xu J, Jiang X, Devan SP, Arlinghaus LR, McKinley ET, Xie J, et al. MRI-Cytometry: Mapping non-parametric cell size distributions using diffusion MRI. Magnetic resonance in medicine. 2021 2;85(2):748. Available from: /pmc/articles/PMC7722100//pmc/articles/PMC7722100/?report=abstracthttps://www.ncbi.nlm.nih.gov/pmc/articles/PMC7722100/.

[79] Yamin G, Schenker-Ahmed NM, Shabaik A, Adams D, Bartsch H, Kuperman J, et al. Voxel Level Radiologic-Pathologic Validation of Restriction Spectrum Imaging Cellularity Index with Gleason Grade in Prostate Cancer. Clinical cancer research : an official journal of the American Association for Cancer Research. 2016 6;22(11):2668–2674. Available from: https://pubmed.ncbi.nlm.nih.gov/27250935/.

[80] White NS, Leergaard TB, D'Arceuil H, Bjaalie JG, Dale AM. Probing tissue microstructure with restriction spectrum imaging: Histological and theoretical validation. Human brain mapping. 2013 2;34(2):327–346. Available from: https://pubmed.ncbi.nlm.nih.gov/23169482/.

[81] Morelli L, Palombo M, Buizza G, Riva G, Pella A, Fontana G, et al. Microstructural parameters from DW-MRI for tumour characterization and local recurrence prediction in particle therapy of skull-base chordoma. Medical Physics. 2023;.

[82] Nilsson M, Alerstam E, Wirestam R, Sta F, Brockstedt S, Lätt J, et al. Evaluating the accuracy and precision of a two-compartment Kärger model using Monte Carlo simulations. Journal of Magnetic Resonance. 2010;206(1):59–67.

[83] Topgaard D. Isotropic diffusion weighting in PGSE NMR: Numerical optimization of the q-MAS PGSE sequence. Microporous and Mesoporous Materials. 2013 9;178:60–63.

[84] Eriksson S, Lasic S, Topgaard D. Isotropic diffusion weighting in PGSE NMR by magic-angle spinning of the q-vector. Journal of Magnetic Resonance. 2013 1;226:13–18.

[85] Naranjo ID, Reymbaut A, Brynolfsson P, Gullo RL, Bryskhe K, Topgaard D, et al. Multidimensional diffusion magnetic resonance imaging for characterization of tissue microstructure in breast cancer patients: A prospective pilot study. Cancers. 2021 4;13(7).

[86] Nilsson M, Eklund G, Szczepankiewicz F, Skorpil M, Bryskhe K, Westin CF, et al. Mapping prostatic microscopic anisotropy using linear and spherical b-tensor encoding: A preliminary study. Magnetic Resonance in Medicine. 2021 10;86(4):2025–2033.

[87] Langbein BJ, Szczepankiewicz F, Westin CF, Bay C, Maier SE, Kibel AS, et al. A Pilot Study of Multidimensional Diffusion MRI for Assessment of Tissue Heterogeneity in Prostate Cancer. Investigative radiology. 2021 12;56(12):845–853.

[88] Topgaard D. Multidimensional diffusion MRI. Journal of Magnetic Resonance. 2017 2;275:98–113.

[89] Topgaard D. Diffusion tensor distribution imaging. NMR in Biomedicine. 2019;32(5):e4066.

[90] Szczepankiewicz F, Sjölund J, Ståhlberg F, Lätt J, Nilsson M. Tensor-valued diffusion encoding for diffusional variance decomposition (DIVIDE): Technical feasibility in clinical MRI systems. PloS one. 2019;14(3):e0214238.

[91] Chatterjee A, Mercado C, Bourne RM, Yousuf A, Hess B, Antic T, et al. Validation of Prostate Tissue Composition by Using Hybrid Multidimensional MRI: Correlation with Histologic Findings. Radiology. 2022 2;302(2):368–377. Available from: https://pubs.rsna.org/doi/10.1148/radiol.2021204459.

[92] Chatterjee A, Antic T, Gallan AJ, Paner GP, Lin LIK, Karczmar GS, et al. Histological validation of prostate tissue composition measurement using hybrid multi-dimensional MRI: agreement with pathologists' measures. Abdominal radiology (New York). 2022 2;47(2):801–813. Available from: https://pubmed.ncbi.nlm.nih.gov/34878579/.

[93] Chatterjee A, Bourne RM, Wang S, Devaraj A, Gallan AJ, Antic T, et al. Diagnosis of Prostate Cancer with Noninvasive Estimation of Prostate Tissue Composition by Using Hybrid Multidimensional MR Imaging: A Feasibility Study. Radiology. 2018 6;287(3):863–873. Available from: https://pubmed.ncbi.nlm.nih.gov/29393821/.

[94] Slator PJ, Palombo M, Miller KL, Westin CF, Laun F, Kim D, et al. Combined diffusion-relaxometry microstructure imaging: Current status and future prospects. Magnetic Resonance in Medicine. 2021 12;86(6):2987. Available from: /pmc/articles/PMC8568657//pmc/articles/PMC8568657/?report=abstracthttps://www.ncbi.nlm.nih.gov/pmc/articles/PMC8568657/.

[95] Lemberskiy G, Fieremans E, Veraart J, Deng FM, Rosenkrantz AB, Novikov DS. Characterization of prostate microstructure using water diffusion and NMR relaxation. Frontiers in Physics. 2018 9;6(SEP):91.

[96] Kim D, Doyle EK, Wisnowski JL, Kim JH, Haldar JP. Diffusion-Relaxation Correlation Spectroscopic Imaging (DR-CSI): A Multidimensional Approach for Probing Microstructure. Magnetic resonance in medicine. 2017 12;78(6):2236. Available from: /pmc/articles/PMC5605406//pmc/articles/PMC5605406/?report=abstracthttps://www.ncbi.nlm.nih.gov/pmc/articles/PMC5605406/.

[97] De Almeida Martins JP, Topgaard D. Multidimensional correlation of nuclear relaxation rates and diffusion tensors for model-free investigations of heterogeneous anisotropic porous materials. Scientific Reports 2018 8:1. 2018 2;8(1):1–12. Available from: https://www.nature.com/articles/s41598-018-19826-9.

[98] Hürlimann M, Venkataramanan L, Flaum C. The diffusion–spin relaxation time distribution function as an experimental probe to characterize fluid mixtures in porous media. The Journal of chemical physics. 2002;117(22):10223–10232.

[99] Zhang Z, Wu HH, Priester A, Magyar C, Mirak SA, Shakeri S, et al. Prostate Microstructure in Prostate Cancer Using 3-T MRI with Diffusion-Relaxation Correlation Spectrum Imaging: Validation with Whole-Mount Digital Histopathology. Radiology. 2020 8;296(2):348–355. Available from: https://pubmed.ncbi.nlm.nih.gov/32515678/.

[100] Dai Y, Hu W, Wu G, Wu D, Zhu M, Luo Y, et al. Grading Clear Cell Renal Cell Carcinoma Grade Using Diffusion Relaxation Correlated MR Spectroscopic Imaging. Journal of Magnetic Resonance Imaging. 2023;.

[101] Sun Y, Reynolds HM, Wraith D, Williams S, Finnegan ME, Mitchell C, et al. Voxel-wise prostate cell density prediction using multiparametric magnetic resonance imaging and machine learning. Acta Oncologica. 2018 12;57(11):1540–1546. Available from: https://www.tandfonline.com/action/journalInformation?journalCode=ionc20.

[102] De Perrot T, Sadjo Zoua C, Glessgen CG, Botsikas D, Berchtold L, Salomir R, et al. Diffusion-Weighted MRI in the Genitourinary System. Journal of clinical medicine. 2022;11(7):1921.

[103] De Cataldo C, Bruno F, Palumbo P, Di Sibio A, Arrigoni F, Clemente A, et al. Apparent diffusion coefficient magnetic resonance imaging (ADC-MRI) in the axillary breast cancer lymph node metastasis detection: A narrative review. Gland Surgery. 2020;9(6):2225.

[104] Vollenbrock SE, Voncken FE, Bartels LW, Beets-Tan RG, Bartels-Rutten A. Diffusion-weighted MRI with ADC mapping for response prediction and assessment of oesophageal cancer: a systematic review. Radiotherapy and Oncology. 2020;142:17–26.

[105] Turkbey B, Rosenkrantz AB, Haider MA, Padhani AR, Villeirs G, Macura KJ, et al. Prostate imaging reporting and data system version 2.1: 2019 update of prostate imaging reporting and data system version 2. European urology. 2019;76(3):340–351.

[106] Surov A, Meyer HJ, Wienke A. Correlations between apparent diffusion coefficient and gleason score in prostate cancer: a systematic review. European Urology Oncology. 2020;3(4):489–497.

[107] Manetta R, Palumbo P, Gianneramo C, Bruno F, Arrigoni F, Natella R, et al. Correlation between ADC values and Gleason score in evaluation of prostate cancer: multicentre experience and review of the literature. Gland surgery. 2019;8(Suppl 3):S216.

[108] Chen L, Liu M, Bao J, Xia Y, Zhang J, Zhang L, et al. The correlation between apparent diffusion coefficient and tumor cellularity in patients: a meta-analysis. PloS one. 2013;8(11):e79008.

[109] Brabec J, Friedjungová M, Vašata D, Englund E, Bengzon J, Knutsson L, et al. Meningioma microstructure assessed by diffusion MRI: An investigation of the source of mean diffusivity and fractional anisotropy by quantitative histology. NeuroImage: Clinical. 2023;37:103365.

[110] Surov A, Eger KI, Potratz J, Gottschling S, Wienke A, Jechorek D. Apparent diffusion coefficient correlates with different histopathological features in several intrahepatic tumors. European Radiology. 2023;p. 1–10.

[111] Petralia G, Koh DM, Attariwala R, Busch JJ, Eeles R, Karow D, et al. Oncologically relevant findings reporting and data system (ONCO-RADS): guidelines for the acquisition, interpretation, and reporting of whole-body MRI for cancer screening. Radiology. 2021;299(3):494–507.

[112] Ljimani A, Caroli A, Laustsen C, Francis S, Mendichovszky IA, Bane O, et al. Consensus-based technical recommendations for clinical translation of renal diffusion-weighted MRI. Magnetic Resonance Materials in Physics, Biology and Medicine. 2020;33:177–195.

[113] Baltzer P, Mann RM, Iima M, Sigmund EE, Clauser P, Gilbert FJ, et al. Diffusion-weighted imaging of the breast—a consensus and mission statement from the EUSOBI International Breast Diffusion-Weighted Imaging working group. European radiology. 2020;30:1436–1450.

[114] Jelescu IO, Veraart J, Fieremans E, Novikov DS. Degeneracy in model parameter estimation for multi-compartmental diffusion in neuronal tissue. NMR in Biomedicine. 2016 1;29(1):33–47.

[115] Lampinen B, Szczepankiewicz F, Lätt J, Knutsson L, Mårtensson J, Björkman-Burtscher IM, et al. Probing brain tissue microstructure with MRI: principles, challenges, and the role of multidimensional diffusion-relaxation encoding. NeuroImage. 2023;p. 120338.

[116] Barbieri S, Gurney-Champion OJ, Klaassen R, Thoeny HC. Deep learning how to fit an intravoxel incoherent motion model to diffusion-weighted MRI. Magnetic Resonance in Medicine. 2020 1;83(1):312–321. Available from: https://onlinelibrary.wiley.com/doi/full/10.1002/mrm.27910https://onlinelibrary.wiley.com/doi/abs/10.1002/mrm.27910https://onlinelibrary.wiley.com/doi/10.1002/mrm.27910.

[117] de Almeida Martins JP, Nilsson M, Lampinen B, Palombo M, While PT, Westin CF, et al. Neural networks for parameter estimation in microstructural MRI: Application to a diffusion-relaxation model of white matter. NeuroImage. 2021 12;244:118601.

[118] Bourne RM, Bailey C, Johnston EW, Pye H, Heavey S, Whitaker H, et al. Apparatus for histological validation of in vivo and ex vivo magnetic resonance imaging of the human prostate. Frontiers in Oncology. 2017 3;7(MAR):47.

[119] Szczepankiewicz F, Lasič S, van Westen D, Sundgren PC, Englund E, Westin CF, et al. Quantification of microscopic diffusion anisotropy disentangles effects of orientation dispersion from microstructure: applications in healthy volunteers and in brain tumors. NeuroImage. 2015 1;0:241. Available from: /pmc/articles/PMC4252798//pmc/articles/PMC4252798/?report=abstracthttps://www.ncbi.nlm.nih.gov/pmc/articles/PMC4252798/.

[120] Nilsson M, Lasič S, Drobnjak I, Topgaard D, Westin CF. Resolution limit of cylinder diameter estimation by diffusion MRI: The impact of gradient waveform and orientation dispersion. NMR in biomedicine. 2017 7;30(7). Available from: https://pubmed.ncbi.nlm.nih.gov/28318071/.

[121] Tax CM, Grussu F, Kaden E, Ning L, Rudrapatna U, John Evans C, et al. Cross-scanner and cross-protocol diffusion MRI data harmonisation: A benchmark database and evaluation of algorithms. NeuroImage. 2019 7;195:285–299.

[122] Tax CM, Bastiani M, Veraart J, Garyfallidis E, Irfanoglu MO. What's new and what's next in diffusion MRI preprocessing. NeuroImage. 2022;249:118830.

[123] Reynaud O, Winters KV, Hoang DM, Wadghiri YZ, Novikov DS, Kim SG. Pulsed and oscillating gradient MRI for assessment of cell size and extracellular space (POMACE) in mouse gliomas. NMR in Biomedicine. 2016 10;29(10):1350–1363.

[124] Xing S, Levesque IR. A simulation study of cell size and volume fraction mapping for tissue with two underlying cell populations using diffusion-weighted MRI. Magnetic resonance in medicine. 2021 8;86(2):1029–1044. Available from: https://pubmed.ncbi.nlm.nih.gov/33644889/.

[125] Ianuş A, Santiago I, Galzerano A, Montesinos P, Loução N, Sanchez-Gonzalez J, et al. Higher-order diffusion MRI characterization of mesorectal lymph nodes in rectal cancer. Magn Reson Med. 2019;00:1–17.

Table 1: Summary of the diffusion models and signal representations included.

Model/representation	**Reported by**	**Model parameters**	**Salient MR-acquisition protocol requirements**	**Main histological correlates assessed**
DKI	[13–19]	ADC_k, K	High b-values required to sample non-Gaussian diffusion	Cellularity
IVIM	[20, 21, 26–43]	D_t, D^*, f	Many b-values required, including low b-values to sample pseudo-diffusion	Cellularity, vessel density measures
VERDICT	[52–59]	f_{ic}, f_{EES}, f_{vasc}, d_{ic}, d_{ec}, d_{vasc} Cell size radius R	PGSE protocol probing various different TE, gradient duration and separations. Novel non-PGSE encodings recently explored	Cellularity, intra-cellular fraction, cell size
IMPULSED	[63–69]	f_{ic}, d_{ic}, d_{ec} Cell size radius R	Uses OGSE in addition to PGSE	Cellularity, intra-cellular fraction, cell size
SEM	[17, 33, 71]	D_{SEM}, α	PGSE protocol probing different low and intermediate b-values at fixed diffusion time	Cellularity, heterogeneity
QSI	[71, 73]	Statistics from displacement distribution profiles	PGSE protocol probing different q-values required, with high gradient strength required	Cellularity, nuclear-to-cytoplasm ratio
MRI-Cytometry	[78]	Probability distribution of cell size radius R, d_{ic}, d_{ec}, f_{ic}, extra-cellular DTD factor β	General framework, so can be applied for multiple acquisition protocols	Cell size
RSI	[22, 79]	Volume fractions C_n	PGSE with high b-values required, but relatively short scan time (it can be performed at fixed diffusion time)	Indices of intra-voxel tissue composition
MDD-MRI	[85]	Statistical descriptors of Diffusion Tensor Distributions	Uses a variety of anisotropic or isotropic b-tensor encodings; e.g., gradient waveforms implementing isotropic linear encoding along multiple directions as well as spherical tensor encoding	Indices of tissue composition
HM-MRI	[91, 92]	The volume fractions V_n, the $T2_n$, and the ADC_n-value for the lumen, stroma, and epithelium	Part of an mp-MRI protocol including T2-weighted, DCE, and diffusion imaging (PGSE at varying b-values and TE, with no requirements on diffusion time)	Indices of tissue composition
DR-CSI	[99, 100]	Volume fractions f_n	Part of an mp-MRI protocol including T2-weighted and diffusion imaging (PGSE at varying b-values and TE, with no requirements on diffusion time)	Indices of tissue composition
MC DW-MRI	[81]	Cell radius and vol. fraction R and f_{ic}, cell diffusivity d_{ic} and apparent cellularity ρ_{app}	Part of a clinical mp-MRI protocol including anatomical MRI and clinical DW-MRI for ADC mapping (no requirements on diffusion time)	Ki-67 expression
mpMRI-based AI	[101]	Cellularity	Part of an mp-MRI protocol including T2-weighted, DCE, and simple ADC mapping based on PGSE	Cellularity

Model abbreviations: DKI = Diffusion Kurtosis Imaging, IVIM = Intravoxel Incoherent Motion, VERDICT = Vascular, Extracellular, and Restricted Diffusion for Cytometry in Tumors, IMPULSED = Imaging Microstructural Parameters Using Limited Spectrally-Edited Diffusion, SEM = Stretched Exponential Model, QSI = q-space imaging, RSI = Restricted Spectrum Imaging, MDD-MRI = Multidimensional Diffusion MRI, HM-MRI = Hybrid Multidimensional MRI, DR-CSI = Diffusion-Relaxation Correlation Spectrum Imaging, mpMRI = Multiparametric MRI, MC DW-MRI = Monte Carlo simulations for microstructural mapping from clinical DW-MRI, AI = Artificial Intelligence.

Table 2: Table summarising the correlations observed between DKI and IVIM metrics and histological indices reported in the 54 articles included in this review. Weak correlations that in absolute value were lower than 0.2 were not included in the table. Values of r indicate Pearson's correlation coefficients, unless otherwise stated. Please refer to section 3.3 for the mathematical/physical foundations beyond each metric.

MRI metric	**Correlation with histology**
DKI ADC_K	$r = -0.24$ with cellularity in [14]; $r = -0.48$ with nuclear-to-cytoplasm ratio in [16]; $r = -0.73$ (Spearman's) with cellularity in [13]; $r = -0.77, 0.63$ with cellularity, apoptosis rate in [18]; $r = -0.40, -0.53, -0.55, 0.67$ with nuclear, cytoplasmatic, cellular and prostate stromal fractions in [17]; $r = -0.83, 0.72$ with tumour cell density, CD45 level in [19]; $r = 0.24, -0.30$ with stromal, nuclear fractions in [20]; $r = -0.21, 0.36$ with tumour area, fraction of interstitium in [21]; $r = -0.51$ (Spearman's) with tumour cellularity in [71]
DKI K	$r = 0.48$ with cellularity in [14]; $r = 0.54$ with nuclear-to-cytoplasm ratio in [16]; $r = 0.49, 0.53$ (Spearman's) with cellularity, Ki-67 positive cell count in [13]; $r = 0.28, -0.23$ with cellularity, apoptosis rate in [18]; $r = 0.49, 0.49, -0.42$ with cytoplasmatic, cellular and prostate stromal fractions in [17]; $r = 0.35, -0.24$ with tumour cell density, CD45 level in [19]; $r = -0.20, 0.26, -0.29$ with cellular, stromal, nuclear fractions in [20]; $r = 0.53, 0.24, 0.38$ with cancer cell nuclear area, lymphocyte area ratio, cancer cell nucleus size in [21]; $r = 0.28$ with tumour grade in [22]
IVIM D_t	$r = -0.33, -0.49, 0.42$ with cell count, nuclear and stromal fraction in [26]; $r = -0.46$ with perc. of fibrosis in [30]; $r = -0.89, -0.87, -0.84$ with cell density, cell area fraction, nuclear fraction in [28]; $r = -0.39$ with tumour cellularity in [27]; $r = -0.45$ (Spearman's) with nuclear-to-stromal ratio in [31]; $r = -0.20, 0.26, -0.29$ with cellular, stromal, nuclear fractions in [20]; $r = -0.35$ with a fibrosis index in [34]; $r = 0.52, -0.20, 0.54$ (Spearman's) wih necrosis fraction, microvessel density and apoptosis fraction in [35]; $r = -0.47, -0.50$ (Spearman's) with microvessel density, area with in [37]; $r = 0.51$ with microvessel density in [38]; $r = 0.84$ with necrotic fraction in [39]; $r^2 = 0.46$ ($r = -0.68$) with cell density in [40]; $r = -0.57$ with vasculogenic mimicry in [41]; $r = -0.46, -0.31$ (Spearman's) with necrotic fraction and microvessel density in [42]
IVIM D^*	$r = -0.26$ with perc. of fibrosis in [30]; $r = 0.33$ with microvessel density in [34]; $r = -0.38, 0.54, -0.69$ (Spearman's) with necrosis fraction, microvessel density and apoptosis fraction in [35]; $r = 0.78$ (Spearman's) with microvessel density in [36]; $r = -0.41, -0.37$ (Spearman's) with microvessel density and area in [37]; $r = 0.71, 0.72$ with microvessel density and pericyte coverage index in [41]; $r = 0.22$ with microvessel area fraction in [21]; $r = 0.33, 0.34$ (Spearman's) with necrotic fraction and microvessel density in [42]; $r = -0.92, -0.79$ with Ki67-positive cell fraction, diameter in [43]
IVIM f	$r = 0.35, -0.42$ with cell count, stromal fraction in [26]; $r = 0.44$ with perc. of fibrosis in [30]; $r = 0.63, 0.61, 0.58$ with endothelial area, total vessel area, microvessel count, and f entropy showed $r = -0.55$ with a Ki-67 index in [29]; $r = -0.24, 0.28, -0.24$ with cellular, stromal, nuclear fractions in [20]; $r^2 = 0.40$ (i.e., $r = 0.63$) with microvessel density in [33]; $r = 0.42$ with a fibrosis index in [34]; $r = -0.35, 0.62, -0.55$ (Spearman's) wih necrosis fraction, microvessel density and apoptosis fraction in [35]; $r = 0.75$ (Spearman's) with microvessel density in [36]; $r = 0.77, 0.82$ (Spearman's) with microvessel density and area in [37]; $r = 0.28$ with microvessel density in [38]; $r = 0.43, 0.53$ with microvessel density and necrotic fraction in [39]; $r^2 = 0.44$ ($r = 0.66$) with blood vessel density in [40]; $r = 0.52, 0.38$ with microvessel density and pericyte coverage index in [41]; $r = 0.24, 0.28, -0.37$ with cancer cell area and nuclear fractions, lymphocyte area ratio in [21]; $r = 0.40, 0.44$ (Spearman's) with necrotic fraction and microvessel density in mice injected with NCI-H226 cells, while $r = -0.51, -0.55$ in mice injected with MSTO-211H cells in [42]; $r = -0.69, -0.61$ with Ki67-positive cell fraction, diameter in [43]

Table 3: Table summarising the correlations observed between DW-MRI metrics of techniques other than DKI and IVIM and histological indices reported in the 54 articles included in this review. Weak correlations that in absolute value were lower than 0.2 were not included in the table. Values of r indicate Pearson's correlation coefficients, unless otherwise stated. Please refer to section 3.3 for the mathematical/physical foundations beyond each metric.

MRI metric	**Correlation with histology**
SEM D_{SEM}	$r = -0.23, -0.52, -0.50, 0.64$ with nuclear, cytoplasmatic, cellular and prostate stromal fractions in [17]; $r = -0.57$ (Spearman's) with tumour cellularity in [71]
SEM α	$r = -0.23, 0.22$ with cytoplasmatic fraction, nuclear-to-cytoplasm ratio [17]
VERDICT f_{ic}	$r = 0.90$ with fraction of HE stained area in [54] (DDE-VERDICT)
VERDICT R	$r = 0.68$ with minimum Feret diameter of cells in [54] (DDE-VERDICT)
IMPULSED d	$r = 0.92$ with *in vitro* mean cell diameter[64]; $r = -0.64, 0.52$ with percentage of CD3+ cells, all-cell mean diameter in [65]
IMPULSED Cellularity	$r = 0.81$ with histological cellularity in [66]
IMPULSED f_{ic}	$r = 0.83$ with nuclear fraction in [68]
QSI Mean Displacement	$r = -0.71, -0.67$ with nuclear-cytoplasmatic ratio and tumour cellularity in [73]
QSI Probability of zero displacement	$r = 0.79, 0.70$ with nuclear-cytoplasmatic ratio and tumour cellularity in [73]
QSI Propagator Kurtosis	$r = 0.73, 0.74$ with nuclear-cytoplasmatic ratio and tumour cellularity in [73]
QSI Propagator Full-Width-At-Half-Maximum	$r = -0.51$ (Spearman's) with tumour cellularity in [71]
RSI restricted fraction C_1	$r = 0.40$ with tumour grade in [22]
HM-MRI epithelial fraction	$r = 0.93$ with histological epithelial fraction in the prostate in [91]
HM-MRI lumen fraction	$r = 0.90$ with histological lumen fraction in the prostate in [91]
HM-MRI stroma fraction	$r = 0.82$ with histological stroma fraction in the prostate in [91]
DR-CSI epithelial fraction	$r = 0.74$ (Spearman's) with epithelial fraction in the prostate in [99]
DR-CSI lumen fraction	$r = 0.67$ (Spearman's) with lumen fraction in the prostate in [99]
DR-CSI stroma fraction	$r = 0.80$ (Spearman's) with stroma fraction in the prostate in [99]
DR-CSI component fractions	The signal fraction of two components out of a 5-component spectrum correlated with tumour grade in [100] ($r = 0.55$ and $r = -0.38$)

Appendix A: diffusion MRI physics fundamentals

This appendix presents the physical fundamentals of diffusion MRI, providing context to the literature review. In the following, the terms *water molecules*, *protons* and *spins* will be used interchangeably to refer to the motion of them.

Diffusion encoding

Time-varying magnetic field gradients are used to sensitise the MRI signal to diffusion. The classical DW-MRI experiment is based on the Pulsed-Gradient Spin-Echo (PGSE) approach, also known as the Stejskal-Tanner experiment, single diffusion encoding, or, more recently, as linear b-tensor encoding. The schematic of a PGSE sequence is shown in Fig. 1.

The PGSE approach is based on the spin echo experiment, in which two radiofrequency (RF) pulses, of flip angle 90° and 180°, separated by a time $\mathrm{TE}/2$ are used to irradiate the sample. The first pulse excites the tissue, creating a component of magnetisation orthogonal to the static field. The second pulse refocuses the magnetisation by cancelling out the effect of field inhomogeneities. The signal is sampled at a time TE, i.e., when the refocussing is complete, and the signal is weighted by the underlying T2 relaxation constant, i.e., proportional to $e^{-\frac{\mathrm{TE}}{T2}}$. In PGSE, two magnetic field gradient lobes (known as diffusion-encoding gradients) are added on either side of the refocussing pulse. The first gradient lobe effectively tags water molecule's phases depending on their spatial position, so that their phases will now depend on their position along the gradient direction. Conversely, the effect of the combination of the refocussing pulse and of the second gradient lobe is that of cancelling out the phase distribution modulation caused by the previous lobe, for those molecules that do not move. If all spins were perfectly static during diffusion-encoding, one would measure the same T2-weighted signal that one would have obtained without diffusion encoding. However, due to diffusion, water molecules change their position in between the two gradient lobes, as well as during the application of each lobe itself. This implies that a full phase coherence over the spin ensemble will not be re-established at the echo time $t = \mathrm{TE}$, so that the signal measured will be smaller than the one obtained without diffusion-weighting, leading to signal attenuation. The amount of attenuation increases as the degree of diffusion taking place increases, resulting in DW images of lower intensity.

b-value and diffusion time

The amount of signal loss caused by diffusion-weighting depends on several factors. Some depend on the tissue being imaged, such as the underlying intrinsic diffusion coefficient and the characteristics of the microstructure, e.g., type and features of the biological structures that restrict or hinder diffusion. These features include, for example, the density and size of cells. Other factors depend instead on the acquisition, and are: the gradient magnitude G, the gradient duration δ, and the gradient separation Δ (see Fig. 1). The total DW-signal S is the ensemble average of the signals from all spins, i.e.,

$$S \;=\; S_0 \,< e^{i\phi} > \tag{16}$$

where S_0 is the T2-weighted, non-DW-reference signal and ϕ is the phase accrued by a generic spin. ϕ depends on the interaction between a spin's random walk over time $\mathbf{r}(t)$ and the temporal evolution of the diffusion encoding gradient $\mathbf{g}(t)$, i.e.,

$$\phi \;=\; -\gamma \int_0^{\mathrm{TE}} \mathbf{g}(t) \cdot \mathbf{r}(t)\, dt. \tag{17}$$

For free water self-diffusion without any barriers, equation 16 simplifies to

$$S \;=\; S_0 \, \exp(-b \, D_{water}). \tag{18}$$

Above, S_0 is the non-DW signal (proton density-, T2- and potentially T1-weighted), whereas D_{water} is the intrinsic diffusivity of water at the experiment temperature, and b provides a general indication of the overall strength of the diffusion-weighting. This factor depends on the acquisition settings, and is routinely known as b-value. It can be calculated as:

$$b = \gamma^2 G^2 \delta^2 (\Delta - \delta/3) \tag{19}$$

where γ is the proton gyromagnetic ratio, and G, δ and Δ the gradient parameters. Another useful sequence parameter is the overall diffusion time $t_{diff} = \Delta - \delta/3$. This provides an indication of the amount of time that diffusing water molecules are allowed to experience the microstructure, before the MRI signal is acquired.

Intra-voxel heterogeneity mapping with PGSE

The voxel size of *in vivo* MRI in humans is of the order of a few cube millimetres. The observed MR-signal in a voxel arises from contributions of various diffusion processes taking place within different cellular components, since the voxel size is much larger than the scale of the microstructure where diffusion takes place ($\sim 1 - 100 \mu m$). As a consequence, *in vivo* DW-MRI measurements are characterised by intrinsic, intra-voxel partial volume effects, and the signal entangles the contribution of multiple water pools in one measurement. Different techniques have been proposed to disentangle such contributions, with the ultimate aim of obtaining sensitive and specific biomarkers of tissue microstructure. The solutions proposed in the literature span phenomenological signal representations (e.g., estimation of apparent diffusion and kurtosis coefficients, stretched exponential, anomalous diffusion), multi-compartment biophysical models, and include recent approaches based on innovative diffusion acquisitions such as double diffusion encoding and b-tensor encoding [4, 86].

The section below provides a general overview of the techniques available for microstructure inference in DW-MRI. The section aims to provide some context for the detailed description of the methods found in our systematic literature search. Importantly, we point out that the inference of microstructure from signal measurements is a challenging task: different combinations of microstructural parameters can provide virtually indistinguishable signals in certain measurement regimes and in the presence of noise, making microstructure estimation an ill-posed inverse problem [114].

Phenomenological signal representations It can be shown that the signal in Eq. (16) can be expanded as a function of increasing powers of the b-value, i.e., $ln(S) \;\sim\; \sum_{k=1} a_k \, b^k$ (the cumulant expansion [23]), where coefficients a_k are related to the cumulants of the spin displacement distribution within a voxel. Expanding Eq.

(16) up to the second power of b (i.e., with an approximation error proportional to $O(b^3)$), provides

$$S = S_0\, e^{-b\, ADC\ +\frac{1}{6}K(b\, ADC)^2} \tag{20}$$

In Eq. (20) above, ADC and K are respectively the apparent diffusion and excess kurtosis coefficients along the direction of the diffusion encoding gradient. ADC provides a measurement of the overall amount of diffusion taking place during the measurement along the gradient direction, so that higher ADC implies stronger signal decay. Conversely, K gives an indication of how much the diffusion process departs from Gaussian, free diffusion. While $K = 0$ would imply perfectly Gaussian diffusion, i.e., mono-exponential signal decay, a non-zero K can arise when i) multiple Gaussian water pools with different intrinsic diffusivities are found inside the same voxel, ii) diffusion is restricted by geometric confinements, iii) orientation dispersion of microscopic domains exists within the voxel, iv) different water compartment exchange water during the MRI signal encoding, or by a combination of all of these. Signal representations as those in Eq. (20) are sometimes referred to as *phenomenological*: they provide a description of the signal and link this to the statistical moments of the spin displacement distribution, but without seeking to estimate the biophysical *causes* of the observed diffusion phenomenon (e.g., without trying to estimate biophysical properties such as cell size, cell density, etc). On the one hand, phenomenological representations do not make any assumptions on the geometry of the tissue (e.g., modelling cells as spheres [60]). On the other hand, measures such as ADC or K may be difficult to interpret, being surrogate indices that entail contributions from multiple biological factors in one number.

When the b-value is not too high (generally, not exceeding 400-800 s/mm^2 in body imaging or 1000-1500 s/mm^2 in the brain), the first-order term in the b-value (cumulant) expansion is dominant, and the expansion reduces to

$$S = S_0 e^{-b\, ADC} \tag{21}$$

where S_0 is the non-DW-signal, b the b-value and ADC is the apparent diffusion coefficient. ADC is a sensitive marker of tissue microstructure, but has relatively poor biological specificity, since contributions from different water compartments within the same voxel (e.g., intra-/extra-cellular water) are pooled together in one, average number. This implies that ADC measurements do not describe the complicated diffusion process in heterogeneous microstructures accurately: signal contributions from different processes within a voxel, including pseudo-diffusion due to perfusion, are integrated and modelled by one single diffusion coefficient, which also depends on the particular diffusion times used for the acquisition (e.g., gradient duration δ and gradient separation Δ). Due to this, the ADC is defined as an 'apparent' coefficient. Nonetheless, ADC is easy to obtain (ADC maps can be computed with as few as two images), and offers sensitivity to alterations in tissue microstructure due to pathology, classification or grading of tumours, and therapy response assessment.

Multi-compartment biophysical modelling Multi-compartment biophysical models describe the DW-signal as arising from the contribution of multiple water pools located in different cellular compartments, as for example intra-cellular or extra-cellular water. Fitting such models to sets of DW-measurements may provide voxel-wise estimates of salient biophysical properties, as for example intra-cellular water fraction or characteristic restriction size, effectively reflecting intra-voxel cell size statistics.

The number and characteristics of the tissue parameters that can be estimated depends on the assumptions made when building the geometric representation of the biophysical model - e.g., spherical vs elongated cells, characteristics of the cell size distribution, etc - as well as on the acquisition protocol. The most common tissue parameters that are estimated in biophysical modelling are:

- compartment-wise signal fractions, e.g., f_{vasc}, f_{ic}, or f_{EES}, which respectively represent the fraction of signal coming from vascular water, intra-cellular water and extra-cellular extra-vascular water;
- cell size radius R or diameter d in μm;
- cellularity indices C, i.e. with units in $cells/mm^2$ or $cells/mm^3$. A common way of estimating C is to combine metrics such as f_{ic} and d in one number, e.g., $C \propto \frac{f_{ic}}{d^3}$ [55].

Other approaches beyond PGSE

PGSE is the most common diffusion MRI acquisition implementation, and is available in virtually all clinical scanners. However, several other implementations of the DW-MRI experiment exist. Some of the latest implementations probe new diffusion contrasts that are not physically accessible with standard PGSE, and therefore offer great promise for the development of new biomarkers of cancer. Nevertheless, these more advanced implementations often come at a price, as for example the need for strong gradient systems, longer echo times TE, and may not yet be available as vendor-provided implementations on clinical systems.

Oscillating gradient spin echo (OGSE) is similar to PGSE, in that two diffusion gradient wave forms are inserted on either side of the refocussing pulse of a spin echo sequence. However, in OGSE, the gradient is not pulsed, but it is rather made of an oscillating waveform at a specific frequency f [123]. A key characteristic of OGSE is that it enables probing much shorter effective diffusion times t_{diff} than PGSE, at a given b-value.

Double-diffusion encoding (DDE) combines in one acquisition two diffusion encoding blocks, separated by a mixing time [54]. The two diffusion encoding gradients are consecutively applied with two different orientations, separated by a relative angle ψ. DDE enables probing diffusion correlations, resolving properties of microscopic domains (e.g., anisotropy and/or eccentricity of pores where restricted diffusion takes place) without the confounding effect of the macroscopic, orientational arrangement of the ensemble of the microscopic domains.

DDE also finds application in Filter-Exchange Imaging (FEXI) [48]. In FEXI, a first diffusion encoding block acts as a filter that suppresses the signal from fast diffusing components. The signal read at the end of the second block will be modulated by the amount of water exchange between water compartments taking place during the

mixing time. FEXI has been used to measure the apparent exchange rate (sensitive to cell membrane permeability, but it is not a measure of permeability as such) and other exchange processes, as for example in breast cancer [48].

Multidimensional Diffusion (MDD) MRI is an innovative diffusion MRI framework that relies on a new diffusion encoding paradigm (also known as b-tensor encoding, or q-space trajectory imaging) [4, 83, 84, 88]. MDD generalises the traditional approach based on PGSE (which is, in fact, a special case of b-tensor diffusion gradient), sensitising the measurements to different diffusion directions at once and thus probing new diffusion contrasts that are not accessible to standard PGSE.

Appendix B: Search query

(”cell size*”[tiab] OR ”intra-cellular fraction*”[tiab] OR cellularity[tiab] OR cytometry[tiab] OR ”Cell Size”[Mesh] OR ”cell density”[tiab] OR ”volume fraction*” OR ”component fraction*”[tiab] OR ”perfusion fraction*”[tiab] OR ”vascular fraction*”[tiab] OR ”fractional volume*”[tiab] OR ”tissue component*”[tiab] OR ”tissue composition*”[tiab])

AND (histolog*[tiab] OR histologic[tiab] or histologically[tiab] OR histology[tiab] OR histopatholog*[tiab] OR patholog*[tiab] OR microstructur*[tiab])

AND (oncology[tiab] OR tumor[tiab] OR tumour[tiab] OR abdominal[tiab] OR liver[tiab] OR pelvic[tiab] OR hepato*[tiab] OR musc*[tiab] OR cancer[tiab] OR prostate*[tiab])

AND (”DW-MRI”[tiab] OR ”diffusion MRI”[tiab] OR ”dMRI”[tiab] OR ”diffusion weighted imaging”[tiab] OR ”DWI”[tiab] OR ”Diffusion Magnetic Resonance Imaging”[tiab] OR ”Diffusion Magnetic Resonance Imaging”[Mesh] OR ”Diffusion-relaxometry”[tiab] OR ”Diffusion Relaxometry”[tiab] OR DWI[tiab] OR ”multidimensional MRI”[tiab] OR ”multiparametric MRI”[tiab] OR mpMRI[tiab] OR bpMRI[tiab] OR mp-MRI[tiab] OR ”multi-parametric MRI”[tiab])

AND (estimat*[tiab] OR predict*[tiab] OR correlat*[tiab] OR validat*[tiab])

NOT (neuro*[tiab] OR cerebral*[tiab] OR ”Neurology”[Mesh] OR ”Brain”[Mesh] OR brain[tiab])

Appendix C: Fitting algorithms

Table 4: Different fitting algorithms that can be used to fit the IVIM-model to measured DW-MR signal data [47, 116]. The algorithm that is used the most for both IVIM fitting and VERDICT fitting is LM.

Algorithm	**Type**	**Estimated parameters**	**Method description**
Levenberg-Marquardt (LM)	Least-squares	D_t, f, D^*	- Determines values of the three parameters simultaneously in each voxel - No boundary constraints possible
Trust-Region (TR) based	Least-squares	D_t, f, D^*	- Determines values of the three parameters simultaneously in each voxel - Uses restricted search space, boundary constraints easily incorporated
Fixed-D^*	Least-squares	f, D_t	- Same as TR, but now with D^* fixed to a value defined a priori
Segmented-Unconstrained (SU)	Multi-step	In first step: D_t and f In second step: D^*	- Most frequently used algorithm for IVIM analysis - Uses assumption that D^t is dominant at high b-values and that D^* is negligible here - Uses TR based algorithm in the second step
Segmented-Constrained (SC)	Multi-step	In first step: D_t and f In second step: D^*	- Similar to SU - Now assumes that the intercept of S is equal to S_0
Bayesian-Probability (BP)	BP-based	D_t, f, D^*	- Does not fit each voxel independently - Fits using a kind of spatial similarity additional information incorporated
Deep Neural Network (DNN)	Auto-encoder	D_t, f, D^*	- Unsupervised network with three hidden layers - Constraint: the input signal should be encoded by the three IVIM-parameters - Increased fitting speed in comparison with LM and BP-algorithms

Figures

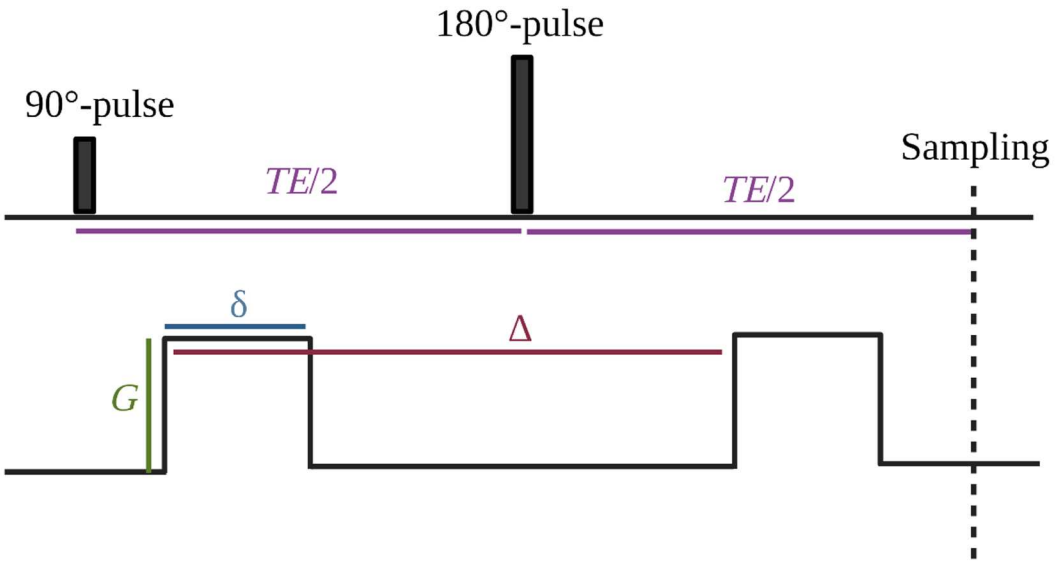

Figure 1 Schematic of the idealised Pulsed-Gradient Spin-Echo (PGSE) sequence. The first and second radiofrequency (RF) pulses rotate the magnetisation vector by 90° and 180° respectively. These two pulses are characteristic for a spin-echo sequence, as they consecutively excite and refocus the magnetisation. After a time TE (the echo time), a spin echo is formed and the centre of the k-space is sampled. The diffusion encoding gradient consists of two pulsed wave forms on each side of the 180°, which diffusion-weight the spin echo. The diffusion gradient is characterised by a gradient magnitude G, the gradient duration δ, and the separation time in between the two gradient lobes Δ. Note that the figure represents a simplified theoretical schematic of PGSE. In real world, the gradient pulses are not rectangular but rather trapezoidal, due to technical requirements.

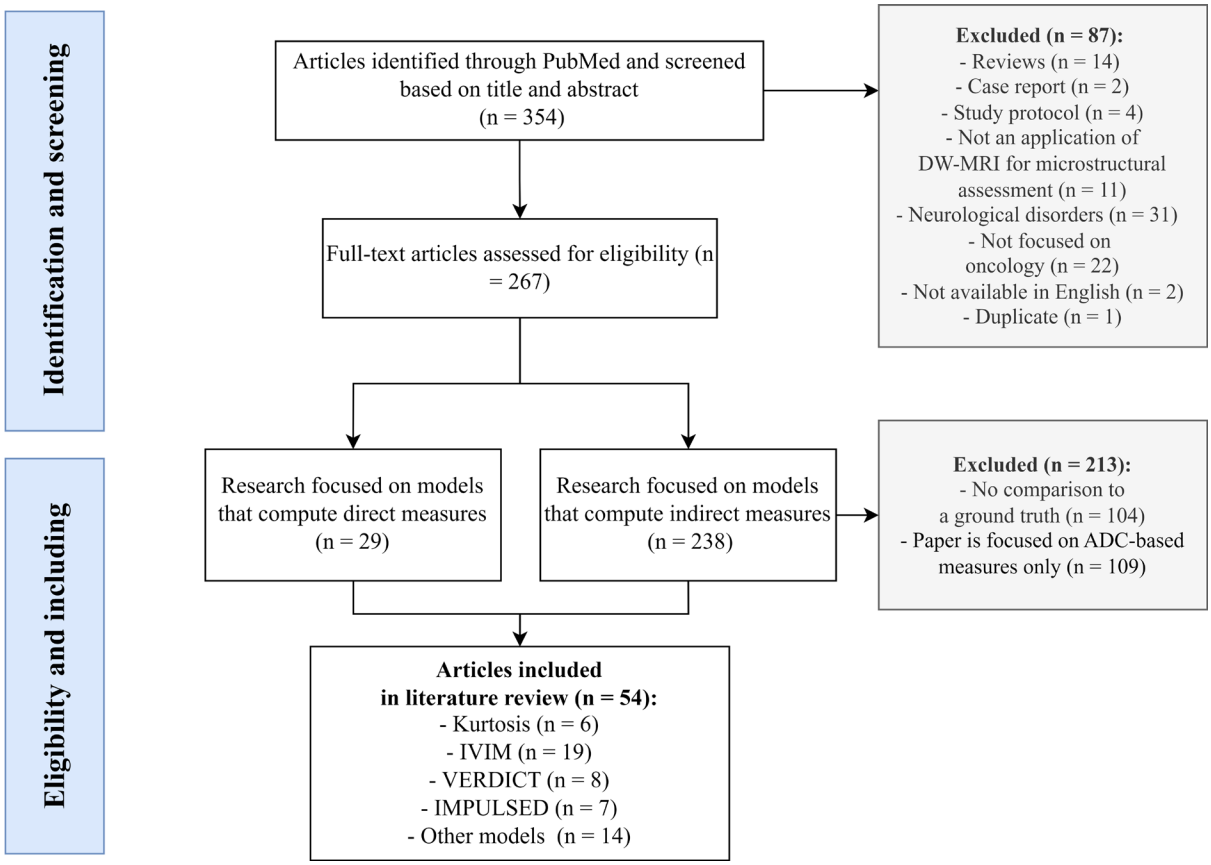

Figure 2 Flow chart of the literature search in PubMed. Acronyms stand for: DW = diffusion-weighted, IVIM = Intravoxel Incoherent Motion, VERDICT = Vascular, Extracellular, and Restricted Diffusion for Cytometry in Tumours, IMPULSED = Imaging Microstructural Parameters Using Limited Spectrally Edited Diffusion.

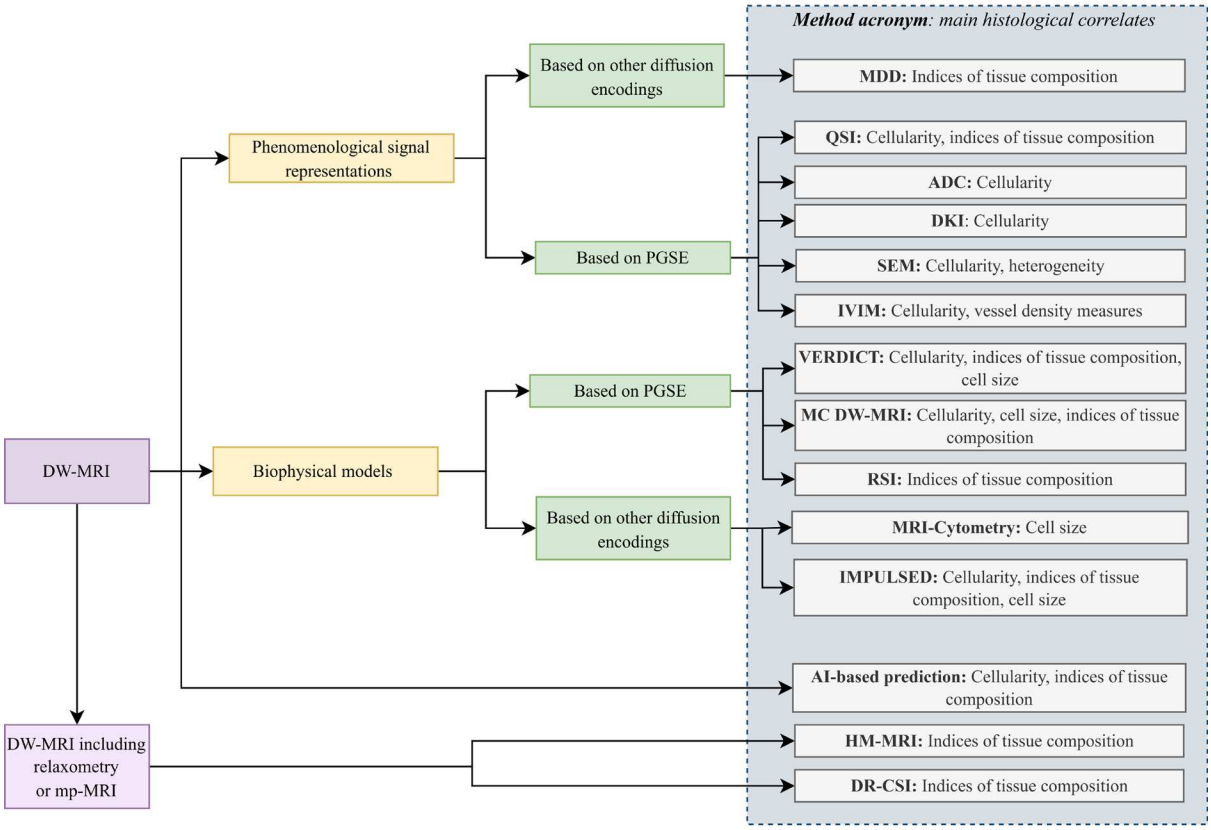

Figure 3 A visual summary of the techniques found in the literature search and their main histological correlates. PGSE = Pulsed Gradient Spin Echo, DKI = Diffusion Kurtosis Imaging, IVIM = Intravoxel Incoherent Motion, VERDICT = Vascular, Extracellular, and Restricted Diffusion for Cytometry in Tumours, IMPULSED = Imaging Microstructural Parameters Using Limited Spectrally Edited Diffusion, SEM = Stretched Exponential Modelling, QSI = q-space imaging, RSI = Restricted Spectrum Imaging, MDD-MRI = Multidimensional Diffusion MRI, HM-MRI = Hybrid Multidimensional MRI, DR-CSI = Diffusion-Relaxation Correlation Spectrum Imaging, MC DW-MRI = Monte Carlo simulations for microstructural mapping from clinical DW, mpMRI = Multiparametric MRI, AI = Artificial Intelligence.

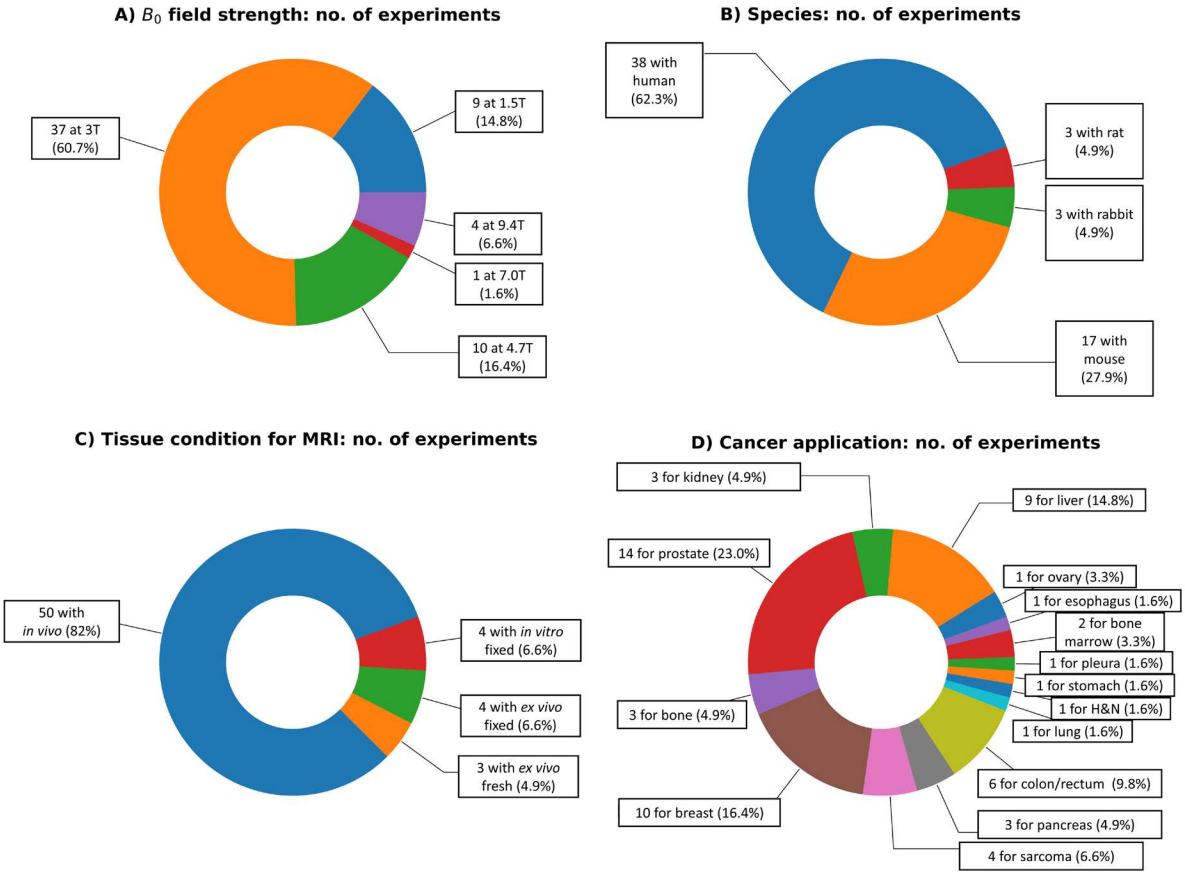

Figure 4 Salient statistics regarding the MRI-histology experiments performed in the identified articles. (A): B_0 magnetic field strength used for MRI. (B): species from which the imaged tissues were obtained. (C): tissue condition during MRI. (D): main cancer application.

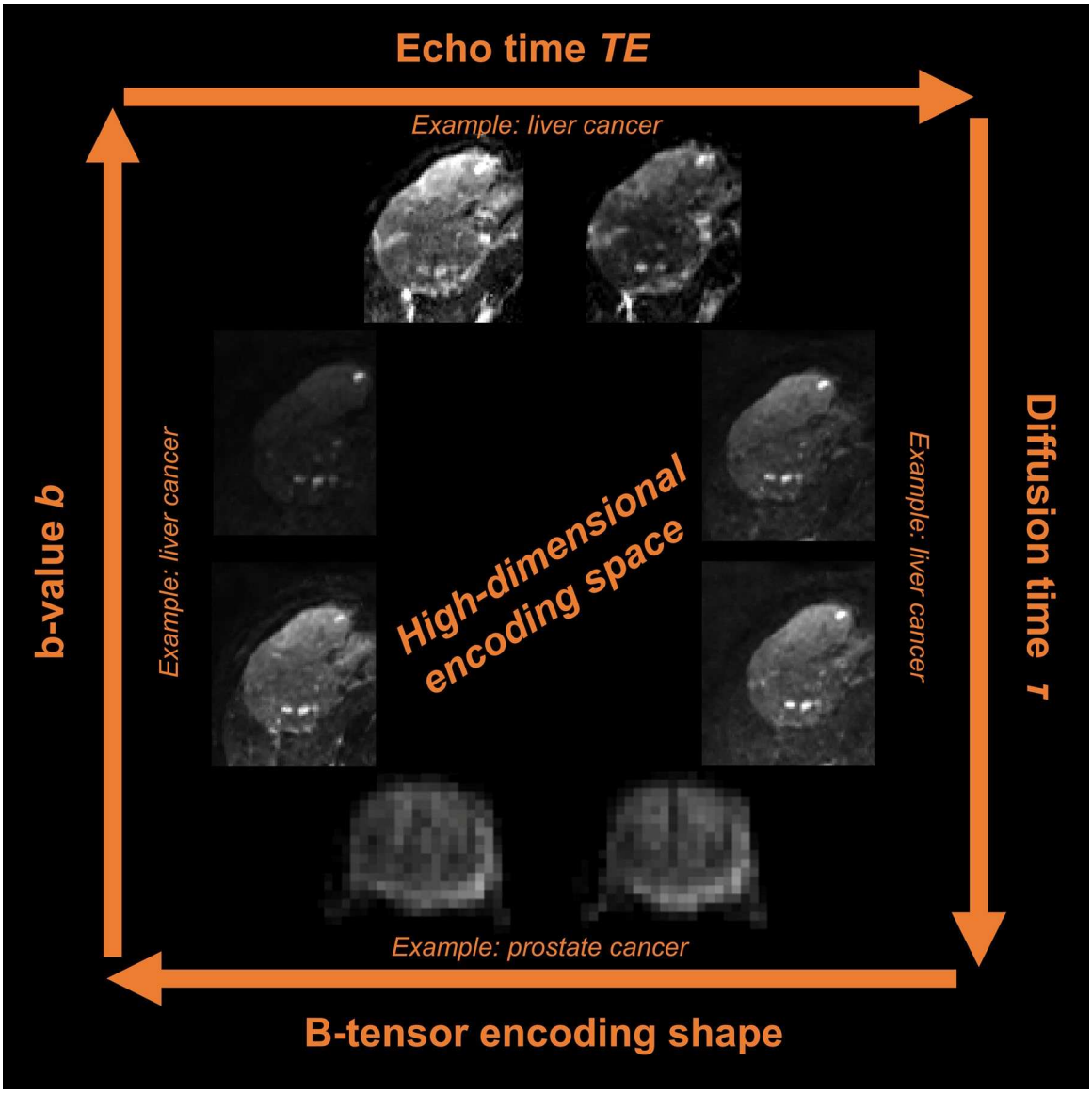

Figure 5 Illustration of the acquisition space exploited in advanced DW-MRI techniques. The figure illustrates the main acquisition parameters that can be varied to generate high-dimensional multi-contrast image sets in advanced diffusion imaging, i.e., changes in b-value (overall diffusion-weighting strength), b-tensor encoding shape (e.g., planar, spherical or routine linear encoding), diffusion time, as well as potential changes in echo, inversion or repetition times for joint diffusion-relaxation imaging. Changes in b-value, diffusion time and echo time are illustrated with a hepatocellular carcinoma (primary liver cancer) case, scanned at 1.5T. Changes in b-tensor encoding shape are instead illustrated with a prostate cancer case, scanned at 3T. The prostate images have been adapted from Figure 2 of reference [86], which was published in open access form under a CC-BY Attribution 4.0 International license.

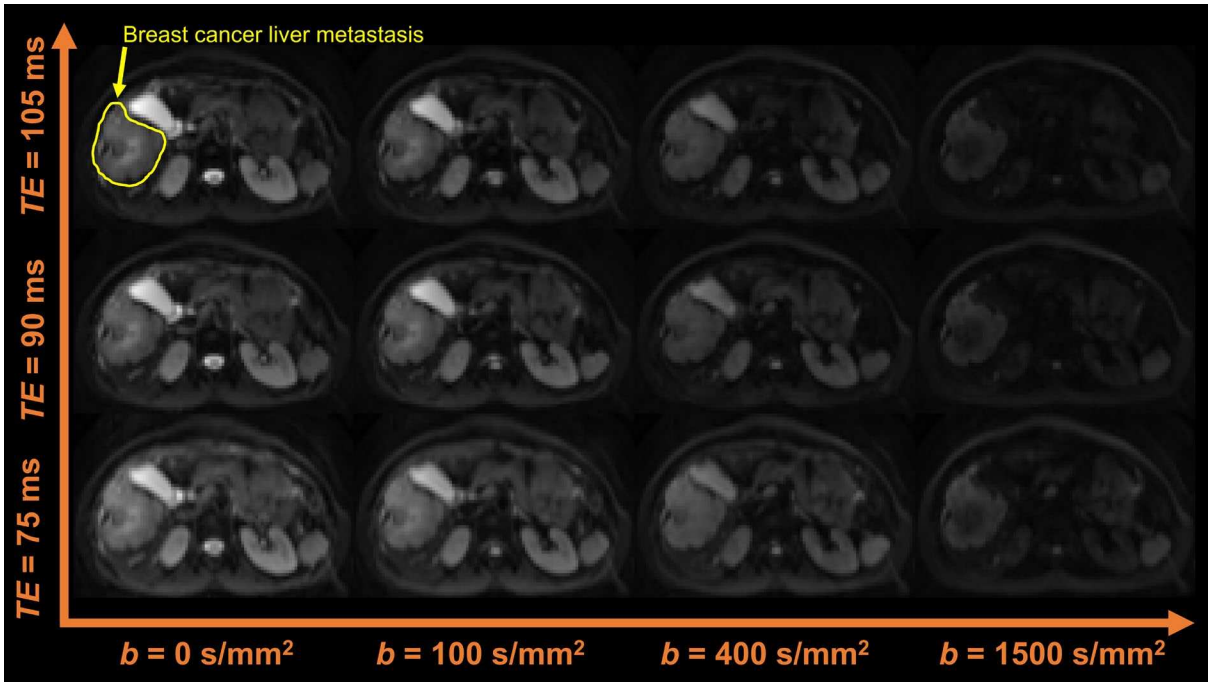

Figure 6 Example of a rich, advanced DW-MRI acquisition in body cancer. The figure shows a diffusion-relaxation acquisition performed at the level of the abdomen with a 3T system, to image a breast cancer liver metastasis. The diffusion protocol features the acquisitions of multiple b-values b with LTE, each acquired independently at several echo times TE.

Supporting Information

Supporting Information Tables S1 to S7 Summary of the content of the 54 articles included in the literature review.

Supporting Information Data D1 CSV file storing information on the type of tissue being imaged (species and condition during MRI, e.g., fresh or fixed), the target anatomy and the cancer application for all the MRI-histology experiments included in the 54 articles part of this review. Note that the data set contains more than 54 entries, as in some articles multiple experiments on different tissues were performed.

List of Abbreviations

Abbreviation	Definition
PGSE	Pulsed Gradient Spin-Echo
TR	Repetition time
TE	Echo time
ADC	Apparent Diffusion Coefficient
DKI, K, ADC_K	Diffusion Kurtosis Imaging, Kurtosis, diffusion coefficient corrected for kurtosis
HCC	Hepatocellular Carcinoma
SNR	Signal-to-Noise ratio
N/C ratio	Nuclear-to-cytoplasm ratio
SEM, D_{SEM}, α	Stretched Exponential Model, mean diffusion coefficient, heterogeneity index
IVIM, D_t, D*, *f*	Intravoxel Incoherent Motion, true diffusion coefficient, pseudo-diffusion coefficient, perfusion fraction
VERDICT	Vascular, Extracellular, and Restricted Diffusion for Cytometry in Tumors
f_{ic}, f_{EES}, f_{vasc} d_{ic}, d_{EES}, d_{vasc}	Intracellular fraction, extracellular-extravascular space fraction, vascular fraction Intracellular diffusion coefficient, extracellular-extravascular space diffusion coefficient, vascular diffusion coefficient
ROC, AUC	Receiver Operator Curve, Area Under the Curve
LM	Levenberg-Marquardt fitting algorithm
ICC	Intraclass Correlation Coefficient
BVD, MVD, MVA	Blood Vessel Density, Mean Vessel Density, Mean Vessel Area
CD, TCD	Cell Density, Tumour Cell Density
AMICO	Accelerated Microstructure Imaging via Convex Optimization

Abbreviation	Definition
R, d, L	Cell size radius, cell size diameter, volume-weighted cell size
AIC	Akaike Information Criteria
ROI	Region of Interest
DDE	Double Diffusion Encoding
TDD	Time Dependency Diffusion
RSD	Relative Standard Deviation
OGSE	Oscillating Gradient Spin-Echo
IMPULSED	
τ_{in}, P_m	Pre-exchange lifetime of intracellular water, cell membrane permeabillity
1P-MM, 2P-MM	One-cell population microstructure model, Two-cell population microstructure model
MDD	Multidimensional Diffusion MRI
DTD	Diffusion Tensor Distributions
E, V	Mean, Variance
D_{ISO}, $D_{\Delta 2}$	Tensor size, tensor shape
RSI	Restricted Spectrum Imaging
QSI	q-space Imaging
HM-MRI	Hybrid Multidimensional MRI
CCC	Lin's Concordance Correlation Coefficient
DR-CSI	Diffusion-Relaxation Correlation Spectrum
bp-MRI, mp-MRI	Bi-parametric MRI, multiparametric MRI
ML, DL, CNN	Machine Learning, Deep Learning, Convolutional Neural Network

Table 1. Information extraction of the articles that reported an evaluation of the *Kurtosis* model – continues on next page [1/2].

Author (year)	Study goal	MRI scanner	Salient Diffusion protocol	Tissue condition on MRI	Extra model specifics	Models compared to	Quantitative comparison with histology or simulated data	Discussion: value for assessment of microstructural properties	Discussion: Other advantages Other limitations
Deen (2019)	Assess clinical feasibility of DKI for prediction of response to therapy	Clinical 3T MRI scanner (Discovery MR750, GE Healthcare, Waukesha WI)	PGSE, b = {0, 100, 500, 900, 1300, 1700} s/mm2 each at TR/TE = 6000/94 ms	• In vivo Ovarian cancer, humans	/	ADC	***Histology, correlation:*** Cellularity vs.: • K (ρ=0.49, p=0.04) • ADC_K (ρ=-0.77, p=0.02) • ADC (ρ=-0.73, p=0.03)	• Significant correlation ADC_K, K and cellularity, but not superior than ADC	• Good intraobserver and interobserver agreement for all diffusion metrics •Significant difference in K for therapy responders and non-responders - not for ADC and ADC_K
Rosenkrantz (2012)	Assessing hepatocellular carcinoma using DKI	1.5-T clinical MR scanner (Magnetom Avanto, Siemens Healthcare)	PGSE, b = {0, 500,1000, 1500, 200} s/mm2 each at TR/TE = 4900/100 ms	• Ex vivo, fresh liver explant refrigerated, maximal delay between explantation and ex vivo imaging 10 hours Hepatocellular carcinoma, humans	/	ADC	***Histology, correlation:*** Cellularity vs: • ADC, weak • ADC_K, weak • K, weak ADC vs.: • ADC_K, r=0.91, p<0.001 • K, r=-0.79, p<0.017 ADC_K vs.: • K, r=-0.79, p<0.001	• K did not correlate with cellularity • The lack of correlation could reflect overlap in structural heterogeneity measured by K among tumors with different cellularity levels • Another option is that the influence of higher order cellular topology measured by K is not captured by histological cellularity measures. • In a subgroup of the tumours, there was a significant correlation between ADC and cellularity; but still none for K	• K showed the greatest HCC-to-liver contrast in comparison ADC and K • All tumours showed excess K greater than 0.50; indicating non-Gaussian diffusion is present in all HCC • There was a lack of strong correlation between ADC, ADC_K vs. K., which suggests complementary, nonredundant information offered by K. • K had a significantly greater coefficient of variation than ADC or ADC_K, which can point either to greater sensitivity to tissue heterogeneity or greater statistical variation. The latter is more likely.
Grussu (2022)	Test a method for mapping DKI-parameters to cell size and diffusivity, from DW-MR data acquired at fixed diffusion time	Preclinical 9.4T Bruker Avance	PGSE, 10 b-values in [0; 4500] s/mm2, TR/TE = 2700/45 ms, {δ,Δ} = {10, 30} ms b > 1700 was used for model fitting	• Simulation study • Ex vivo, formalin-fixed mouse liver cancer	ADC_K and K are used as input for estimation of intrinsic cell diffusivity D_0 and cell size measure L. ADC_K, K were fit using non-linear least-squares fitting. Two models are used to map from (ADC_K,K) to D_0 and (ADC_K,K) to L: •**PolyMap:** based on polynomial function • **SigFit:** a biophysical model for the intracellular DW signal	/	***Simulation*** : • PolyMap does not predict D0 and L accurately, but does capture salient characteristics of the relationships • Cell sizes can be classified in small - medium - large categories with an accuracy up to 0.7 • D_0 and L are over/underestimated at the lower/upper end of their ranges; extent varies with gradient timings. ***Histology*** : • L agrees well with L_histo for both models for PDX type tumour; for WT, L is larger than L_histo especially for PolyMap.	• ADC_K and K offer sensitivity to D0 and L even at realistic SNR (=20) • The models capture salient cell-size contrast at fixed diffusion time • The mappings provide cell-size contrasts that correspond with histology, even though estimates are not accurate for largest and smallest values; they can still be used to characterize cell-size variations • Relatively small changes in D0 and L cause large variations of K and ADC_K, which implies that kurtosis captures deviations from Gaussian diffusion well • A higher SNR and longer tdiff lead to smaller error	*PolyMap vs. SigFit:* • PolyMap predicts smoother than SigFit, has higher precision than SigFit • D0 is more variable for SigFit than for PolyMap • PolyMap detects PDX-WT differences in D0 unlike SIgFit • Both models provide a good quality of fit • Results quantify how much information can be retrieved with minimal schemes like this one with one fixed diffusion time: the relative performances of both models depend on diffusion sequence; it may be feasible to obtain cell size values if the right technique is used even with a fixed diffusion time. When a rich sequence might not be possible this is useful. However, acquiring data at varying diffusion weightings is still preferred method. • Mappings do not estimate D0 and L accurately for the studied range. This could be improved by using more advanced mapping strategies - such as random forestmodels - or using voxel-wise fitting. • Mappings overestimate histological cell size, especially for larger cells • Not yet tested with clinical acquisition protocol; now at 9.4T
Wu (2017)	Compare performance of DKI and DWI for characterization of renal cancer	Clinical 1.5T MR scanner (uMR 550; United Imaging Healthcare, Shanghai,China)	PGSE, b = {0, 300, 600} s/ mm2, TR/TE = 3000/57 ms	In vivo Clear Cell Renal Cell Carcinoma, humans	/	/	***Histology, correlation:*** Nuclear-to-cytoplasm ratio vs.: • ADC_K, r=-0.474, p<0.001 • K, r=0.543, p<0.001 No correlation with cell nuclei count or intracellular fraciton (*cell volume fraction* here).	• In addition to mean kurtosis, also radial and axial kurtosis were measured. These parameters are defined to specifically address direction-dependent K, not useful for determining microstructural properties of whole tumours. • There is a correlation between ADC_K and K and N/C ratio, but no correlation between K and cellularity measures.	• Good intraobserver and interobserver agreement for each parameter • MK is promising for differentiation of tumour grades. • Low b-values only were used in this study, higher clinical feasibility; does give less information though. • Mechanism between relationship of alterations in kurtosis metrics and tumour grades has yet to be determined.

Table 1. Information extraction of the articles that reported an evaluation of the *Kurtosis* technique – final page [2/2].

Author (year)	Study goal	MRI scanner	Salient Diffusion protocol	Tissue condition on MRI	Extra model specifics	Models compared to	Quantitative comparison with histology or simulated data	Discussion: value for assessment of microstructural properties	Discussion: Other advantages Other limitations
Deen (2019)	Assess clinical feasibility of DKI for prediction of response to therapy	Clinical 3T MRI scanner (Discovery MR750, GE Healthcare, Waukesha WI)	PGSE, b = {0, 100, 500, 900, 1300, 1700} s/mm2 each at TR/TE = 6000/94 ms	• In vivo Ovarian cancer, humans	/	ADC	***Histology, correlation:*** Cellularity vs.: • K (ρ=0.49, p=0.04) • ADC_K (ρ=-0.77, p=0.02) • ADC (ρ=-0.73, p=0.03)	• Significant correlation ADC_K, K and cellularity, but not superior than ADC	• Good intraobserver and interobserver agreement for all diffusion metrics •Significant difference in K for therapy responders and non-responders - not for ADC and ADC_K
Rosenkrantz (2012)	Assessing hepatocellular carcinoma using DKI	1.5-T clinical MR scanner (Magnetom Avanto, Siemens Healthcare)	PGSE, b = {0, 500,1000, 1500, 200} s/mm2 each at TR/TE = 4900/100 ms	• Ex vivo, fresh liver explant refrigerated, maximal delay between explantation and ex vivo imaging 10 hours Hepatocellular carcinoma, humans	/	ADC	***Histology, correlation:*** Cellularity vs: • ADC, weak • ADC_K, weak • K, weak ADC vs.: • ADC_K, r=0.91, p<0.001 • K, r=-0.79, p<0.017 ADC_K vs.: • K, r=-0.79, p<0.001	• K did not correlate with cellularity • The lack of correlation could reflect overlap in structural heterogeneity measured by K among tumors with different cellularity levels • Another option is that the influence of higher order cellular topology measured by K is not captured by histological cellularity measures. • In a subgroup of the tumours, there was a significant correlation between ADC and cellularity; but still none for K	• K showed the greatest HCC-to-liver contrast in comparison ADC and K • All tumours showed excess K greater than 0.50; indicating non-Gaussian diffusion is present in all HCC • There was a lack of strong correlation between ADC, ADC_K vs. K., which suggests complementary, nonredundant information offered by K. • K had a significantly greater coefficient of variation than ADC or ADC_K, which can point either to greater sensitivity to tissue heterogeneity or greater statistical variation. The latter is more likely.
Grussu (2022)	Test a method for mapping DKI-parameters to cell size and diffusivity, from DW-MR data acquired at fixed diffusion time	Preclinical 9.4T Bruker Avance	PGSE, 10 b-values in [0; 4500] s/mm2, TR/TE = 2700/45 ms, {δ,Δ} = {10, 30} ms b > 1700 was used for model fitting	• Simulation study • Ex vivo, formalin-fixed mouse liver cancer	ADC_K and K are used as input for estimation of intrinsic cell diffusivity D_0 and cell size measure L. ADC_K, K were fit using non-linear least-squares fitting. Two models are used to map from (ADC_K,K) to D_0 and (ADC_K,K) to L: •**PolyMap:** based on polynomial function • **SigFit:** a biophysical model for the intracellular DW signal	/	***Simulation*** : • PolyMap does not predict D0 and L accurately, but does capture salient characteristics of the relationships • Cell sizes can be classified in small - medium - large categories with an accuracy up to 0.7 • D_0 and L are over/underestimated at the lower/upper end of their ranges; extent varies with gradient timings. ***Histology*** : • L agrees well with L_histo for both models for PDX type tumour; for WT, L is larger than L_histo especially for PolyMap.	• ADC_k and K offer sensitivity to D0 and L even at realistic SNR (=20) • The models capture salient cell-size contrast at fixed diffusion time • The mappings provide cell-size contrasts that correspond with histology, even though estimates are not accurate for largest and smallest values; they can still be used to characterize cell-size variations • Relatively small changes in D0 and L cause large variations of K and ADC_k, which implies that kurtosis captures deviations from Gaussian diffusion well • A higher SNR and longer tdiff lead to smaller error	*PolyMap vs. SigFit:* • PolyMap predicts smoother than SigFit, has higher precision than SigFit • D0 is more variable for SigFit than for PolyMap • PolyMap detects PDX-WT differences in D0 unlike SIgFit • Both models provide a good quality of fit • Results quantify how much information can be retrieved with minimal schemes like this one with one fixed diffusion time: the relative performances of both models depend on diffusion sequence; it may be feasible to obtain cell size values if the right technique is used even with a fixed diffusion time. When a rich sequence might not be possible this is useful. However, acquiring data at varying diffusion weightings is still preferred method. • Mappings do not estimate D0 and L accurately for the studied range. This could be improved by using more advanced mapping strategies - such as random forestmodels - or using voxel-wise fitting. • Mappings overestimate histological cell size, especially for larger cells • Not yet tested with clinical acquisition protocol; now at 9.4T
Wu (2017)	Compare performance of DKI and DWI for characterization of renal cancer	Clinical 1.5T MR scanner (uMR 550; United Imaging Healthcare, Shanghai,China)	PGSE, b = {0, 300, 600} s/ mm2, TR/TE = 3000/57 ms	In vivo Clear Cell Renal Cell Carcinoma, humans	/	/	***Histology, correlation:*** Nuclear-to-cytoplasm ratio vs.: • ADC_K, r=-0.474, p<0.001 • K, r=0.543, p<0.001 No correlation with cell nuclei count or intracellular fraciton (*cell volume fraction* here).	• In addition to mean kurtosis, also radial and axial kurtosis were measured. These parameters are defined to specifically address direction-dependent K, not useful for determining microstructural properties of whole tumours. • There is a correlation between ADC_K and K and N/C ratio, but no correlation between K and cellularity measures.	• Good intraobserver and interobserver agreement for each parameter • MK is promising for differentiation of tumour grades. • Low b-values only were used in this study, higher clinical feasibility; does give less information though. • Mechanism between relationship of alterations in kurtosis metrics and tumour grades has yet to be determined.

Table 2. Information extraction of the articles that reported an evaluation of the *Intravoxel Incoherent Motion (IVIM)* model – continues on next pages [1/3].

Author (year)	Study goal	MRI scanner	Salient diffusion protocol	Tissue condition on MRI	Extra model specifics	Models compared to	Fitting methods	Correlation to histology	Discussion: value for assessment of microstructural properties	Discussion: Other advantages Other limitations
Fang (2022)	Correlate IVIM parameters to quantitative histological features	3-T MR scanner (DiscoveryMR750w, GE Healthcare, Chicago, IL)	Single diffusion encoding, b = {0,50,100,150,200,400,600,800,1000,1200} s/mm2, TR/TE = 3000/80 ms	In vivo, Rhabdomyosarcoma in mice	/	ADC	Bi-exponential model fitting, using "MADC Software".	ADC vs.: • Cell count, rho=-0.410, p=0.022 • Nuclear fraction, rho=-0.540, p=0.002 • Stroma fraction, rho=0.474, p=0.007 D_t vs.: • Cell count, weak • Nuclear fraction, rho=-0.491, p-0.005 • Stroma fraction, rho=0.421, p=0.018 Cytoplasm fractio and nuclear to cytoplasm ratio did not correlate with any of the metrics. None of the microstructural parameters correlated with D^*. Neither with f, except for stroma fraction (rho =-0.423,p=0.018).	• According to their multiple linear regression, nuclear and stroma fraction independently correlated with D and stroma fraction independently correlated with f. ADC independently correlated with both nuclear fraction and stroma fraction. • They did not find very promising results for the IVIM parameters; few significant correlations and never a correlation if ADC did not already correlate. This suggests that IVIM does not provide useful additional information	• For all four parameters interobserver agreement was good • D showed the best diagnostic ability when comparing with ADC and looking at the AUC of ROC.
Hecht (2017)	Assess relationship between IVIM parameters to histopathology	Clinical 1.5T (Signa HD, 16.0 software, GeneralElectric, Waukesha, WI)	Single diffusion encoding, b = {0,25,50,75,100,150,200,400,600,800} s/mm2, TR/TE = 11000/74 ms	In vivo, Pancreatic adenocarcinoma in humans	/	ADC	***Two fitting methods used:*** • 1. Nonlinear least -square fitting based on LM. • 2. Fixed model method. ***Comparison*** : • All fitting models gave goodness of fit statistic R2>0.7. • Most significant correlations were achieved for both readers using D and f fitted with linear least squares fit and then LM of D*, so data of the first fitting were used.	Mean vessel density, mean vessel density hot spots, mean fibrosis fraction, fraction high fibrosis, tumor cell density were tested for correlation to ADC, f, D_t, D* Summary of findings: • Correlation of f with mean fibrosis fraction (r=0.44, p =0.055) • Correlation of D_t with high fibrosis fraction (r=-0.46, p=0.04) • No correlations between cell density and any of the parameters	• Not very promising results for the IVIM parameters in terms of correlation with microstructural parameters: mean vessel density or cell density.	• The interobserver ICC was excellent for ADC, f, and D_t. For D* it was poor. Intraobserver ICC was excellent for all. • It was found that LM fitting estimates histological parameters better thant he fixed D* method. • The coefficient of variance was greatest for D* and f. This could indicate that D* and f has a large statistical variety; or that they include a lot of information on tissue heterogeneity. Their conclusion is that
Meyer (2021)	Association of IVIM histogram parameters to histopathology	Clinical 3.0 T device (Magnetom Skyra, Siemens, Erlangen, Germany)	Single diffusion encoding, b = {0,50,200,500,100} s/mm2, TR/TE = 6700/58 ms	In vivo, Rectal cancer in humans	Histogram-based metrics of the IVIM-parameters are also computed.	ADC	Simplified IVIM analysis; using Advanced Diffusion Analysis ADA tool.	Cellularity, endothelial area, total vessel area, vessel diameter, vessel count were tested for correlation to *ADC, f, D_t, D** • Endothelial area and f (r=0.63,p=0.006) • Total vessel area and f (r=0.61,p=0.009) • Microvessel count and f (r=0.58,p=0.01) No IVIM parameters showed a significant correlation with cellularity or vessel diameter. No correlation of ADC or D_t with endothelial/vessel area	• A significant correlation is found between f and vascularity parameters • The D_t was not superior compared to ADC *Note:* • *Histogram-based parameters were also computed, however for simplicity they were not taken into account in this review. Only the mean values were considered.*	• Excellent interreaderagreement based on the interreader ICC • There is a lack of standardization in the IVIM acquisition protocol: there are large differences across studies in regard of used b-values. Using more is supposed to be better, sometimes it gives similar results. In addition, using less b-values is more feasible in clinic.
Yin (2018)	Predict tumour cell count and heterogeneity from DWI-data	Clinical 1.5 T MRI (Avanto, Siemens, Erlangen)	Single diffusion encoding, b ={0,50,100,150,200,400,800} s/mm2	In vivo, Lung cancer in humans	/	/	Fit the model using freely available software MITK Diffusion. • Average goodness of fit R2 is 0.91.	Cell count 2D and 3D, tumor cell load in each voxel, cell number whole tumour were tested for correlation to D_t • 2D cell density and D_t (r=-0.84) • 3D cell density and D_t (r=-0.89) • Cell area fraction (intracellular fraction) and D_t (r=-0.87) • Nuclear area fraction and D_t (r=-0.84)	• Strong correlation found between D_t and cell density, cell area fraction and nuclear area fraction • Based on the relationship found between D_t and cell density, the tumour cell count is estimated (see Eq. 8 in the paper). This gives reasonable results. • Only tested this relationship now for one tissue type, should be further tested to test its validity for other tissue types to see if the relationship is generalizable. Should thus be calibrated for different tumour types.	• In this article, a pipeline is developed to infer tumor cell numbers directly from non-invasive DWI data. Focuses therefore a bit as well on an automated image segmentation pipeline for histological data.
Yuan (2016)	Investigate intratumour heterogeneity, correlate MRI measurements with tumour vascularity and cellularity	3T dual-transmit MRI scanner (Achieva,Philips Healthcare, Best, The Netherlands)	Single diffusion encoding, b={0, 50, 100, 200, 450, 600, 1000} s/mm2, TR/TE=1 breathing cycle/60 ms	In vivo, Clear Cell Renal Carcinoma in humans	/	ADC	Custom-written programs in MATLAB	• D_t and cellularity (ρ=-0.316, p=0.039) • No correlation ADC with cellularity (ρ=-0.214,p=0.169) • ADC and D_t were significantly correlated to each other (ρ=0.679,p<0.0001)	• The IVIM-based D_t correlated more with cellularity than ADC: ADC overestimated the tissue diffusion compared to D_t. This supports the advantage of IVIM excluding the perfusion contribution.	/
Winfield (2019)	Correlate quantitative multiparametric MRI values to histopathological findings	1.5 T MAGNETOM Aera MRIscanner (Siemens, Erlangen, Germany	Single diffusion encoding, b={0,25,50,80,150,300,500,800} Δ = 28.4 ms, δ={5.4,12.6,14.6} ms	In vivo, Retroperitoneal sarcoma in humans	/	ADC	Voxel-wise using Markov-chain Monte Carlo method for robust bi-exponential curve-fitting	• D_t and natural logarithm of nuclear-to-stromal ratio (r=-0.45,p=0.005); similar for ADC. Also a dependence on stroma type and grade for both. • No correlation between vessel density and f, D^*	• Correlation between ADC and D_t and high cellularity (high nuclear-to-stromal ratio) points out that the degree of restricted diffusion relates to the density of tumour cells. • IVIM parameters did not contribute additional information to ADC.	• Repeatability of Dt was similar to ADC, but for f and D* poor
Cai (2021)	Investigate the value of IVIM-DWI in differentiating ovarian cancer types	3.0-T MRI scanner(Verio; Siemens Healthineer	Single diffusion encoding, b={0,50,100,150,200,400,600,1000} s/mm2, TR/TE=3300,71 ms	In vivo, Ovarian cancer in rats	/	ADC	Non-linear regression algorithm.	No correlation found between IVIM-parameters and MVD.	• Higher D_t values indicated increased cellularity.	• D_t had good discrimination performance for the tumour types. • Interobserver agreement was acceptable for Dt, and f, but low for D* • f and D* failed to distinguish between tumour types. • No correlation found between f and D* and any DCE-MRI parameters.
Xiao (2020)	Explore correlations of histogram metrics of ADC, IVIM, and DKI with histopathological parameters in sinonasal cancers	3T MR scanner (MagnetomVerio, Siemens Healthineers, Erlangen, Germany)	PGSE, b = {0, 50, 100, 150, 200, 250, 300, 350, 400, 800, 1000} s/mm2, TR/TE = 5200/83 ms	In vivo, Sinonasal cancer in humans	Histogram-based metrics of the IVIM-parameters are also computed.	ADC, **K**	A two-step fitting method	• Histogram metrics from ADC, D_t, f, and ADC_k were significantly correlated with cellular, stromal, nuclear, and cytoplasmic fractions • ADC, f, and ADC_k were also significantly correlated with nuclear-to-cytoplasmic ratio.	• The diffusion coefficients from IVIM and kurtosis were similarly significantly correlated with cellular and tissue composition fractions. • Histogram metrics of ADC_k showed higher correlation coefficients with histopathological features, indicating that ADC_k is a more accurate diffusion parameter • Histogram metrics of f were significantly correlated with cellular and stromal fractions; as high cellular and stromal fraction indicates abundant capillary network and active neoanginesis, this can be explained. • The histogram metrics could not be correlated with histopathologic features on a point-to-point basis *Note:* • *Histogram-based parameters were also computed, however for simplicity they were not taken into account in this review. Only the mean values were considered.*	• Good intrareader agreements achieved >0.825 for all • From all analysed histogram metrics, the histogram metrics obtained from DKI were the most efficient indicators for the characterization of tumor microstructure.

Author (year)	Study goal	MRI scanner	Salient diffusion protocol	Tissue condition on MRI	Extra model specifics	Models compared to	Fitting methods	Correlation to histology	Discussion: value for assessment of microstructural properties	Discussion: Other advantages Other limitations
Wu (2016)	Investigate the value of different diffusion models for monitoring changes in liver cardinoma, and for correlating perfusion parameters to histology	1.5T MRI system (Achieva 1.5T, Philips Health-care, Best, Netherlands)	PGSE, b = {50, 10, 20, 30, 40, 50, 75, 100, 150, 300, 500, 800} s/mm2, TR/TE = 1310/65 ms	In vivo, Rabbit liver VX2 carcinoma	/	ADC, **K, SEM**	"A manufacturer-supplied software (PRIDE DWI Tool, v. 1.5, Philips Healthcare)and workstation (Extended Workspace, Philips Healthcare"	With mean vessel density: • ADC and *f* highest correlation at one timepoint, r2 = 0.307, p = 0.017 and r2 = 0.402 • D* no significant correlation at any timepoint	• At two of three measured timepoint, f was correlated to MV; lower vascularity leads to a lower f. At the first timepoint, no correlation yet; because tumours were still relatively small with sparse vessels. • f was the only parameter that showed high correlation for MVD. • D* did not correlate with MVD and had poor reproducibility.	• ADC, Dt, f, D_{SEM}, ADC_k had excellent reproducibility. D*, σ_{SEM}, K worse. • ADC, f, and K were identified as the most promising parameters for monitoring changes of VX2 carcinoma
Liu (2021)	Exploring differences between IVIM-parameters and ADC for evaluating histology of pancreatic cancer	3.0 Tesla MRI system (Ingenia,Philips Healthcare, Best, Netherlands	PGSE, b = {0, 10, 20, 40, 60, 80, 100, 150, 200, 500} s/mm2, TR/TE = 1261/69 ms	In vivo, Pancreatic ductal adenocarcinoma in humans	/	ADC	"A segment analysis method described previously"	• Significant correlations between fibrosis and D_t (r = -0.35, p = 0.01) and f (r = 0.42, p = 0.01) • Significant correlation between D* and MVD (r = 0.33, p = 0.02)	• Significant correlation between IVIM parameters and tumour fibrosis • D* correlated with MVD	• ADC, Dt, and f had high interreader agreement (075-0.83 ICC), but D* low (0.23). • A high b-value requires an increased TE, which lowers overall SNR; this is especially an issue for pancreatic tissue, as this has short T2 times. • IVIM-parameters had higher sensitivity and diagnostic performance for grading fibrosis in
Song (2016)	Assess IVIM for monitoring early response to chemotherapy in human gastric cancer mouse model	3T MRI (GE Healthcare, Waukesha, WI, United States)	PGSE, b = {0, 10, 15, 20, 25, 30, 60, 75, 100, 200, 400, 800} s/mm2, TR/TE = 2000/99.6 ms	In vivo, Human gastric cancer bearing mice	/	ADC	Levenberg-Marquardt fit	• ADC and Dt were significantly correlated with necrotic fraction (r = 0.720, p < 0.001; r = 0.522, p = 0.006) • No significant correlation among ADC, Dt, and MVD • f and D* significantly correlate with MVD (r = 0.618, p= 0.001; r = 0.538, p = 0.006) • No significant correlation necrotic fraction and f	• D values were positively correlated with intratumoral necrosis and cellular apoptosis • f and D* correlated with MVD	• Lack of standardization in magnitude and number of b-values that ought to be applied • IVIM suffers significantly from variations in SNR, prone to generate measurement errors when b<100s/mm2
Lee (2014)	Test correlation between IVIM-parameters and histological microvessel density	3.0-T MRI imagingsystem (Magnetom Trio; Siemens Medical Solutions,Erlangen, Germany)	PGSE, b = {0, 50, 100, 300, 500, 700, 1000} s/mm2, TR/TE = 3300/104 ms	In vivo, Human colorectal cancer implanted in mice	/	/	"Using in-house software written by MATLAB"	• D* and f significantly correlated with MVD (r=0.782,p<0.001 and r=0.749,p<0.001) • No significant correlation between D_t and MVD	• D* and f are correlated with histological MVD	• CV of D* and f were high across tumours in spite of them having the same malignant histology; probably due to variation in MVD as well
Mayer (2021)	Compare IVIM and CT perfusion to assess perfusion of pancreatic tumours	1.5 T scanner (Magnetom Avanto, Siemens Medical Solutions)	PGSE, b = {0, 50, 100,150, 200, 300, 400, 600, 800} s/mm2, TR/TE = 2200/58 ms	In vivo, Pancreatic adenocarcinoma in humans	/	/	A two-step fitting method	• f correlated significantly with MVD and MVA (ρ = 0.770 and ρ = 0.818, both p < 0.05)	• No significant rank correlation between D* and MVD or MVA, although D* is supposed to be a flow-related parameter; possible explanation is that D* is found to be much less stable than f • Dt did not correlate with any histological microvessel parameters, as is expected	• The applicability of DW IVIM-MRI seems comparable to the applicability of CT perfusion for assesment of tumour tissue perfusion
Li (2018)	Compare IVIM and CT perfusion to assess microvessel density	Achieva 1.5 T (PhilipsHealthcare, Best, Netherlands)	PGSE, b = {0, 10, 20,30, 40, 50, 75, 100, 150, 300, 500, 800} s/mm2, TR/TE = 2660/80 ms	In vivo, Rabbit liver VX2 tumours	/	ADC	"a software program (PRIDE DWI Tool, version 1.5, Philips Healthcare)"	• D_t correlated significantly with MVD (r = 0.509, p = 0.044) • No significant correlation between f, D*, ADC and MVD	• f had no correlation with MVD; implying a potential mismatch between f and angiogenesis due to a series of mentioned mechanisms. • D* showed no correlation between MVD as well, implying that D* value cannot be considered as reflection of microcirculatory perfusion; for which a number of possible explanations are mentioned. • Dt was the only parameter that did correlate significantly with MVD, which in theory does not make sense; for this various reasons are mentioned as well	• All parameters had excellent reproducibility
Mori (2022)	Evaluate correlation of ADC and IVIM-diffusion kurtosis model parameters with histological parameters	3-T system (Intera Achieva dStream, Philips Healthcare; Best, The Netherlands)	PGSE, b = {0,50, 100, 300, 550, 850, 1000} s/mm2, TR/TE = 4987/74 ms	In vivo, Breast cancer in humans	Uses a combined *IVIM-DK model*, computes in addition to perfusion fraction *f*, pseudo-diffusion D*, true diffusion D_t, also the kurtosis *K*.	ADC	A two-step fitting method	Tested for correlation with area ratio of cancer cells, cancer cell nuclei and cytyplasm, interstitium, lympocyte, microvesseels, size of cancer cells and cancer nuclei, and entropy. • K significantly correlated with area of cancer cell nuclei (r = 0.53, p = 0.00079); ADC correlated significantly with area ratio of the interstitium (r = 0.53, p =0.00082) and with entropy (r = -0.58, p = 0.00019) • No other correlations found	• The difference in results between the ADC and D_t might be attributable to the complexity of the IVIM-DK imaging model, rendering it more susceptible to MRI noise • K correlated significantly with the area ratio of cancer cell nuclei; kurtosis becomes larger with larger nucleus and more tissue heterogeneity	• Interobserver agreement was excellent ICCs of all computed parameters were >0.817. • Further studies comparing kurtosis obtained from data acquired with higher b-values (b >1000 s/mm2) with quantitative histological parameters are needed in the future; in this study highest b = 1000.
Yang (2017)	To investigate effectiveness of IVIM-parameters in the assessment of therapeutic efficacy of sorafenib in HCC xenograft model	1.5T MR scanner (Magnetom Aera; Siemens Healthcare, Erlangen, Germany)	PGSE, b = {0, 25, 50, 80, 150, 300, 500, 800} s/mm2, TR/TE, 5000/64 ms	In vivo, Hepatocellular carcinoma in mice	/	ADC	"an in-house developed software based on MatLab (MathWorks, Natick, MA), where the fitting algorithm was the same with that implemented in the Siemens IVIM prototype software"	*Treated group:* • ADC, Dt, f had significant correlation with necrotic fraction (r = 0.811, p < 0.001; r = 0.838, p < 0.001; r = –0.095, p = 0.691 respectively) • No correlation D* and nectrotic fraction • No correlation between ADC, IVIM-parameters and MVD *Control group:* • Only f had significant correlation with MVD (r= 0.568, p = 0.009) • No correlation any of the other IVIM-parameters and histological parameters	• Moderate correlation was found between f and MVD in the control group, but no correlation between ADC, Dt and NF, while for the treatment group this was the case. An explanation of this is mentioned in the article.	• Intra- and interobserver ICCs were observed for all parameters • IVIM-parameters can be used to detect sequential changes in diffusion and perfusion under sorafenib treatment • D* has inherent poor SNR and low precision • IVIM cannot differentiate between intra- and extracellular water molecule diffusion • ADC, Dt, and f obtained by IVIM may be useful as noninvasive biomarkers for prediction of HCC responses to sorafenib
Hompland (2018)	Develop a method to visualize hypoxia in prostate cancer	a 1.5 T General Electric Discovery 450 magnet with a 32 channel phased array coil (GE Medical Systems)	PGSE, b = {0, 100, 200, 300, 400, 500, 600, 700, 800, 900, 1000} s/mm2, TR/TE = 3000/59.4 ms	In vivo, prostate cancer in humans	/	/	A two step fitting algorithm	• Significant correlation between D_t and cellularity (R2 = 0.46, p < 0.0001) • Significant correlation between f and blood vessel density (R2 = 0.44, p < 0.0001)	• Their findings support that D_t and *f* can be used as measures of CD and BVD respectively, in prostate tumors.	
Tao (2023)	To investigate the correlation between IVIM parameters and microvessel architecture in an orthotopic murine Model of rhabdomyosarcoma.	3.0 T Discovery750w MRI system (GE Healthcare) equipped with a human Four-channel wrist coil	Fast spin-echo DWI with periodically rotated overlapping parallel lines with enhanced reconstruction (FSE-PROP-DWI). B-values: 0, 50, 100, 150, 200, 400, 600, 800, 1000, and 2000 s/mm2	In vivo, anesthesised mice, imaged in tumours that developed in the muscle, model of Rhabdomyosarcoma	/		MADC software bi-exponential fitting	• Significant correlation between Vasculogenic Mimicry (VM) And Dt (r = -0.569, p = 0.008) • Significant correlation between Microvessel Density (MVD) and D* (r=0.708, p=0.001) • Significant correlation between Pericyte Coverage Index (PCI) and D* (r=0.716, p=0.001) • Significant correlation between MVD and f (r=0.517, p=0.026) • Significant correlation between MVD and the product fxD* (r=0.509, p=0.026) • Significant correlation between PCI and	• Their findings suggest that IVIM parameters can be used as proxys For microvessel architecture	• Results may not generalise to humans in vivo, as the characteristics of the Vasculature in tumours grown from injections of culutured cells may be considerably Different from the characteristics of vasculature in vivo in humans • Relatively small sample size • Higher resolution with small animal systems should have been used

Table 2. Information extraction of the articles that reported an evaluation of the *Intravoxel Incoherent Motion (IVIM)* model – final page [3/3].

Author (year)	Study goal	MRI scanner	Salient diffusion protocol	Tissue condition on MRI	Extra model specifics	Models compared to	Fitting methods	Correlation to histology	Discussion: value for assessment of microstructural properties	Discussion: Other advantages Other limitations
Zhang (2023)	To distinguish the histological subtypes of malignant pleural mesothelioma (MPM) and characterize the development of related histological Features.	3.0 T MR scanner (Achieva 3.0T Tx, Philips) using a dedicated mouse coil with an inner diameter of 50 mm (CG-MUC43-H300-AP, Chenguang Medical Technologies Co., LTD, Shanghai, China).	Spin echo PGSE EPI With TR=710ms, TE=63ms, b=0, 10, 20, 30, 50, 100, 200, 400, 600, 800, 1000, 1200 s/mm2, NEX=6	In vivo, anesthesised mice, malignant pleural Mesothelioma xenografts	/	T1, T2, ADC mapping	Generic bi-exponential fitting	• Significant correlation between D* and NF (r=0.327,p=0.016) and between D* and MVD (r=0.342,p=0.011) in biphasic MSTO-211H cells • Significant correlation between f and necrotic fraction (NF), but with opposite signs in epithelioid NCI-H226 (r=0.404,p=0.002) and biphasic MSTO-211H cells (r=-0.507,p=0.001) • Significant correlation between f and Microvessel Density (MVD), but with opposite signs in epithelioid NCI-H226 (r=0.437,p=0.001) and biphasic MSTO-211H cells (r=-0.554,p<0.001) • Significant correlation between f and tumour volume (TV), but with opposite signs in epithelioid NCI-H226 (r=0.445,p=0.004) and biphasic MSTO-211H cells (r=-0.560,p=0.009) • Significant correlation between D and tumour	• IVIM metrics sensitive to histological properties of the microvasclature and cell density (e.g., necrosis), but high variability in the correlation sign is Seen across cancer cell groups	• Imaging performed with a clinical 3T system on alive animals, which gives confidence on the clinical feasibility of the mapping • Results are highly variable depending on the cancer cell type and require confirmation
Xie (2022)	To evaluate liver perfusion changes and their effect on liver regeneration (LR) after partial hepatectomy (PH) using intravoxel incoherent motion (IVIM) and T2* mapping To a rat model	3T MR scanner (MEGNETOM Prisma, Siemens) with an eight-channel rat-specific coil	Single-shot PGSE EPI; TR/TE 2300/74 ms; FOV 120x98 mm2 ; 12 slices, 3mm-thick; 120x98 matrix; reconstructed voxel size 0.5x0.5x3 mm3; acceleration factor4; b = 0, 10, 20, 30, 50, 75, 100, 300, 500, 800 s/mm2 ; 7 min 12 s	In vivo, anesthesised Sprague-Dawley Rats, Imaged after hepatectomy	/	DCE, T2*	Generic bi-exponential fitting	D* and f correlated with hepatocyte Ki-67 indices (r = _x0001_0.588 to _x0001_0.915; p < .05) And hepatocyte diameter (r = _x0001_0.555 to _x0001_0.792; p < .05).	• IVIM metrics sensitive to histological properties related to liver regrowth in hepatectomy, a relevant treatment option in several types of cancers (e.g., metastasis resection)	• Histology was not performed on the mice that were imaged with MRI

Table 3. Information extraction of the articles that reported an evaluation of the *Vascular, Extracellular, and Restricted Diffusion for Cytometry in Tumors* model – continues on the next page [1/2].

Author (year)	Study goal	MRI scanner	Salient diffusion protocol	Tissue condition on MRI	Extra model specifics	Models compared to	Fitting characteristics, including compartment models	Comparisons with ground truth data	Discussion: value for assessment of microstructural properties	Discussion: Other advantages Other limitations
Bonet-Carne (2019)	Linearize VERDICT to improve fitting speed; comparison VERDICT vs. VERDICT-AMICO	3 T scanner (Achieva, Philips Healthcare, Best, Netherlands)	PGSE, b = {90, 500, 1500, 2000, 3000} s/mm, Δ/δ = {23.8/3.9}, {31.3/11.4}, {43.8/23.9}, {38.8/18.9} ms, TR/TE = {2482/50}, {2482/65}, {2482/90}, {3945/71}, {3349/80} ms	In vivo, Prostate cancer in humans	For **conventional VERDICT:** • Computed: f_{ic}, f_{ees}, R, f_{vasc} = 1 - f_{ic} - f_{ees} • Fixed at set value: d_{ic}, d_{ees}, d_{vasc} For **VERDICT-AMICO**: • The same as for VERDICT, except that d_{EES} is also estimated as extra paremeter, not fixed anymore	VERDICT compared to VERDICT-AMICO	*Two fitting procedures compared:* • 1. Accelerated microstructure imaging via convex optimization (AMICO) framework. • 2. Original non-linear VERDICT fitting using Camino (Matlab); iterative optimization using LM algorithm.	***Simulation study:*** • At typical noise level for clinical acquisitions, VERDICT-AMICO has lower absolute error than VERDICT • For f_{ic}, AMICO makes slightly larger errors than VERDICT ***Clinical study:*** • Similar estimates VERDICT and VERDICT-AMICO for f_{ic} and f_{EES} • Significantly higher estimates f_{ic} and R for AMICO, f_{EES} significantly lower for AMICO • Results of both are within biophysically plausible range • Precision of fit better for AMICO	• No validation with clinical histological data done in this study; only correlation between results of both methods • They did both provide clinically plausible values based on the used dictionary. • VERDICT-AMICO had a higher precision. • Parametric maps for AMICO appear less noisy than original VERDICT, for the rest similar parametric maps. • VERDICT tends to overestimate f_{vasc} in comparison with normal histology; this effect decreases if we unfix d_{EES}	• Most parameters are repeatable with high correlation coefficients, AMICO had the highest repeatability • AMICO much faster; allows parameters to be computed directly during the scan. This increases clinical feasibility. VERDICT-AMICO reduces processing time by more than three orders of magnitude (6.55 s/voxel --> 1.78 ms/voxel). • AMICO fitting depends on dictionary values selections; the regularization has to be set empirically. Choice of these has to be validated based on histology. • AMICO inherits limitations of original VERDICT, which is that it does not account for permeability between different compartments or for T2 heterogeneity wihtin the same voxel
Bailey (2019)	Clinical validation of VERDICT-parameters, and to assess influence of a 3D printed patient specific mould. In addition, comparison between fresh and fixed samples from the prostate.	• For in vivo scanning on which the mould is based: 3T MRI (Philips Achieva, Best, The Netherlands) • For ex vivo DW-MRI data acquisition: 9.4 T (Agilent Inc., Santa Clara, CA, USA)	PGSE, different protocols for fresh and fixed imaging. TR = 2000 ms Δ/δ/TE = {10/3/18} ms • *Fresh*: b = {9, 148, 334, 594, 752} s/mm2 • *Fixed*: b = {9, 84, 232, 455, 752, 928} s/mm2 Δ/δ/TE = {30/3/46} ms • *Fresh:* b = {30, 120, 478, 1077} s/mm2 • *Fixed:* b = {30, 269, 748, 1465} s/mm2 Δ/δ/TE = {30/10/46} ms • *Fresh*: b = {306, 1222, 2750, 7638, 14971} s/mm2 • *Fixed:* b = {306, 2750, 7638, 14971} s/mm2 Δ/δ/TE = {50/3/66} ms • *Fresh:* b = {51, 202, 808} s/mm2 • *Fixed:* b = {51, 455, 1263) s/mm2 Δ/δ/TE = {50/10/66} ms • *Fresh:* b = {535, 2139, 8555} s/mm2 • *Fixed:* b = {535, 2139, 8555} s/mm2 Δ/δ/TE = {70/3/86} ms	Ex vivo, both fresh and formalin fixed, Resected prostate cancer in humans	Model parameters: • Computed: f_{ic}, f_{ees}, R, f_{vasc} = 1 - f_{ic} - f_{ees} • Fixed at set value: d_{ic}	ADC	Model fitting using **LM algorithm.** First fitting with different compartment models: • Isotropic balls; unrestricted diffusion • Tensor, anisotropic • Sphere, isotropically restricted • Watson; group of sticks Several models tested: • 1 compartment: conventional DTI (tensor) • 2 compartments: bi-exponential (ball-ball) • 2 compartments: with spherical restricted compartment = VERDICT, but without vascular compartment (the third) - Ball or sphere functions as the intracellular space, with a fixed d_{ic} Data were fitted voxelwise with max-likelihood approach. Models compared with **Akaike Information Criteria (AIC).** Tensor-sphere model had the lowest AIC in most voxels: • This one used in the rest of the comparisons.	***Histology, qualitative comparison:*** • Regions of high f_{ic} and low ADC correspond to regions of high cell fraction on histology • Regions of low f_{ic} and high ADC are dominated by lumen space or low cellularity stroma • In regions with lots of lumen space, *R* was poorly determined; tended towards the largest values allowed by the fitting. It had a high uncertainty	• f_{ic} indicates whether a region belongs to tumour or lumen space - high vs. low. • *R* varies little in this study for tumour and non tumour; in some other studies this is different but in those they allow d_{ic} to vary. • R does not provide useful information here; does not fit well for lots of lumen space. • No quantitative voxelwise comparison was done with histology, due to alack of registration accuracy • VERDICT assumes one single cell size within each voxels, however cells have a distribution of sizes; not captured by VERDICT.	• Tensor-sphere model best describes diffusion data in prostates, which agrees with previous studies. Single-compartment models fail when data includes high b-values or varying diffusion times. • A decrease is observed in extracellular diffusivity and an increase in intracellular fraction after fixation, which is caussed by water loss from the extracellular space during fixation. Fixation influences water content and diffusivity, but neither model selection nor model parameters associatated with tissue structure (such as R) are greatly affected by the fixation. They conclude that fixation does not seriously affect estimates of VERDICT-based microstructural parameters and that correction for fixation is not necessary. • T2 is modelled as mono-exponential.
Duchêne (2020)	Presentation of a double diffusion encoding MRI sequence on a clinical scanner to analyze microstructure and microvasculature	3T Achieva (PhilipsTM, Best, The Netherlands)	Double Diffusion Encoding (DDE) with single shot double spin-echo echo-planar sequence, different protocol per specimen: • *DDE on asparagus* : b = {0, 0.2, 0.87, 2.0, 3.5, 5.3} ms/μm2, TE/TR = 3000/164 ms, relative angle ψ = {0, 45, 90, 135, 180}, {0, 180}, Δ/δ = 60/12 ms • *DDE on tumour:* b = {0, 0.01, 0.39, 0.89, 1.58, 2.46, 3.55} ms/μm2, TR/TE = 2000/108 ms, relative angle ψ ={0, 180}, Δ/δ = 32/13 ms In addition *conventional DWI on tumour:* • b = {0, 1} ms/μm2, Δ/δ = 27/8 ms, TR/TE = 2000/55 ms	• Biological phantom: asparaguses' stems • In vivo, 2 allografts of rhabdomyosarcoma in rats	Model parameters: • Computed: f_{ic}, f_{ees}, R, f_{vasc}, d_{EES}, mean flow velocity *v*	DDE with only two ψ (= 0, 180) (called P-AP) compared to DDE with more angles	AMICO-fitting was used for VERDICT. Compartment shapes: • Intracellular as spheres • Vascular as sticks • EES as hindered diffusion environments Model fitting yielded a signal that closely matched to the measured signal (for asparagus).	***Histology quantitative comparison:*** • f_{ic}, f_{vasc}, f_{EES}, d_{EES} were all consistent with necrotic and viable areas • f_{ic} and cell size *R* were significantly decreased in necrotic ROIs compared with viable tissue. • Feret diameter is used for the histology, which is a measure for cell size. This correlated sgnificantly with the computed *R* (*r* = 0.59, 0.68). • Stained area fraction is used for the histology, which is a measure for intracellular fraction. This strongly correlated significantly with f_{ic} (r = 0.84, 0.90).	• Histology was consistent with DDE results; good f_{ic} and R estimation with high correlation. • R and v are sensitive to noise. • v exhibits a poor differentiation between viable and necrotic tissues. • Vascular component behaviour depends on Δ, so the use of a single Δ could be an advantage of DDE over TDD. Both behaviours of vascularity would then give a constant contribution to MR signal. DDE is not meant to not provide extra information than TDD, but it does offer a more accurate model.	• Implementation of DDE sequence on clinical scanner is challenging; limited maximum gradient strength and scan time should be acceptable; however in this work it is attempted to achieve on a clinical scanner. Results were only weakly affected by using relative angle ψ = 0, 180 instead of multiple angles. This increases clinical feasibility, • The reason for using different Δ is to increase sensitivity to cell sizes as the relationship between Δ and the mean squared displacement of water molecules depends on the size of restricting geometries: this effect is referred to in the paper as *RD*. The proposed DDE sequence does not rely on TDD, but rather on the influence of *RD* at a constant diffusion time. • In DDE, two diffusion encoding gradients are consecutively applied with 2 different orientations, separated by a relative angle ψ. For adjacent gradient pairs; molecular displacements during encodings are correlated, resulting in a high sensitivity to *RD*. DDE has therefore been proposed to quantify cell sizes • Besides RD, DDE is shown to be sensitive to ballistic flow occuring in vascular network.
Panagiotaki (2014)	First introduction of VERDICT! To quantify and map histologic features of tumors	9.4T scanner (Agilent)	PGSE, Δ/δ = {{10, 20, 30, 40}/3}, {30, 40}/10}} ms, G = [40-400] mT/m in 10 steps for δ = 3 ms, G = {40, 80, 120} mT/m for δ = 10 ms. TE = minimum for each Δ/δ combination, TR = chosen to minimize gradient heating effects.	In vivo, Colorectal adenocarcinomal xenografts in mice	Model parameters: • Computed: f_{ic}, f_{EES}, R, f_{vasc}, d_{vasc} the main orientations of the anisotropic diffusion tensor that represents the vascular component θ, φ. • Fixed at set value: d_{ic} = d_{EES}	ADC, **IVIM**	Compartment shapes: • Intracellular as spheres • EES as isotropic • Vascular as anisotropic Iterative optimization procedure for model fitting (non-linear optimization via LM algorithm); first fitting over all voxels within the tumor ROI averaged, then fitting for each voxel. Uses contrained model parameters; to ensure biophysically meaningful values. • VERDICT manages to get a good fit to	***Histology, absolute value comparison:*** • Because of shrinkage during prepration ex-vivo; cell sizes *R* measured on histologic sections were on average smaller than those computed by VERDICT. • The f_{ic} got the greatest value ascribed from all fractions. • f_{vasc} and d_{vasc} were significantly different between tumour types.	• VERDICT estimated biophysically realistic values for all parameters; they were larger than those measured in histology but that is explainable by the shrinkage. All parameters were broadly consistent with histology and arterial spin labelling MRI. • VERDICT found a significant difference for each of the parameters between two cell lines of tumours; while ADC and IVIM did not. • VERDICT had a much better fit to the data than ADC/IVIM • Cells are assumed to be perfectly spherical; if they are not, their radius R index was overestimated.	• The key advantage of VERDICT that make it better fitting than ADC/IVIM is the possibility for inclusion of signal anisotropy and restricted diffusion (via different compartment shape models). • Clinical application is difficult due to limited gradient strength available on clinical MR systems • No incorporation of exchange between compartments in VERDICT • Specific used compartment models require tuning depending on the shape and arrangement of cellular structures. This requires more study on histology to determine which models fit certain tissues best.
Johnston (2019)	Evaluate performance of parameter f_ic and compare with ADC	3.0-T MRI system (Achieva; Philips, Best, the Netherlands)	PGSE, b = {90, 500, 1500, 2000, 3000} s/mm2 with respectively Δ/δ = {{23.8/3.9}, {31.3/11.4}, {43.8/23.9}, {34.3/14.4}, {38.8/18.9}} ms, and TR/TE = {{2482/50}, {2482/65}, {2482/90}, {3945/71}, {3945/80}} ms	In vivo, Prostate cancer in humans	Model parameters: • Computed: f_{ic}, f_{EES}, f_{vasc}	ADC	AMICO-fitting was used for VERDICT.	***Histological grade differentiation:*** • f_{ic} for Gleason grade 3+4 was significantly higher than for benign/Gleason grade 3+3, while for ADC they were similar • f_{EES} and f_{vasc} did not show significant differences between those groups	• No difference in image quality for the parametric map based on f_{ic} and ADC • ROC AUC was higher for f_{ic} than ADC, for distinguishing Gleason tumour grades; but for f_{EES} and f_{vasc} it was lower	• Repeatability was excellent for the VERDICT parameters, ICC was >0.87

Table 3. Information extraction of the articles that reported an evaluation of the *Vascular, Extracellular, and Restricted Diffusion for Cytometry in Tumors (VERDICT)* model – final page [2/2].

Author (year)	Study goal	MRI scanner	Salient diffusion protocol	Tissue condition on MRI	Extra model specifics	Models compared to	Fitting characteristics, including compartment models	Comparisons with ground truth data	Discussion: value for assessment of microstructural properties	Discussion: Other advantages Other limitations
Bailey (2018)	Characterize microstructure using different models	1.5T (MAGNETOM Avanto, Siemens Healthcare, Erlangen, Germany)	PGSE, b = {1000, 2000, 3000, 2500, 1500, 800, 400, 200, 100, 500, 800, 800, 500} s/mm2 with respectively Δ/δ = {33.8/24.8, 45.6/33.2, 52.4/40, 52.6/40.2, 40.6/28.2, 31.4/19, 26.2/13.4, 22.8/10, 20.2/7.4, 60/24.8, 60/24.8, 50/24.8, 50/24.8} ms and TE = {77.2, 94, 111.6, 108, 84, 67.6, 56.4, 49.6, 44.4, 100.4, 100.4, 90, 90} ms, TR = 3000 ms	In vivo, Prostate cancer in humans	Model parameters: • Computed: R, f_{ic}, f_{EES}, f_{vasc} • Fixed at set value: $d_{EES} = d_{ic}$, d_{vasc}	• ADC: only ball • **IVIM**: two compartments, vascular using ball, extracellular using ball as well • **K**	Three VERDICT options modeled for *vasc-EES-ic* : • Astrosticks-Ball-Sphere (ABS) • Ball-Ball-Sphere (BBS) • Ball-Astrosticks-Sphere (BAS) Models compared using AIC. BAS performed significantly worse than ABS and BBS. Kurtosis, ABS and BBS performed similarly. BBS was chosen for the rest of the analysis.	• VERDICT model parameters fell within plausible biological ranges ***Model correlations:*** • The correlation was tested between ADC, K and VERDICT parameters: - ADC, ADC_{ic}, correlated significanlty with d_{ic}, f_{ic}, f_{vasc}. - K correlated most strongly with f_{ic}, and more weakly with d_{ic}, R - R did not correlate significanty with either ADC, or ADC_{ic}	• Kurtosis and VERDICT models captured the signal at high b-values well. In some voxel the complex VERDICT model was required to fully capture the signal; particularly variations with diffusion time. • These voxels have largest f_{ic} in parameter maps, indicating that VERDICT might work better in regions with large f_{ic} contribution; they have higher SNR and strong time-dependence.	• Astrosticks is not a good descriptor for extracellular space; BAS did not perform well • BBS and ABS were similar; they only vary shape of vascular component, due to low vascular fraction might not matter that much • Kurtosis is better able to capture non-Gaussian behaviour, with a high b. Where kurtosis best explained data, the VERDICT fit was similar, but this is a more complicated mdoel. • Where VERDICT better explained data, there was a greater diffusion time dependence: this is captured by the restricted sphere component in VERDICT.
Panagiotaki (2015)	Demonstrate feasibility of VERDICT for prostate cancer in clinical setting	Philips Achieva 3-T MRI scanner	PGSE, b = {100, 200, 400, 800, 1000, 1500, 2000, 2500, 3000} s/mm2, with respectively Δ/δ = {{26.6/8.5}, {29.4/11.3}, {31.6/13.5}, {30.7/12.6}, {28.1/10.0}, {25.7/7.6}, {23.7/5.6}, {22.2/4.1}, {21.2/3.1}} ms, TR/TE = {{2000/55}, {2305/60}, {2731/65}, {2517/63}, {2033/58}, {2000/53}, {2000/49}, {2000/46}, {2000/44}} ms	In vivo, Prostate cancer in humans	Model parameters: • Computed: R, f_{ic}, f_{EES}, f_{vasc} = 1 - f_{ic} - f_{EES} • Fixed at set values: d_{vasc}, d_{ic}, d_{EES} with $d_{EES} = d_{ic}$	ADC, **IVIM, K**	AIC computed to compare the models: • K and VERDICT perform similarly, so slight preference for K because this has only 2 parameters, VERDICT has 3. • In cancerous areas however, VERDICT shows smaller AIC than K; indicating that the extra complexity of the model is necessary to explain the data	***Comparison tumour vs. benign:*** • Differences between tumour / benign regions tested; VERDICT volume fractions are all significantly different. • No significant change in VERDICT-based cell size R between tumour / benign	• VERDICT-based cellularity computation clearly indicates tumour regions from benign regions • VERDICT assigns the differences to specific biophysical or histological factors; while ADC and K do not; they use unspecific metrics. • VERDICT volume fractions of IC and vascular component are increased for cancer, which corresponds to histological assesment	• Lower mean squared error for the VERDICT fit than for ADC or IVIM • Kurtosis fits closely, similar to VERDICT • Correlation tested between ADC, K, IVIM and VERDICT parameters: - Negative correlation between {ADC, D_k} and f_{ic} - Positive correlation between {ADC, D_k} and f_{EES}, f_{vasc}, - *K* strong positive correlation with f_{ic}, negative with f_{EES}
Palombo 2023	Extend VERDICT to include for relaxation properties	Philips Achieva 3-T MRI scanner	PGSE with ive combinations (b; δ; Δ; TE; TR) of b-values b (in s/mm 2), gradient duration δ, separation Δ, echo time TE and repetition time TR (in ms): respectively, (90; 3.9; 23.8; 50; 2482); (500; 11.4; 31.3; 65; 2482); (1500; 23.9; 43.8; 90; 2482); (2000; 14.4; 34.4; 71; 3945); (3000; 18.9; 38.8; 80; 3349), in three orthogonal directions using a cardiac coil.	In vivo, Prostate cancer in humans	Model parameters: • Computed: T2vasc/EES, T2ic, T1, R, f_{ic}, f_{EES}, f_{vasc} = 1 - f_{ic} - f_{EES} • Fixed at set values: d_{vasc}, d_{ic}	Classic VERDICT	Fitting via Deep Neural Networks or relaxation-VERDICT (rVERDICT), which is compared to classical VERDICT fitting	**Comparison tumour vs. benign:** • Differences between tumour / benign regions tested, with rVERDICT showing stronger effect sizes than VERDICT **MRI-histology correlation:** ANOVA analysis shows that rVERDICT fic is associated to Glason grade, improving results from classical VERDICT. RVERDICT discriminates 3+4 vs >=4+3 (p=0.040), unlike classical VERDICT	• The implementation improves the histological fidelity of VERDICT intra-cellular fraction	• The implementation improves the reproducibility of VERDICT as it takes into account changes in TE • Moreover, it provides new potential biomarkers of compartment-wise T2

Table 4. Information extraction of the articles that reported an evaluation of the *Imaging Microstructural Parameters Using Limited Spectrally Edited Diffusion (IMPULSED)* model – continues on the next page [1/2].

Author (year)	Study goal	MRI scanner	Salient diffusion protocol	Tissue condition on MRI	Extra model specifics	Models compared to	Fitting characteristics, including compartment models	Comparisons with ground truth data	Discussion: value for assessment of microstructural properties	Discussion: Other advantages Other limitations
Jiang, Xu et al. (2020)	Noninvasive method testing for in vivo mapping hepatocyte size	• *Preclinical*: Varian/Agilent DirectDrive horizontal 4.7T magnet (Agilent, Palo Alto, CA) • *Clinical*: Philips Achieva 3T scanner (Amsterdam, Netherlands)	*Preclinical:* TR/TE = 3000/70 ms • PGSE, Δ = {10, 40} ms, δ = 4 ms, b = {0, 300, 500, 750, 1000} s/mm2 • OGSE, *f* = {66, 100} Hz with respectively Δ/δ = {(20/15), (15/10)} ms and b = {{0, 300, 500, 750, 1000}, {0, 300, 450, 600}} s/mm2. *Clinical:* TR/TE = 4500/110 ms • PGSE, Δ/δ = 74/12 ms, b = {0, 250, 500, 750, 1000} s/mm2 • OGSE, TR/TE = 4500/110 ms, *f* = {25, 50} Hz with Δ/δ = {52/40} ms and respectively b = {{0, 250, 500, 750, 1000}, {0, 100, 200, 300}} s/mm2. Resulting diffusion times t_{diff} ranged	• In vivo, Liver of three mice and three rats • In vivo, Liver of humans	Model parameters: • Computed: cell size diameter *d* f_{ic}, d_{ec} • Fixed to a set value: d_{ic}	/	This version of IMPULSED assumes three compartments: • **1. Perfusion (IVIM)** is ignored in other applications of IMPULSED. With decreasing t_{diff}, IVIM effects decrease as well. The effect of perfusion is removed by implementing an approach from Taouli and Koh: the model is fit on IVIM-free signals. • **2. Intracellular component**: restricted diffusion in hollow spheres, depend on cell size diameter *d*, d_{ic} • **3. Extracellular component:** d_{ec} is approximately linearly related to the inverse of the diffusion time t_{diff}. The used frequency range in this study shows minor variation in d_{ec} and therefore is modelled as a constant. Nonlinear, constrained algorithm to fit, based on a Bayesian Probability Based grid search method. If voxels did not show a significant t_{diff} dependence of ADC; they were excluded (< 5%).	***Animal histology:*** • Histograms of MRI-derived and histology derived hepatocyte sizes from rats are similar. • f_{ic} has a lower mean value and wider distribution from MRI than histology. • Fitted *d* have high precision RSD < 10%. • IMPULSED-derived *d* show good agreement, while IMPULSED-derived f_{ic} are lower than histological ***Humans:*** • Hepatocyte size estimates are within human plausible ranges. • *d* again has lowest RSD (~7-9%), highest precision	• Estimates for hepatocyte size are plausible in humans and animals, and similar to histology in animals • Due to challenges in co-registration; it was not possible to perform a voxel-wise correlation between histology and MRI. No strict comparison possible, only indication that estimates are reasonable is possible. • Precision was tested for the parameters, which was good, but it was not possible to assess systematic bias errors. • f_{ic} is underestimated in comparison with histology • Difficult to obtain true values of d_{ic} and d_{ec}, variations of 15-30% are observed; can be decreased by increasing SNR - which typically requires longer scanning. • Fitted cell size represents an average per voxel, lowers sensitivity for assessing changes in certain types of cells; cell-distribution would be better.	• Since this is a more complicated signal model, an increased SNR is required for stable fitting. • Only healthy subjects studied, no oncological cases tested yet. However, this application is still relevant for oncology. • In this study, the effect of pseudo-diffusion is removed. However, including presudo-diffusion coefficient as an independent variable in the fitting model might lead to an even more accurate quantification. This would however increase scanning time. • Transcytolemmal water exchange is ignored, which explains the underestimation of f_{ic}.
Xu (2020)	Present clinically feasible IMPULSED method	• *In vitro:* Varian/Agilent 4.7T MRI spectrometer (Agilent Technologies, Santa Clara, CA) • *Animals:* 4.7T Varian/Agilent horizontal small animal scanner (Agilent Technologies) • *Humans:* Philips Achieva 3T scanner	TR/TE = 4500/104 ms • PGSE, Δ/δ = 74/12 ms, b = {0, 250, 500, 750, 1000, 1400, 1800} s/mm2 • OGSE, *f* = {25, 50} Hz, Δ/δ = {51.4/40/9} ms, with b = {{0, 250, 500, 750, 1000}, {0, 100, 200, 300} s/mm2. Resulting diffusion times t_{diff} ranged from [5-54] ms.	• In vitro cells • In vivo breast cancer xenografts in mice • In vivo breast cancer in humans	Cell size diameter is here a volume weighted mean *d* - see equation in paper. Computed: f_{ic}, d_{ec} Fitting precision decreases if d_{ic} is free, so it was fixed at a set value.	PGSE-only based ADC	Two compartments: • 1. Intracellular diffusion modelled by spheres. • 2. Extracellular diffusion modelled by constant d_{ec}. Maximization of log likelihood with Rician noise, voxel wise basis fitting.	***Simulation study:*** • IMPULSED can measure cell size *d* and f_{ic} even with low SNR; but the d_{ec} is not reliable with low SNRs. ***In vitro study:*** • IMPULSED derived cell size shows a strong correlation with measured histology (r = 0.92, p<0.001). ***In vivo mice:*** • Good agreement of mice in vivo as well, but slightly underestimates *d*.	• f_{ic} is underestimated; however other studies found that f_{ic} correlates well with ground-truth cell density in simulations. It might be a good indicator, but absolute accuracy is uncertain. • *d* can on the other hand be reliably estimated. Estimation of cell size distribution would be a useful extension of the model.	• This application of IMPULSED does not use cosine oscillating diffusion gradients but *cosine modulated oscillating trapezoidal diffusion gradients*, which makes it more clinically feasible. • The most significant ADC change occurs between t_{diff} of 5-30 ms; which is the range used in IMPULSED and ensures that it has a good sensitivity to cellular properties. - This IMPULSED method performance is not limited by the standard clinical parameters; so feasible for the clinic • Difference VERDICT & IMPULSED: both use multiple diffusion times, but VERDICT uses conventional PGSE with higher *b*-values, resulting in a narrower range of diffusion times. In addition, VERDICT uses multiple different TE, which results in biases in fitting due to relaxation effects.
Jiang, Dudzinski et al. (2020)	Study tumor response using IMPULSED	Varian DirectDrive horizontal 4.7 T magnet (Varian, Palo Alto, California, USA)	TE = 70 ms, 5 b-values ranging [0-1500] s/mm2 at equal logarithmic intervals • PGSE, Δ = {12, 48} ms, δ = 4 • OGSE, *f*= {50, 100} Hz, Δ/δ = {25/20} ms Resulting diffusion times t_{diff} ranged from [2.5-46.7] ms.	In vivo Colon adenocarcinoma in mice	Cell size diameter is here a volume weighted mean *d* - see equation in paper. Computed: f_{ic}, d_{ec}, d_{ic}	/	Two compartments: • 1. Intracellular diffusion modelled by spheres. • 2. Extracellular diffusion modelled by constant d_{ec}. Signals from each tumor voxel were evaluated to see which fitting worked best; constant ADC vs. ADC varying with t_{diff} (*time dependency*). For low SNR voxels, the constant ADC-model was often preferred. For voxels favouring the other model, the DW signal fit to generate parametric maps with the *fmincon* function in Matlab: based on maximization of log likelihood with Rician noise, voxel wise basis fitting. • For only a few voxels (< 1%) cellular parameters could	***Histology, correlation:*** • IMPULSED derived cell sizes show a correlation (r=0.52, p=0.008) with histology-derived cell sizes • IMPULSED derived cell sizes show negative correlation with T cell fraction (r = -0.64, p < 0.0001)	• Cell size *d* correlates with histology-based cell size • The mean cell size *d* has a very low RSD, high precision for a realistic SNR • IMPULSED derived *d* is able to detect cell size decreases associated with treatment-induced T cell infiltration	• In parametric maps, a significant heterogeneity is visible across tumour regions. Might be interesting, for future studieds. • The gradient strength used here is not achievable on any clinical MR scanner, too high • In other studies, it was tested on clinical MR scanner; the sensitivity to dic is then low. However, measurement of cell size *d* is still possible.
Jiang (2017)	Application of IMPULSED in vivo to estimate microstructural features	VarianDirectDrive horizontal 4.7 Tesla (T) magnet (VarianInc., Palo Alto, CA).	TE = 67 ms • PGSE, Δ/δ = {48/4} ms, b= {0,500, 1000, 1500, 2000} s/mm2 • OGSE, *f* = {50, 100, 150} Hz,with respectively b = {{0, 500, 1000, 1500, 2000}, {0, 330, 660, 1000, 1320}, {0, 150, 300, 450, 600) s/mm2, Δ/δ = {25/20} ms Resulting diffusion times t_{diff} ranged from [1.7-48] ms.	In vivo Colon cancers in mice	• Computed: cell size diameter is here a volume weighted mean *d* - see equation in paper -, f_{ic}, d_{ec}, d_{ic}, the slope of the d_{ec} with respect to the frequency *f* β_{ec}, 3D tumour cell density ρ based on Eq. from paper, 2D tumour cell density	PGSE-only based ADC	Two compartments: • 1. Intracellular diffusion modelled by spheres. • 2. Extracellular diffusion modelled by constant d_{ec}. Using lsqcurvefit in MATLAB.	***Histology, correlation:*** • IMPULSED derived cellularity shows correlation with histology derived cellularity (ρ=0.81, p<0.0001) • This was a stronger correlation than with ADC (ρ=-0.69, p=0.03), suggesting that IMPULSED is more specific indicator of cellularity • IMPULSED-derived cell sizes are slightly larger than the histology-derived cell sizes, which is explained by shrinkage due to	• Reasonable cell size estimates • Cellularity correlates strongly and more than ADC; however underestimation • Intracellular volume fractions are underestimations; leads to underestimation of cellularities as well • Due to challenges in co-registration between histology and MRI; voxel-wise correlation between histology and MR not possible. This should be done in future studies.	• Water exchange is assumed to be negligible in this model. In this method PGSE measurements with long t_{diff} are used; causes this model more likely to be affected by water exchange than with only OGSE. This process plays a role in the cellularity underestimation •Capillary perfusion was ignored in this study; because perfusion fraction of tissues is <<< diffusion fraction of tissues; if tumor angioginesis is large / non-negligible; the PGSE/OGSE sequence should be modified to acquire perfusion-free MR signals by inserting PGSE filter with small b-value at beginning of sequence.
Li (2017)	Investigate influence of trancytolemnal water on estimates of microstructure from PGSE or IMPULSED methods	Varian 4.7 Tesla MRI spectrometer (Palo Alto, California,USA)	Three separate parts: • τin the intracellular exchange lifetime was estimated with a constant gradient experiment, δ = 10 ms, Δ ranging from [20-426] ms in 30 increments. • PGSE: δ = 4 ms, Δ = {10, 25, 35, 50} ms, TR/TE = 3500/60 ms,11 gradient strenghts varying linearly from [0-20] g/cm • IMPULSED: TR/TE = 3500/60 ms, 9 b-values evenly distributed over [0-2000] s/mm2 - PGSE: Δ/δ = 52/4 ms - OGSE: Δ/δ = 30/25 ms, *f* = {40, 80} Hz Resulting in diffusion times t_{diff} ranging from [4-52] ms	• Simulation study • In vitro murine erythroleukemia cancer cells	Model parameters: • Cell size d, f_{ic}, d_{ic}, β_{ec}, d_{extr}	Two PGSE-based methods: • PGSE_I: that fits d_{ic} as fourth parameter • PGSE_II: fixed value d_{ic}	Lsqcurve fit function MATLAB.	***Simulation study:*** • IMPULSED and PGSE_II accurately estimate *d*, while PGSE_I is only accuratewhen τ_{ic} > 350 ms, and *d* between 10-16 µm • For both IMPULSED and PGSE_II, precision decreases drastically with decreasing SNR • All three methods significantly underestimated f_{ic} • Transcytolemnal water echange has large influence on fitted f_{ic}: it decreases rapidly with a smaller τ_{ic} • d_{ic} estimates reasonable for IMPULSED ***In vitro histology:*** • IMPULSED and PGSE_II had accurate fittings of d, independent of permeability • fic is again underestimated for fast transcytolemmal water exchange • While d_{ic} is slightly more susceptibile to water exchange, it still can be reliably estimated with IMPULSED if exchange is not too fast	• Incorporation of OGSE measurements increases sensitivity to intracellular diffusion, including additional information than PGSE; a more comprehensive way to fit d_{ic} and cell size d • d_{ic} can be reliably estimated by IMPULSED when d is appropriate, τ_{ic} > 100, and SNR is sufficient > 50 • Fitted cell size *d* is relatively insensitivite to transcytolemmal water exchange and is reasonably estimated by IMPULSED • f_{ic} is significantly underestimated	• Realistic clinical gradient strengths were used in this study • Difference VERDICT and IMPULSED: VERDICT requires prior knowledge of d_{ic} and d_{ec} to minimize fitting errors; challenging for this mehod to measure cell size and intracellular diffusivitiy at the same time, due to long diffusion times of PGSE • Transcytolemmal water echange should be incorporated in quantitative difusion models; tau_in should be fit as well; would be more accurate and a relevant parameter as well
Wu (2022)	Investigate feasibility IMPULSED mapping for clinic	3.0-T MRI scanner (Skyra, Siemens Healthcare)	TR/TE = 5000/148 ms, Δ/δ = 30/10 ms • PGSE: b = {400, 800, 1200} s/mm2 • OGSE: *f* = {17, 33} Hz with respectively b = {{400, 800, 1200}, {300, 600}} s/mm2 Resulting in diffusion times t_{diff} ranging from [7.5-26.7] ms	In vivo Prostate cancer in humans	Model parameters: • Computed: cell size d, f_{ic}, d_{ec} d_{ic} is fixed at set value cellularity = f_{ic} / d * 100	PGSE-only based ADC	See git; in MATLAB. Uses lsqcurve fit	***Histological tumour grades comparison:*** • Higher GG: f_{ic} and cellularity higher, lower d_{ec}, more diffusion time dependency • fic shows singificant difference between benign and GG 2-5, *d* significant difference between GG 1 and 2-5. Cellularity between benign, GG1, GG2-5. ***Histology, correlation:*** • Correlation between estimated f_{ic} and histological f_{ic} (r=0.83, p<0.001) • Confirmed by simulation results (r=0.97, p<0.001)	• Correlation between estimated f_{ic} and histological measures is found, for both histology and simulation study • No spatially matched comparison between IMPULSED results and histology possible, only biopsy done of small area of tumor, while MR is of whole tumour region.	• Cellularity had very high AUC ROC 0.96, f_{ic} 0.93 • Cell size and d_{ec} lower, > 0.74 still • Limiting factor is available diffusion time range; not feasible for clinic because gradient magnitudes are unachievable. In this study, however tested with limited diffusion time range and it still works.

Table 4. Information extraction of the articles that reported an evaluation of the *Imaging Microstructural Parameters Using Limited Spectrally Edited Diffusion (IMPULSED)* model – final page [2/2].

Author (year)	Study goal	MRI scanner	Salient diffusion protocol	Tissue condition on MRI	Extra model specifics	Models compared to	Fitting characteristics, including compartment models	Comparisons with ground truth data	Discussion: value for assessment of microstructural properties	Discussion: Other advantages Other limitations
Jiang (2022)	Introduce new joint model that incorporates water echange and compare with original IMPULSED		TR/TE = 3500/60 ms, 9 b-values evenly distributed over [0-2000] s/mm2 - PGSE: Δ/δ = 52/4 ms - OGSE: Δ/δ = 30/25 ms, f = {40, 80} Hz Resulting in diffusion times t_{eff} ranging from [3.125-52] ms	• Simulation study • In vitro murine erytrholeukemia cancer cells	Computed model parameters: • Cell size d, f_{ic}, d_{ec} d_{ic} , Cell membrane permeability P_m • τ_{is} pre-exchange lifetime of intracellular water: to evaluate whether echange is fast or slow in comparison with t_{eff}	IMPULSED compared with *joint model:* based on IMPULSED but incorporates transcytolemmal water exchange	• For t_{eff} < 5ms water exchange was ignored; same model as IMPULSED is used • For t_{eff} > 30 ms; the modified Karger model was used that includes both restricted diffusion and exchange between compartments. • Typically τ_{is} > 30 ms, so if diffusion time is shorter than that, the water exchange is negligible • Model now describes two non-Gaussian compartments undergoing exchange, taking into account effect of restricted diffusion and cell size. (modified Kärger model) Matlab code available on git; uses lsqurvefit.	***Simulation study*** • The joint-model derived τ_{is} and P_m are highly linearly correlated with ground truth r=0.99 and 0.98 with p<0.01 • τ_{is} is highly correlated with CG-based τ_{is}, but significantly smaller • Average fitted d values of joint-model are very close to ground truth and improves wrt original IMPULSED. Thed is less affected by the fast water exchange • Underestimation of f_{ic} is significantly reduced with joint model. ***In vitro study:*** • d values are close to ground truth	• Joint model significantly reduces underestimation of f_{ic} in comparison with IMPULSED • Joint model improves quantification of d, when τ_{is} is 50-100. Joint model and IMPULSED both provide accurate estimates of water exchange when τ_{is} > 100 ms. • Estimation of d can well be done with OGSE measurements with short t_{eff}: because low influence then of water exchange • f_{ic} may be determined by PGSE measurements with long t_{eff} and large b-values; with high influence of water exchange	• More effect of water exchange if τ_{is} decreases or t_{eff} increases • τ_{is} and P_m provide complementary information; they are highly linearly correlated with ground truth simulation and in vitro cell study. However, they were still biased compared with absolute ground truth. • Joint model still uses same scan time as IMPULSED, which is possible on clinical scanners with relatively fast acquisitions • Possible differences in relaxation properties between intra- and extracellular spaces are ignored, like in most compartmentalized models

Table 5. Other techniques that were reported in two or less of the included articles. The used technique is specified in the second column, underlined and bold.

Author (year)	Study goal, **Used model**	MRI scanner	Salient diffusion protocol	Tissue condition on MRI	Models compared to	Model characteristics	Fitting methods	Quantitative comparisons with histology or simulated data	Discussion: value for estimation of microstructural properties	Discussion: Other advantages Other limitations
Xu (2021)	Framework for mapping cell size distributions without assuming any parametric distribution. The **MRI-Cytometry** framework is non-Gaussian and compartmentalized into two compartments (intra- and extracellular).	• *In vitro:* Varian/Agilent 4.7T MRI spectrometer (Agilent Technologies, Santa Clara, CA) • *Animals:* 4.7T Varian/Agilent horizontal small animal scanner (Agilent Technologies) • *Humans:* Philips Achieva 3T scanner	MRI-Cytometry is a general framewok; data was used froma previously aquired study by Xu et al. on IMPULSED. TR/TE = 4500/104 ms • PGSE, Δ/δ = 74/12 ms, b = {0, 250, 500, 750, 1000, 1400, 1800} s/mm2 • OGSE, f = {25, 50} Hz, Δ/δ = {51.4/40/9} ms, with b = {{0, 250, 500, 750, 1000}, {0, 100, 200, 300} s/mm2. Resulting diffusion times t_{diff} ranged from [5-54] ms.	• Simulation study • In vitro cells • In vivo breast cancer xenografts in mice • In vivo breast cancer in humans	/	A probability distribution of: • cell size diameter d (volume-weighted in step 1) • d_{ic} (volume-weighted in step 1) • d_{ec} • β_{ec} • f_c called v_{ic} in the paper	Two compartments: • Intracellular: spheres, with cell size diameter d and d_{ic} • Extracellular: spin packets, each has its own time-dependent diffusion coefficient $d_{ec} = d_{ec0}+\beta_{ec}*f$. Not a single d_{ec} is thus used. Transcytolemmal exchange is ignored. Two step fitting approach: • 1. Uses nonnegative least squares analysis • 2. Uses dictionary with all possible *ic* and *ec* signal forms, and their corresponding weigth. This equation is fit to the data. After fitting, the vector is split into 2 matrices; one for ic and one for ec. In step 1: β_{ec}, d_{ec} determined; in step 2: cell size d, d_{ic} determined.	***Simulation study:*** • Mean distribution of all parameters apart from β_{ec} match simulated ground truth well • SNR has strong impact on fitting precisions for all distributions • Two-step approach improves estimates of d and d_{ic} ***In vitro cells:*** • Correlation between estimated d and histological d for cultured cells in vitro. However σ of distribution of d correlates less. ***In vivo animals:*** • Good agreement estimated d (and its σ) with histology. ***In vivo breast cancer in humans:*** • No direct comparison with histopathology possible yet. • Only compared to IMPULSED results: results suggest that MRI-Cytometry might be more robust and less sensitive to partial volume effect. Estimated cell sizes are highly correlated (r = 0.83, $p < 0.02$).	• Distribution of cell size mappings match ground truth well	• Mapping cell size distribution instead of single values per voxel, is useful for distinguishing different cell populations. • Based on IMPULSED acqusition data, which was ensured to be clinically feasible. Should still be tested for different acquisition methods, but with same MRI-Cytometry framework. • Influences of free water fraction and cell membrane permeability need further investigation. • β cannot be reliably estimated with the currently used diffusion times, unless higher frequencies can be used, MRI-cytometry works better (enhanced fitting precision) as a simplified version by removal of β_{ec} from the fitting parameters.
Naranjo (2021)	Investigate **multidimensional diffusion MRI (MDD MRI)** for microstructural characterization of breast cancer, in clinical setting. Framework relies on novel diffusion gradient waveforms.	3T magnet (Discovery MR750; GEHealthcare, Milwaukee, WI)	Uses anisotropic, versatile b-tensors, instead of b-values: gradient waveforms targeting 37 isotropic linear encoding directions, and 43 spherically encoded signals TR/TE = 5000-2700/98 ms, b = {0, 100, 700, 1400, 2000} s/mm2.	In vivo, Breast cancer in humans		Diffusion Tensor Distributions (DTD) are estimated for each voxel, containing information on the size, shape and orientation of a microscopic diffusion pattern, using the MDD data. Statistical descriptors of the DTD are computed, the mean E and variances V of: • The tensor size D_{A0}. The E represents conventional mean diffusivity, the V the variance of cell densities over the voxel scale. • The tensor shape D_{A2}. The E presents microscopic anisotropy; 0 for spherical, 1 for completely alongated • The orientation dimensions of the DTD. Size-shape space is binned to separate signal fractions: • Elongated cells f_{bin1} • Isotropic environments with low diffusivity f_{bin2} • Large isotropic diffusion environments with high diffusivity f_{bin3}	A set of 200 diffusion tensors is randomly generated and the likelihood is assessed via NNLS fitting; this is repeated and the largest-weight solutions are kept; eventually forming the DTD.	***Comparison cancer vs. healthy and carcinoma types:*** • Cancer and normal tissue was significantly different according to all DTD-based metrics, except for the V[D_{iso}] and f_{bin2} (associated with densely packed isotropic cells). • For purely invasive and mixed invasive and in situ carcinomas, only f_{bin1} and f_{bin3} were signficantly different.	• Parametric maps allow qualitative and quantitative evaluation of the composition and orientational order of healthy tissue and tumours. • Validation based on tumour co-registered histological speicmens is required.	• The DTD-derived mean cell size E[Diso] may provide more consistent and reproducible results than conventional DWI, as DTD imaging takes non-Gaussian diffusion into account • Cancers are characterized by low E[D_{iso}] and low E[D_{A2}], i.e. higher f_{bin2} (elongated cells). Normal tissue exhibited more f_{bin3}. • Bins were set manually, which might limit generalization of the work
Xiong (2022)	Assess ability of **Restricted Spectrum Imaging (RSI)** model for rectal tumor grading. It is non-Gaussian and compartmentalized. Here, three compartments are used (see Eq. in paper): restricted, hindered, free	3 T whole-body scanner (uMR 780, Shanghai United Imaging Healthcare, Shanghai, China)	PGSE, TR/TE = 4600/86.2 ms, b = {0, 10, 20, 30, 50, 80, 100, 150, 200, 400, 600, 800, 1500, 2000} s/mm2, Fitting of RSI was based on only 6 of the b-values: {0, 400, 600, 800, 1500, 2000} s/mm2.	In vivo, Rectal cancer in humans	ADC, **K**	• C_1 volume fraction and D_1 diffusion coefficient of restricted diffusion compartment, intracellular regions • C_2 volume fraction and D_2 diffusion coefficient of hindered diffusion compartment, mostly extracellular • C_3 volume fraction and D_3 diffusion coefficient of free diffusion, not tumor specific	The diffusion coefficients are all fixed at set values, which were theoretically and experimentally determined. This was done to prevent overfitting.	***Tumour grade differentiation:*** • More restricted diffusion C_1 is found in high grade tumors; no difference for the other compartments. • C_1 has capability of discrimining grades with significant difference • ADC and K showed no significant difference between grades • RSI-C_1 had the highest diagnostic ability, with an AUROC 0.753	• RSI-C_1 is a significant indicator for tumor grades; has a high diagnostic ability • RSI has a superior performance than ADC and K • A combination with IVIM coud be useful, utilizing the low b-values as well, to give even more diagnostic information • RSI-C_2 and C_3 do not provide specific descriptions on tumor cellularity, not directly related to tumor grading	• RSI is a highly efficient technique, with scan time less than 5 min • High b-values are required for RSI, poorer image quality. More optimized b-value selection would be good. • The restricted compartment map corresponds to high b value map b=2000 s/mm2.
Yamin (2016)	Evaluation of the reliability of **Restricted Spectrum Imaging (RSI)** to predict variance with histological tumour grade	3.0-T SignaHDxt MRI Scanner (GeneralElectric)	PGSE, TR/TE = 9900/69-72 ms, b = {0, 125, 375, 1000} s/mm2	In vivo, Prostate cancer in humans	/	RSI-MRI cellularity index, based on Z-score cellularity maps	Instead of utilizing one Gleason Grade for a whole tumour ROI, in this study the histopathology of the tumour is analyzed and graded at voxel level; in order to privde more accurate representation of intratmour heterogeneity	***Tumour grade differentiation:*** • RSI-MRI cellularity index distinguished benign from increasingly malignant prostate cancer with $p<1x10^{-5}$ • Trend of higher mean RSI-MRI cellularity with increasing grade	• Based on RSI-MRI cellularity index, it is possible to detect variation of Gleason Grade within a single tumour	• By using this voxel-based approach, a very large sample size (> 2700 voxels) is achieved, even though not many patients were included. • RSI-MRI may be promising for planning of focal therepautic procedures, because it allows identification of areas with the most agressive disease
Yamada (2015)	Determine usefulness of **q-space imaging (QSI)** for esophageal cancer analysis	a 7.0 Tesla(T) MR imaging unit (BioSpec 70/16; Bruker BioSpin,Ettlingen , Germany)	PGSE, TR/TE = 3000/29 ms, Δ/δ = 18.5/4.5 ms, b = {0, 97, 387, 874, 1554, 2423, 3495, 4762, 6206, 7163} s/mm2, corresponding to q = {0, 119, 238,358, 478, 597, 717, 837, 955, 1026) /cm	Ex vivo, formalin-fixed specimens of humans with esophageal squamous cell carcinoma	/	Displacement distribution profiles for each voxel: • Mean displacement in μm, at 0.425 times the FWHM • Probability for zero displacement P_0 • Kurtosis K	In-house software	***Histology, correlation:*** • Correlation between mean displacement and nuclear-cytoplasmic ratio (r=0.793, $p < 0.001$) • Correlation between P_0 and nuclear-cytoplasmic ratio (r=0.793, p<0.001) • Correlation K and nuclear-cytoplasmic ratio (r=0.728, p<0.01) • Correlation mean displacement and cellularity (r=-0.667, p<0.01) • Correlation P_0 and cellularity (r=0.695,p<0.01) • Correlation K and cellularity (r=0.783, p<0.001)	• Significant correlations of q-space parameters and histological parameters • q-space MR imaging is very sensitive to changes in tissue microstructures • The mean displacement provides the real range of restricted diffusion on the micrometer scale	• Significant correlation found between (P0, K, mean displacement) and the histological grades • Study is performed ex vivo, formalin fixed • A very long imaging time was used here, of 43 min • High q-values required to use q-space imaging, with a higher gradient strengths than clinical feasible • Perfusion is not taken into account in this method; combining q-space imaging and IVIM might be helpful
Senn (2019)	Determine whether **q-space imaging (QSI)** works better than conventional DW-MRI to estimate cellularity	Clinical 3.0-T MRI unit with maximum gradient strength of 80 mT/m (Achieva Tx; Phil-ips Healthcare)	PGSE, TR/TE, 5900/94 ms, 32 equidistant b-values ranging [0-5000] s/mm2, corresponding to 32 equidistant q-values ranging [10.4-655] /cm	Ex vivo, formalin-fixed excised human breast tumours	ADC, **K, SEM**	Displacement distribution profiles for each voxel: FWHM computed each distribution. Parametric map based on FWHM formed. For FWHM is computed: • Skewness as marker for asymmetry of the distribution • Median as marker for the average of the distribution	In-house software	**Histology, correlation:** • Correlation between QSI FWM and cellularity (r=-0.513, $p < 0.021$) • Correlation FWHM skewness and cellularity (r=-0.468, p<0.038)	• Tumour cellularity computed with QSI had increased effect gradient compared with the other DWI techniques; higher sensitivity to the underlying differences in breast tumours	• QSI has shown to be feasible on clinical MRI units because of hardware advances, the requirements for the gradient magnitude can be met
Morelli (2023)	To characterize tumor microstructure according to proliferative capacity and predict local recurrence through **microrostructural parameters from conventional DW-MRI** at baseline, in skull-base chordoma (SBC) patients treated with proton (PT) and	Clinical 3T Magnetom Verio Siemens Scanner	b-values = 50,400,1000 s/mm2; resolution 1.98 × 1.98 × 5 mm; TE = 66-83 ms; TR = 5600- 6600 ms; α = 90; GRAPPA factor = 2; head coil with 32 channels	In vivo Skull-base chordoma (SBC)	ADC	It maps multiple ADC values to cellular radius Rf, cell volume fraction vf, cell diffusivity Df apparent cellularity rhoapp	Complex dictionary fitting where ADC values are compared to values obtained from Monte Carlo Simulations	**Agressiveness differentiation:** - All microstructural markers distinguished Between more/less proliferative tumours (high/low Ki-67) **Survival** - A signature made of a combination of All microstructural parameters Can predict survival following radiotherapy	- Markers not validated histologically to ground truth histological counterparts, but they show clinical utility	- The approach removes the need to write analytical models of the signal - However, it is difficult to implement as it required ad hoc Monte Carlo simulations

Table 6. Relaxometry-based techniques, which were all reported in two or less of the included articles. The used method is specified in the second column, underlined and bold.

Author (year)	Study goal, **Used model**	MRI scanner	Salient diffusion protocol	Tissue condition on MRI	Extra model specifics	Fitting methods	Quantitative results	Discussion: value for estimation of microstructural properties	Discussion: **Other advantages** **Other limitations**
Chatterjee & Antic (2022)	Validate prostate microstructure measured by **hybrid multidimensional MRI (HM-MRI),** with quantitative histologic evaluation	3-T multiparametric MRI (Ingenia; Philips Healthcare)	• PGSE, TE = {57, 70, 150, 200} ms, TR = 5000 ms, b = {0, 150, 750, 1500} s/mm2 In combination with: • Standard clinical multiparametric sequences, including T2-weighted and DCE-MRI	In vivo, Prostate cancer in humans	For three tissue compartments, stroma, epithelium and lumen: • Volume fraction V • T2 relaxation • ADC	Voxel-by-voxel basis, fitting equation from paper using nonlinear least-squares method, Matlab.	***Histology, differences:*** • Measured prostate tissue composition did not differ significantly between HM-MRI and histology: for stroma $\rho = 0.23$, epithelium $\rho = 0.08$, lumen $\rho = 0.8$. • For benign tissue, HM MRI overestimated lumen volume ($\rho = 0.01$) and underestimated epithelium ($\rho = 0.01$) in comparison with histology ***Histology, correlation:*** • Overall Pearson's correlation coefficient was greater than 0.9. • Lin's Concordance Correlation Coefficient (CCC) demonstrated that there was excellent agreement between histology and HM MRI: stroma CCC = 0.81, epithelium CCC = 0.90, lumen CCC = 0.87.	• Prostate tissue composition did not significantly differ when evaluated with HM MRI or histology. • Correlation and agreement of HM MRI with histology was excellent, with high correlations. • Tested with both Lin's CCC and Pearson, because CCC also measures the degree of corresondence between two measures based on covariation and correspondence. • Bland-Altman analysis showed good accuracy and high precision • In ex vivo formalin fixed histology, the size of the prostate is reduced by 15%; this could affect volume fractions, especially lumen - since lumen fluids leaks out.	• Cancers were characterized by an increased epithelium and decreased lumen. Cancer was predicted in any voxel with a fractional volume of lumen of < 20%, and fractional volume of epithelium > 40%. • AUC ROC for distinguishing between prostate cancer and benign prostate tissue was high for HM MRI: epithelium 0.96, lumen 0.94. • Previous work has shown that volume fractions of stroma, epithelium, and lumen are better indicators of prostate cancer than cellularity is.
Chatterjee (2022)	Validate prostate microstructure measured by **hybrid multidimensional-MRI (HM-MRI)** by comparing with results from pathologists' intepretation of histopathology slides	3 T Philips Ingenia or Achieva MR scanner	• PGSE, TE = {57, 70, 150, 200} ms, TR = 5000 ms, b = {0, 150, 750, 1500} s/mm2 In combination with: • Standard clinical multiparametric sequences, including T2-weighted and DCE-MRI	In vivo, Prostate cancer in humans	For three tissue compartments, stroma, epithelium and lumen: • Volume fraction V • T2 relaxation • ADC	Voxel-by-voxel basis, fitting equation from paper using nonlinear least-squares method, Matlab.	***Pathologist's interpretation vs. HM-MRI:*** • Measured tissue compositions were similar for epithelium and lumen volume. HM-MRI measures are within range of individual measures from each pathologist. • The between methods agreement is on par with the pathologists' agreement	• Tissue composition measured with HM-MRI matches very closely with results from consensus of three expert pathologists	• AUC ROC for differentiation cancer vs. benign based on epithelium from HM-MRI was 0.87, pathologists 0.969. • For lumen volume, AUC ROC was 0.847 for HM-MRI, 0.768 for pathologists. • Pathologists' assessment was done on formalin fixed prostate tissue ex vivo; formalin fixation reduces size of prostate
Zhang (2020)	Validation of ex vivo **diffusion-relaxation correlation spectrum imaging (DR-CSI)** for measurement of microstructural tissue compartments using histopathology. Instead of assuming a predefined number of compartments, a spectrum is quantified. Based on T2 relaxation and diffusion.	3-T whole-body scanner (Prisma; Siemens, Erlangen, Germany)	• DR-CSI: PGSE, TR = 5000 m, sTE = {60, 80, 100, 120} ms and for each TE, b = {0, 400, 800, 1500} s/mm2 In combination with: • "A high-resolution T2-weighted MRI sequence"	Ex vivo, Fresh (within 15-35 minutes) prostate cancer specimens of humans	Three distinct DR-CSI signal components were consistently identified; thus the entire T2-D spectral space was divided into three regions: f_A, f_B, f_C • Comparison with histological parameters: $f_{epithelium}$, f_{stroma}, f_{lumen}	Signal modeled as a summation of continuous exponential decay functions, based on both T2 and D. Based on the found spectrum, signal component fraction maps are generated by integrating the spectral peaks on the voxelwise T2-D spectra. If there are three peaks, three signal component fractions are derived.	***Histology, correlation:*** • All three DR-CSI fractions were positively correlated with the histological volume fractions based on a linear mixed-effects model (all $p < 0.001$) • f_A vs. $f_{epithelium}$ $\rho = 0.74$, • f_B vs. f_{stroma} $\rho = 0.80$ • f_C vs. f_{lumen} $\rho = 0.67$ • ADC was correlated with $f_{epithelium}$ ($\rho = -0.68$, $p = <0.001$) and f_{lumen} ($\rho = 0.42$, $p = 0.002$), but not with f_{stroma}.	• A significant positive correlation was found between all DR-CSI signal component fractions and the histopathology area fractions • The found correlations were stronger for DR-CSI than for ADC • Validation in vivo is required, this was only ex vivo	• For this technique, no prior information like the number of components or a fixed cell size radius of the intracellular component (such as with VERDICT) is required. • Unlike HM-MRI, no predetermined tissue diffusion coefficients were required for this model.
Dai (2023)	Assess the performance of in vivo **diffusion relaxation correlation spectroscopic imaging (DR-CSI)** in grading clear cell renal cell carcinoma (ccRNC)	3T Siemens Prisma	• In vivo DR-CSI: PGSE EPI (TE: 51/80/110/140/180/200 ms; b-value: 0/150/400/800/1200/1500 s/mm2)) • Other anatomical sequences • ADC and T2 mapping • DCE MRI	In vivo kidney imaging	• 5 different DR-CSI ADC-T2 spectra were identified. Maps of signal fraction of each spectrum were produced voxel-by-voxel (Va, Vb, Vc, Vd, Ve). • Spectra signal fractions were compared across ccRNC grades, as obtained by visual histopathological analysis of HE images obtained from total or partial nephrectomy	Regularised spectral fitting based on the MERA toolbox, using a 30 x 30 grid of ADC-T2 values and cross-subject spectral standardisation to mitigate inter-subject differences in the position of spectral peaks	**Histology, classification:** • Vb differenciates low grade (G1-G2) from high grade (G3-G4) with AUC 0.801 • Vb differenciates G1 from G2-G4 with AUC 0.796 • Best grade disctrimination: model with Vb, Vd, tumour size and age (AUC = 0.927) **Histology, correlations:** • Vb correlates with tumour grade ($r = 0.553$, $p < 0.001$) • Vd correlates with tumour grade ($r = -0.378$, $p = 0.001$)	• Spectral signal fraction maps provide insight on the agressiveness of the tumour, being correlated with grade • Spectral signal fraction enable non-invasive grading of the tumour, especially if coupled to additional clinical variables like tumour size	• 5 regions of interest were arbitrarily identified, corresponding to tumor, necrosis, cysts, normal cortex and normal medulla • These were used to calculate 5 characteristics spectra • Different results would have been obtained if the number and characteristics of the components had been defined differently

Table 7. Techniques to link histology maps to mp-MRI using AI, which were all reported in two or less of the included articles. The used method is specified in the second column, underlined and bold.

Author (year)	Study goal, Used model	MRI scanner	Salient diffusion protocol	Tissue condition on MRI	Extra model specifics	Fitting methods	Quantitative results	Discussion: value for estimation of microstructural properties	Discussion: Other advantages Other limitations
Sun (2018)	Quantitatively estimate prostate cell density from **multiparametricMRI** data, using **machine learning** models. Histological data and mpMRI data are registered at a voxel level.	3TSiemens Trio Tim machine (Siemens Medical Solutions,Erlangen, Germany)	• DWI: b = {50, 400, 800, 1200} s/mm2, Δ = 36.4 ms, In combination with: • T2-weighted MRI • DCE-MRI	• In vivo, Prostate cancer in humans • Ex vivo, Prostate cancer specimens of humans used for the co-registration of histology	Cell density in 10^3 cells/mm, including both cancerous and normal cells	For model training, voxels were treated as independent samples, with feature vectors existing from mpMRI data and the outcome being the cell density from histologic data. Three regression models are used: multivariate adaptive regression spline (MARS), polynomialregression (PR) and generalised additive model (GAM).	***Model accuracy:*** Performance of the three regression models was measured by root mean squared error (RMSE) in 10^3 cells/mm2: • MARS 1.07 +- 0.05 • PR 1.07 +- 0.06 • GAM 1.06 +- 0.06 Small difference, but significant. GAM had best performance.	• Prostate cell density can quantitatively be estimated from high-quality co-registered histological data, using regression models. • The best performing model was the GAM.	